Tunisian Republic
Ministry of Higher Education and
Scientific Research

University of Sfax
National School of Engineers of Sfax

Doctoral School of
Sciences and Technologies

DOCTORAL Thesis

Order Number: 60/17

Doctoral Thesis

Presented at

National School of Engineers of Sfax

In partial fulfillment of the requirements to obtain

DOCTORAT

in Mechanical Engineering

Presented by

Safa BEN ARAB CHAKER

Composite Shaft Rotordynamic Analysis Using the Finite Element Method

December 9th - 2017

Dissertation committee:

M. Lotfi HAMMAMI	**ENIS - University of Sfax - Tunisia**	**President**
M. Rachid NASRI	**ENIT - University of Tunis El Manar - Tunisia**	**Reviewer**
M. Abdelkhalak ELHAMI	**INSA Rouen - University of Normandy - France**	**Reviewer**
M. Ramiro MARTINS	**FEUP - University of Porto - Portugal**	**Member**
M. Slim BOUAZIZ	**FSS - University of Sfax - Tunisia**	**Director**
M. José DIAS RODRIGUES	**FEUP - University of Porto - Portugal**	**Director**
M. Jorge SEABRA	**FEUP - University of Porto - Portugal**	**Co-supervisor**
M. Mohamed HADDAR	**ENIS - University of Sfax - Tunisia**	**Co-supervisor**

Tunisian Republic
Ministry of Higher Education and Scientific Research
University of Sfax
National School of Engineers of Sfax
Doctoral School of Sciences and Technologies
Doctoral Thesis – Order Number: 60/17

University of Porto
Engineering Faculty
Doctoral Program in Mechanical Engineering
December 2017

Composite Shaft Rotordynamic Analysis Using the Finite Element Method

Safa BEN ARAB CHAKER

Doctoral Thesis
developed under the Co-Supervision Thesis Agreementof November 1st, 2014,
between the University of Sfax, Tunisia, and the University of Porto, Portugal.

Submitted to the National Engineering School of Sfax,
in partial fulfilment of the requirements to obtain the

Doctorat

in Mechanical Engineering

Members of the Jury:

M. Lotfi HAMMAMI	ENIS - University of Sfax - Tunisia	President
M. Rachid NASRI	ENIT - University of Tunis El Manar - Tunisia	Reviewer
M. Abdelkhalak ELHAMI	INSA Rouen - University of Normandy - France	Reviewer
M. Ramiro MARTINS	FEUP - University of Porto - Portugal	Member
M. Slim BOUAZIZ	FSS - University of Sfax - Tunisia	Director
M. José DIAS RODRIGUES	FEUP - University of Porto - Portugal	Director
M. Jorge SEABRA	FEUP - University of Porto - Portugal	Co-supervisor
M. Mohamed HADDAR	ENIS - University of Sfax - Tunisia	Co-supervisor

From the depths of my heart and with the greatest pleasure of this world, I dedicate this work to my dear father ***Thameur*** *and my dear mother* ***Hedia*** *for the great love they gave me.*
I deeply indebted to my parents for their support, sacrifices and uninterrupted encouragement. For all they have endured to satisfy all my needs and wishes, for this specific day.

God save my parents and grant their long happy life. It is in this testimony that I wish to show them my sincerest gratitude and appreciation.

To my sister ***Omaima*** *and my brother* ***Salem****, for their constant encouragement. They have been always here for me all the time, surrounded me with love and support.*

To my dear husband ***Ahmed****, for his continued and unfailing love, support and understanding. I greatly value his contribution and deeply appreciate his belief in me.*

To all the members of my broad family, you receive my gratitude and my profound respect.

To all my friends, their names are beyond the capacity to be cited in a page, for their fraternities and their support. To all those I love and who love me, who helped me from far or near at this period and make it more comfortable.

They will be filled with happiness and joy.

To all of you, I hope you are proud of me !

I lovingly dedicate this work to all of you my dears !

Acknowledgements

First of all, I thank Allah for giving me the strength and the ability to work for my goals.

I would like to express my deep and sincere gratitude to my directors M. Slim Bouaziz and M. José Dias Rodrigues for providing whatever advice and resources necessary for me to achieve my goals. Their understanding, encouraging and personal guidance have provided a good basis for my work.

Special thanks are also offered to M. Mohamed Haddar and M. Jorge Seabra for providing me this exceptional opportunity and for their endless help and support.

I want to express appreciation to the president of jury M. Lotfi Hammami, to the reviewers M. Rachid Nasri and M. Abdelkhalak Elhami and to the member in committee M. Ramiro Martins who kindly agreed to judge my work.

I would like to thank my colleague João Amorim for whatever help and company he has provided and to express my love to my friend Maroua Hammami for her wonderful company and moral support.

To all the members of ENIS: *National Engineering School of Sfax, FEUP*: *Faculty of Engineering of University of Porto and INEGI*: *Institute of Science and Innovation in Mechanical and Industrial Engineering, you receive my gratitude and my profound respect.*

Author gratefully acknowledges the funding of Project NORTE-01-0145-*FEDER*-000022 - *SciTech - Science and Technology for Competitive and Sustainable Industries, cofinanced by Programa Operacional Regional do Norte* (*NORTE*2020)*, through Fundo Europeu de Desenvolvimento Regional* (*FEDER*).

Contents

List of Figures

List of Tables

Abbreviations

Symbol	Meaning
CLT	Classical laminate theory
dof	Degree of freedom
EMBT	Equivalent modulus beam theory
FEM	Finite element model
FGM	Functionally graded material
FRF	Frequency response function
LBT	Layerwise beam theory
LST	Layerwise shaft theory
LT	Laminate theory
SHBT	Simplified homogenized beam theory

Nomenclature

Symbol	Meaning
$(1, 2, 3)$	Orthotropic axes of composite layer
A	Shaft cross sectional area
α	Fiber orientation angle
C_{yy}, C_{zz}	Bearing damping in y and z directions respectively
C_{yz}, C_{zy}	Coupled terms of bearing damping in y-z plane
d	Derivative
∂	Differential
E_1, E_2	Elastic modulus of composite material in "1" and "2" directions respectively
E_i	Young's modulus of the inner material of functionally graded material
E_o	Young's modulus of the outer material of functionally graded material
$\{\varepsilon\}$	Strain field
G_{12}, G_{13}, G_{23}	Shear modulus of composite material in orthotopic axes
$[G(\Omega)]$	Gyroscopic matrix of the shaft
$[G_D(\Omega)]$	Gyroscopic matrix of the disk
Γ_{R/R_0}	Instantaneous angular velocity vector
h_k	Thickness of the kth layer of composite shaft
h_D	Thickness of the disk
I_m	Mass per unit length of the composite shaft
I_d	Diametrical moment of inertia of the composite shaft cross section
I_{Dd}	Diametrical moment of inertia of the disk cross section
I_p	Polar moment of inertia of the composite shaft cross section
I_{Dp}	Polar moment of inertia of the disk cross section
J	Jacobian of the transformation
$[J]$	Tensor of inertia
k_s	Transverse shear correction factor
K_{yy}, K_{zz}	Bearing stiffness in y and z directions respectively
K_{yz}, K_{zy}	Coupled terms of bearing stiffness in y-z plane
$[K]$	Stiffness matrix of the composite shaft
$[K_d]$	Dissipation matrix of the composite shaft
$[K_c]$	Circulation matrix of the composite shaft
L	Length of composite shaft
L^e	Length of an element

m_D	Mass of the disk
m_u	Mass unbalance
$[M]$	Mass matrix of the composite
shaft$[M_D]$	Mass matrix of the disk
M_y, M_z, $M_{x\phi}$	Stress couples
n	Power law index of functionally graded material
N_x, $Q_{xr}^{(i)}$, $Q_{x\phi}^{(i)}$	Stress resultants
$[N]$	Shape function matrix
ν_{12}, ν_{13}, ν_{23}	Poisson's ration of composite material in orthotopic axes
ν_i	Poisson's ration of the inner material of functionally graded material
ν_o	Poisson's ration of the outer material of functionally graded material
Ω	Rotational speed
P	Number of layers
$P(r)$	Generic material property of functionally graded material
P_o	Property of the outer material of functionally graded material shaft
P_i	Property of the inner material of functionally graded material shaft
Π	Deformation energy of the composite shaft
$\{q\}$	Vector of generalized coordinates
$\{Q\}$	Vector of generalized forces
$[Q]$	Material stiffness matrix
$\left[\bar{Q}\right]$	Transformed material stiffness matrix
$R_0\,(C, x, y, z)$	Coordinate system fixed to the space
$R\,(C, x_3, y_3, z_3)$	Coordinate system fixed to the cross section of the shaft and the disk
R_{Di}	Interior radius of the disk
R_{De}	Exterior radius of the disk
R_p	Inner radius of the pth layer of composite shaft
R_{p+1}	Outer radius of the pth layer of composite shaft
R_i	Inner radius of the shaft
R_o	Outer radius of the shaft
R_m	Mean radius of the shaft
ρ	Mass density of the composite shaft
ρ_i	Mass density of the inner material of functionally graded material
ρ_o	Mass density of the outer material of functionally graded material
ρ_D	Mass density of the disk
$\{\sigma\}$	Stress field
t	Time
T	Kinetic energy of the composite shaft
T_D	Kinetic energy of the disk
T_u	Kinetic energy of the mass unbalance
$[T]$	Transformation matrix

θ_x	Angular displacement about x axis
θ_y, θ_z	Rotations about y, z axes respectively
u_x, u_y, u_z	Displacements along x, y, z directions respectively
v, v, w	Flexural displacement along x, y, z directions respectively
W	Work of the bearings
ω	Natural Frequencies
ξ	Natural coordinate
(x, y, z)	Cartesian coordinate system
(x, y, ϕ)	Cylindrical coordinate system

Chapter 1

Introduction and Literature Review

1.1 Rotor dynamic

Rotor dynamic is an extremely important branch of the discipline of dynamics that deals with behaviour of huge assortment of mechanical systems in which at least one part rotates with significant angular momentum, defined as rotor. Rotors are referred as fixed rotors in case they are provided with bearings to constrain their spin axis in a more or less rigid way to a fixed position in the space, whereas they are defined as free rotors in case they are not constrained in any way. In the case of fixed rotors, the rotational speed is often considered as constant or at least as imposed by a driving equipment, while in the case of free rotors, the spin speed is governed by the conservation of the angular momentum [Genta, 2005]. Rotors represent a very important part in many machines, devices and plants and represent the largest and most important class of machinery used in aerospace, automotive, nuclear and oil industries. We can cite some applications of rotating machines such as: drive shaft (figure 1.1), pump (figure 1.2), turbine (figure 1.3) and compressor (figure 1.4).

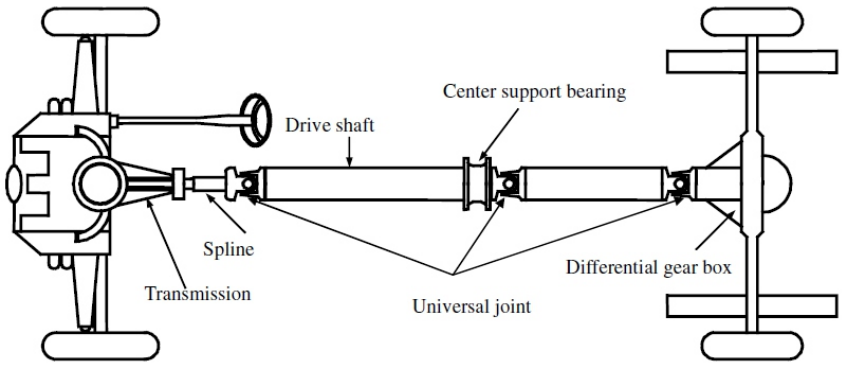

Figure 1.1. Drive shaft [Lee et al., 2004]

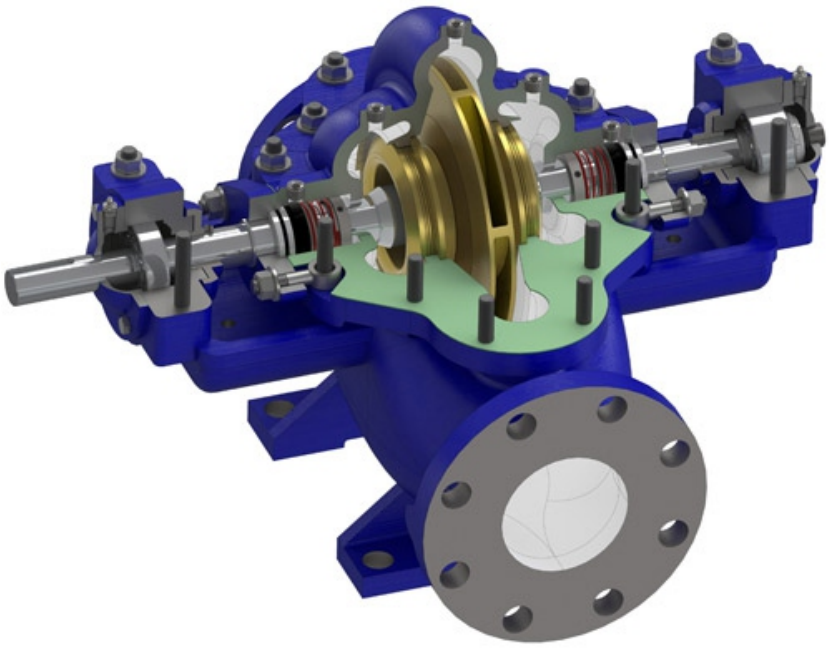

Figure 1.2. Double suction pump [Web1, 2017]

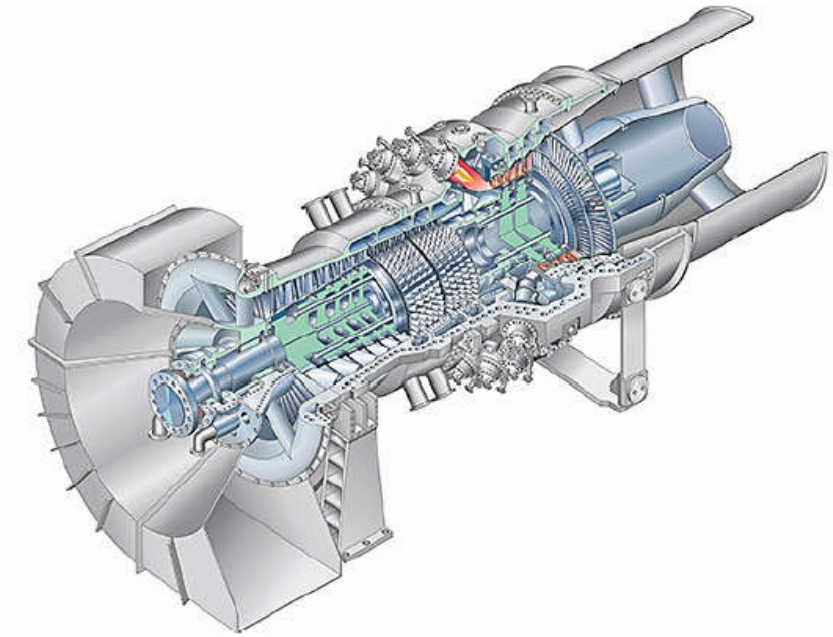

Figure 1.3. Gas turbine [Web2, 2017]

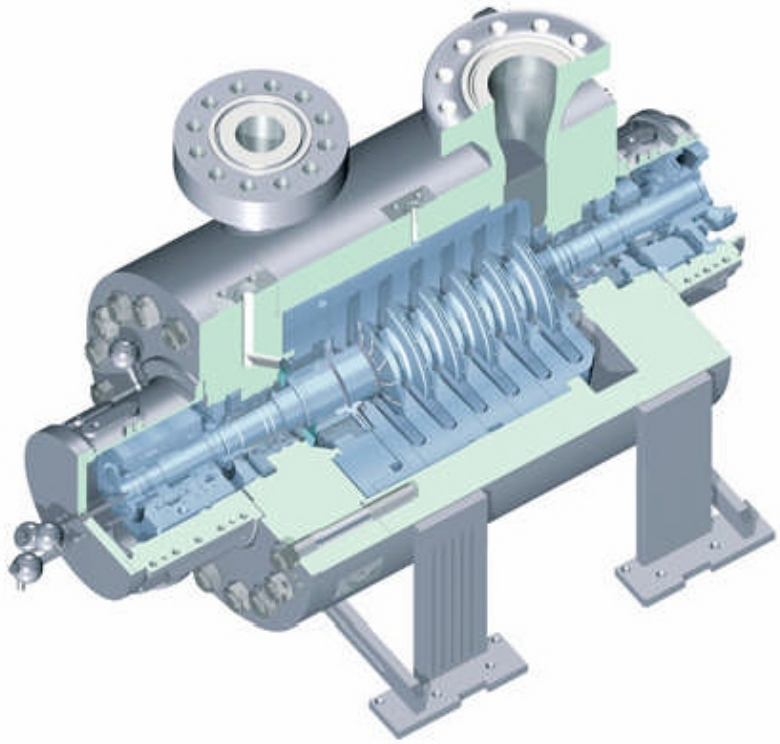

Figure 1.4. Turbo compressor (STC single shaft compressor) [Web3, 2017]

Research in rotor dynamic related to technological applications started back to the second half of the nineteenth century. In fact, the increase of the operating range and the spinning speed of many rotating machine elements made it mandatory to include the rotation into the analysis of their dynamic and stability behaviours. However, with the availability of larger computing power and the versatile measurement technologies, the dynamic of rotating systems has been well treated and the problem of the behaviour of the rotation has been successfully dealt by several mathematicians and theoretical mechanicians. Because of industry demand, a progress is achieved in the design and manufacturing process allowing today to decrease the rotor system weight and to increase at the same time the performance and the efficiency of rotating machines by making them operate in rotational speed ranges increasingly higher. However, the increasingly significant generated efforts influence highly the dynamic and stability behaviour of the rotating machine and the vibratory amplitudes become usually too high for the structure to support them. For that purpose, the deformation amplitude of the rotating machines must be identified and controlled and its resonant frequencies must be determined to avoid that too much vibration causes a lower yield and a higher noise. This vibration can even lead to instability, catastrophic failures and damage of the rotating system such as: fatigue failure, power loss and damage of the bearings. Therefore, the history and the development of the subject of rotor dynamics is an interesting one and the study of the dynamic of rotating machines is so more relevant than ever.

1.2 Composite shafts

The development of technology and the evolution of modern civilization widened through the development of new materials elaborated from new methods of design and manufacturing. In fact, the new materials should be light, should have high performance efficiency and reliability and should be possible to use them at extreme environments such as: high/low temperature, high/low pressure and high corrosion. The high demands on materials for better overall performance in many fields, such as aerospace and transportation has led to extensive research and development efforts in the composite material fields to achieve the technological requirements. Composite materials can be defined as a combination at a macroscopic level of two or more dissimilar materials having a distinct interface between them such that the properties of the resulting material are superior than those of the individual constituents and that certain improved or desired properties are achieved. Currently composite materials refer to materials having strong fibers, continuous or noncontinuous, which are the principal load-carrying components surrounded by a weaker matrix material which keeps the fibers together, acts as a load-transfer way between them and protects them from being exposed to the environment. Constituent materials are the main difference between composite and alloy. In fact, they are insoluble in each other and retain their individual properties in the case of composites, while in the case of alloys, the constituent materials are soluble in each other and form a new material which has different properties from those of its constituents. Moreover, composite materials have important advantages over traditional materials. Some of the properties that can be improved by using composite materials are stiffness, strength, weight reduction, corrosion resistance, damping capacity, lower vibration level, thermal properties, fatigue life and wear resistance. They also offer better noise isolation and, for some of them, good electrical isolation. Furthermore, composite materials arrival opened new ways by enhancing the performance of industrial machines because of their intrinsic qualities. Even now, the technology of composite materials is evolving with the development of nano-reinforcements, new matrix materials, design softwares and manufacturing methods. The main advantage of composite materials is their high specific stiffness and strength. Hence, the use of composite materials can reduce the component weight. The second advantage of composite materials is their energy efficiency. In fact, energy conservation is the major concern of today's world. The operating efficiency of any machinery can be improved by using lighter materials. Most of the composite materials currently used are based on polymer which can be made environs the ambient temperature. Therefore, very little energy is required for composite materials production. As mentioned previously, the extensive use of polymer composites in aircrafts and automobiles will reduce the total weight and consequently increase the fuel efficiency. Composite materials are energy efficient due to these two reasons and there is no doubt that they will continue to play an important role in the energy conservation of the modern world [Balasubramanian, 2014].

The use of composite materials has yielded in remarkable achievements in diverse fields, such as aviation, marine and automobile engineering, medicine, prosthetics and sports, by increasing the specific stiffness and strength, reducing the energy requirements due to the weight reduction and improving the fatigue and the corrosion resistance . Composite materials application has been extensively studied and reported in the literature. Some of the applications reported by [Singh et al., 1997] are propeller shafts in small ships, aircraft power take shaft, high speed tool spindles, transmission shafts and long bars and some of the other applications reported recently by [Gupta, 2015] are helicopter tail rotor and drive

shaft for transmission applications. The different applications can be categorized in two groups (i) the subcritical operation (rigid rotor) where the main objective is the maximization of the weight saving and the torque transmission and (ii) the supercritical operation (flexible rotor) where additional factors such as shaft flexural vibrations, dynamic stresses, stability and fatigue life acquire significant.

For aerospace applications, the primary criteria is related to the performance. Therefore, the primary focus includes reduction of weight, maximization and optimization of critical speeds and reduction of dynamic response at operating speed. For composite shaft applications, elaborated algorithms have been developed for accurate adjustments of fiber winding angles and stacking sequences. In one of the first studies carried by [Zinberg and Symonds, 1970], a boron/epoxy helicopter tail rotor drive shaft was optimized for weight saving of 28% with the critical speed, torsional buckling and strength as design criteria. In more recent studies, [Roos and Bakis, 2011] have used genetic algorithm for optimization of minimum overall weight of a helicopter drive shaft including the determination of the optimal stacking sequence, number of layers and number of in-span bearings. Different practical conditions like variable torque and speed, shaft misalignment and different load cases were considered in this analysis. Moreover, the drive shaft self-heating was illustrated and evaluated and influence of material properties on frequency and temperature was taken into account. Weight saving of 20% is obtained. Some of the important results from this paper are (i) whirling instability is maximum bearing span dependent, which decides the minimum number of in-span bearings required (ii) minimum number of layers required is governed by maximum stresses and buckling and (iii) shaft overheating strongly affects fiber orientations and typically prevents fiber angle orientations of 20°. It was also proved that 30% of weight saving is possible, for the case of constant power transmission in Blackhawk driveline, by adjusting ratio of rotational speed and driving torque. [Montagnier and Hochard, 2013] have used also genetic algorithm for optimization of a hybrid helicopter tail rotor composite shaft operating at subcritical and supercritical speeds. General rules for fibers lay-up were suggested to facilitate the optimization, such as 0° high modulus fibers for maximum axial stiffness and minimum damping, $\pm 45^\circ$ high strength layers for torque transmission and 90° high modulus layers farthest from the shaft middle surface for buckling torque. Results proved also the feasibility of reduction in number of supports, thereby considerably reducing the driveline overall weight.

On the other hand, for automotive applications, cost is one of the main criteria. Therefore, accurate detailed cost sensitivity analysis is performed in order to get a cost optimal design. Several researches have focused on the design optimization of composite drive shafts for power transmission applications. In fact, the one piece composite drive shaft is designed to replace the conventional steel drive shaft of an automobile. The major advantage of this design is that only one piece of composite drive shaft can strongly fulfil all the drive shaft requirements. Conventional drive shafts are made in two pieces to reduce the natural bending frequencies, while composite shafts can be made as single piece shafts, thereby reducing the overall shafts weight. As an example, for Mercedes-AMG GT, which is the second sports car model series developed entirely in house by Mercedes-AMG, the power is transmitted by means of a shaft made of carbon fiber composite material which rotates in aluminum torque tube (see figure 1.5). In fact, the new composite shaft design, resulted in 25% of weight saving, is developed to meet the stringent performance requirements while considerably reducing the fuel consumption [Gindele et al., 2015]. Also, in Formula one car, the torque that causes the rupture of the carbon fiber shaft is 3.5 times higher than the torque that causes the rupture of the steel shaft.

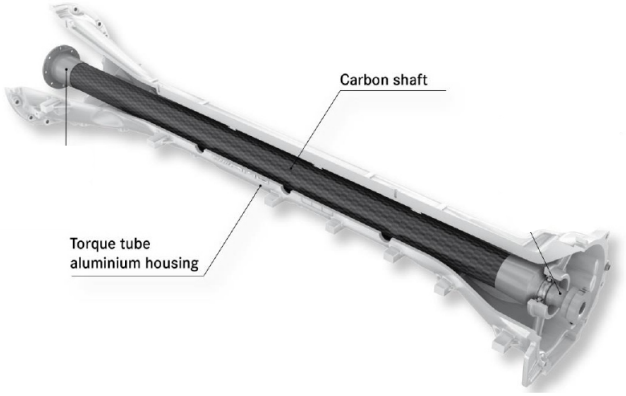

Figure 1.5. Composite shaft in aluminum tube for Mercedes-AMG GT [Gindele et al., 2015]

The use of composite materials in drive shafts provides also designers with the possibility of increasing the shaft length which is an additional advantage for replacing steel shafts by composite shafts. The relationship between the shaft's length and the critical speed for steel drive shaft and composite drive shaft is shown in figure 1.6. Substituting composite structures for conventional metallic structures has much advantages owing to the higher specific stiffness and strength of composite materials.

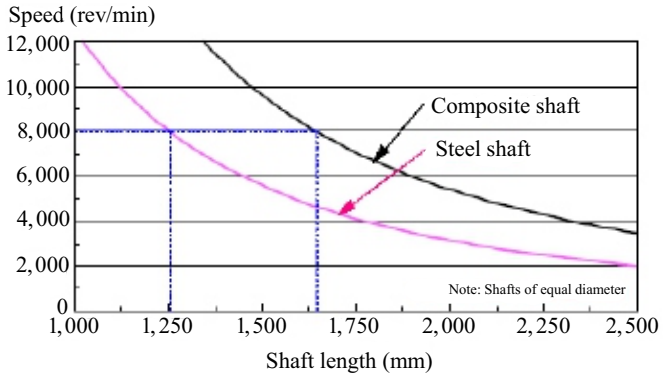

Figure 1.6. Shaft length effect on critical speed [Khoshravan et al., 2011]

[Rangaswamy and Vijayarangan, 2005; Rangaswamy et al., 2002] have focused on design optimization of composite drive shafts made of e-glass/epoxy and high modulus carbon/epoxy while using genetic algorithms in order to minimize the shaft weight which is subjected to constraints like torque transmission, torsional buckling capacities and fundamental lateral natural frequency. Results, given by [Rangaswamy et al., 2002], showed that the stacking sequence strongly affects the buckling torque. Moreover, the weight savings of e-glass/epoxy and high modulus carbon/epoxy shaft are respectively 48.36% and 86.90% [Rangaswamy and Vijayarangan, 2005]. [Chowdhuri and Hossain, 2010] have proposed two different drive shaft designs. One design is made of graphite/epoxy and other one is a hybrid shaft made of aluminum and glass/epoxy. The basic requirements considered are torsional strength, torsional buckling and natural bending frequency. A cheaper and lighter optimum design of the drive shaft was achieved while verifying all the above load requirements. [Badie et al., 2011; Talib et al., 2010] have examined the

influence of fiber orientations and stacking sequences on torsional stiffness, natural frequency, buckling strength, fatigue life and failure modes of composite tubes. They have used a finite element analysis to predict the fatigue life and an experimental program to investigate the torsional stiffness. Authors have shown that composite drive shaft has a frequency reduction of 54.3% when the orientation of carbon fibers at one layer, among other three glass ones, changed from $0°$ to $90°$ and that critical buckling torque has a peak at $90°$ and a lowest value at a range of $20 – 40°$ when the orientation angle of one or two layers in a hybrid or of all layers in non-hybrid transformed similarly. For fiber orientation angle equal to $\pm 45°$, authors have proved experimentally that composite tubes experience higher torsional stiffness and higher load carrying capacity and that specimens of carbon/epoxy and glass/epoxy composites show catastrophic failure mode. Authors have proved also that in a hybrid of both materials, $[\pm 45°]$ configuration affects the failure mode. [Khoshravan and Paykani, 2012; Khoshravan et al., 2011] have presented a design method of a carbon/epoxy composite drive shaft and its coupling and a vibration analysis. Critical speed, static torque, fiber orientation and adhesive joints were studied and Tsai-Hill failure criterion was implemented to control the rupture resistance of the composite shaft. This analysis highlights the importance of the appropriate design of composite drive shafts. Results revealed that fiber orientations have a great influence on the dynamic characteristics of the composite shaft. Furthermore, results showed that the substitution of the composite drive shaft has resulted in considerable weight reduction about 72% compared to the conventional steel shaft. Figure 1.7 shows a mass comparison between steel and composite drive shafts.

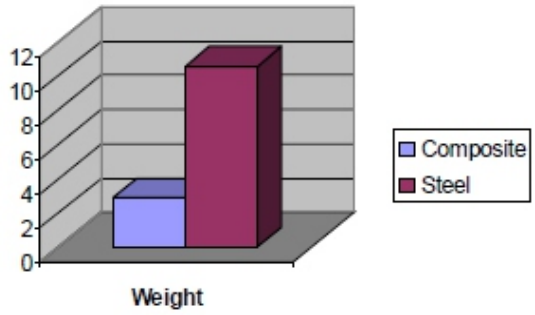

Figure 1.7. Mass comparison between steel and composite drive shafts (kg) [Khoshravan and Paykani, 2012]

[Dongare and Deshmukh, 2013] have analysed the influence of fiber orientations on axial loadings, torque, buckling torque and modal frequencies of composite drive shaft. Authors have established, using a developed regression equation, a relation between stress and fiber orientation and another relation between deflection and fiber orientation and they have shown also that fibre orientation angle has significant effect on the buckling torque. [Moorthy et al., 2013] have designed and compared carbon/epoxy and kevlar/epoxy composite drive shafts in terms of torsional strength, natural bending frequency and torsional buckling with the conventional steel drive shaft. This analysis showed that the use of carbon/epoxy results in 89.76% of mass saving when compared to the conventional steel drive shaft, while kevlar/epoxy results in 72.53%. Moreover, the number of layers necessary in the case of carbon/epoxy is 14 with 1.82 mm wall thickness as compared to 44 layers with 5.72 mm wall thickness for kevlar/epoxy. Furthermore, the torsional buckling capacity and natural bending frequency are adequate enough to achieve the design requirements in the case of carbon/epoxy drive shaft. In order to reduce the drive shaft weight for an

automotive application, [Bhajantri et al., 2014] have replaced the steel drive shaft by a single piece of e-glass/epoxy, high strength carbon/epoxy and high modulus carbon/epoxy composite drive shafts. The weight savings of the high strength carbon/epoxy and high modulus carbon/epoxy drive shafts are equal to 50% approximately of the steel drive shaft. Results proved also that optimum fibre orientation angle plays an important role in composite shaft requirements. [Gubran and Gupta, 2014] have applied a simulated annealing approach for weight optimization of automotive composite propeller shaft. The analysis focused on the effects of design variables such as layer thickness, fiber orientation angles and stacking sequences on shaft natural bending frequency, buckling and transmission torque capacity. Authors have compared six shafts of different materials like steel, aluminum, graphite/epoxy and glass/epoxy and different combinations. Results showed that weight saving of 88% for carbon/epoxy and 73% for glass/epoxy shaft is possible and that a single piece hybrid made of glass/epoxy and aluminum is feasible since its natural frequency is 40% higher than that of metallic shaft.

1.3 Composite shaft deformation theories

Continuous fiber wound composite shaft is considered. In fact, the composite shaft wall thickness consists of several orthotropic layers, each of particular thickness and fiber orientation angle and stacked in a certain order known as stacking sequence. Besides, fibers are placed in helical direction at certain winding angle. In composites literature, Laminate Theory (LT) is performed for the analysis of a laminate to identify stresses, strains and deformations, specifically to determine stiffness and strength [Gay, 2003; Tsai, 1984]. LT principle states that orthotropic mechanical behaviour of the composite laminate is evaluated by first analysing each orthotropic layer separately, next treating it as a thin two-dimensional orthotropic layer and then combining suitably the orthotropic characteristics of all the individual layer. This theory is based on important assumptions like perfect adhesion between the layers, continuity of displacement at the interface of two adjacent layer and linear variation of displacement across the thickness of each layer. In the simpler version of LT known as Classical Laminate Theory (CLT), Kirchoff hypothesis is applicable, while in general, Mindlin theory is applicable accounting for the first order shear deformation effect [Gupta, 2015].

In rotor dynamic analysis, structural designers are interested in identifying system natural frequencies, mode shapes, critical speeds, vibration response and instability thresholds. In fact, rotor critical speeds must be sufficiently away from the operating speeds range and dynamic stresses and shaft fatigue life can be estimated from vibration response. To model the rotating composite shaft, several theories have been proposed in the literature, their salient features are presented in following.

Some papers have summarized research on dynamic analysis of composite shafts. In one of the earliest paper, [Singh et al., 1997] have traced a review on the development of composite shafts in varied applications. Different theoretical and experimental aspects of composite shaft dynamics were reviewed. More recently, [Gupta, 2015] have summarized a research on dynamic of composite shafts with an objective to develop lighter rotor system. Precisely, the different aspects dealt were the theories for dynamic analysis of fiber reinforced composite shaft, the modeling and analysis, the experimental work and the design optimization procedures. Various approaches adopted for modeling the dynamic behaviour of composite shafts are summarized in following.

In earliest studies, [Zinberg and Symonds, 1970] have introduced the Equivalent Modulus Beam

Theory (EMBT), which is extensively used for the dynamic analysis of composite shafts, to model a boron/epoxy composite tail drive shaft for a helicopter. In this formulation, equivalent longitudinal Young's modulus and equivalent shear modulus are identified by using laminate theory for symmetrical stacking and shear deformation is not considered. Critical speeds are determined by extrapolation the unbalance response curve which was obtained in the subcritical region assuming the shaft as a thin walled circular tube simply supported at its ends. [Bauchau, 1981] have performed several important investigations on composite shafts subjected to torsion using a water brake at one end. The analysis focused on determination of stiffness, strength characteristics and stresses under unbalanced condition. Strains were measured using strain gages, bending stresses due to unbalance excitation, determined experimentally, were much larger than those calculated using beam theory and the difference was explained as due to non-linear effects and lateral bending critical speeds were determined using a finite element formulation based on Timoshenko beam theory. But, composite shafts were operated in subcritical region and typical rotor dynamic phenomena were not studied. [Kim and Bert, 1993] have determined the critical speeds of a rotating circular cylindrical composite shaft while considering the bending-twisting coupling effects. The shaft was modeled based on shell theories and results were consistent with those of [Zinberg and Symonds, 1970]'s rotor. Authors have shown that for a long shaft, Donnell's theory is not effective and that for a very thin walled drive shaft, the influence of the transverse shear modulus on critical speeds is negligible. Additional works on composite shafts treating theoretical aspect was reported by [Singh and Gupta, 1996a,b]. For composite shafts dynamic analysis, authors have developed the Equivalent Modulus Beam Theory (EMBT) and the Layerwise Beam Theory (LBT) which was reduced from shell theory with a layerwise displacement field [Singh and Gupta, 1996a]. The bending stretching coupling was incorporated. The conventional shaft dynamic parameters like natural frequencies, critical speeds, damping factors, unbalance response and instability threshold were analysed and results from both formulations were compared [Singh and Gupta, 1996b]. Results showed that LBT is more efficient than EMBT because it takes into account the effect of stacking sequence and thickness shear deformation. In fact, EMBT predicts inaccurate results for non-symmetric stacking sequences, while LBT gives better results and produces a more realistic stress field in the laminate. However, LBT requires the development of a finite element with a high number of degrees of freedom dependent on the number of layers. [Chang et al., 2004b] have analysed the vibration behaviour of a simple spinning composite shafts. Based on the first order shear deformation theory, the shaft deformation energy was determined by adopting the three-dimensional constitutive relations of material, whereas the shaft kinetic energy was obtained using the transformed rotating coordinate systems related to the shaft cross section. The transverse shear deformation, rotary inertia and gyroscopic effect, as well as coupling effects due to the staking sequence were taken into account. Authors have demonstrated that the developed continuum-based beam model is compatible to some beam theories available in the literature. They have thereby concluded that the developed model can be considered as a viable alternative for the vibration analysis of the spinning laminated composite shafts. [Gubran and Gupta, 2005] have developed the Modified Equivalent Modulus Beam Theory (Modified EMBT) to analyse the natural frequencies of composite tubular shafts. This theory was formulated to consider the different mechanical coupling effects and stacking sequence effects which are the major limitations of EMBT. The shear–normal coupling effect present in the unbalanced configurations has been introduced by modifying the equivalent Young's modulus expression. The close agreement in results obtained using Modified EMBT and LBT showed that Modified EMBT could be

used effectively for rotor dynamic analysis of tubular composite shafts. This analysis showed also that the maximum reduction in the shaft natural frequency is at 45° fiber orientation angle for Poisson's effect, however for shear–normal and bending–twisting couplings, the maximum reduction is at 30° fiber orientation angle. Authors have concluded that Poisson's effect will be inherently incorporated in the formulation of shear–normal coupling, however for balanced configuration, shear–normal effect is not present, but Poisson's effect will be present and has to be incorporated. [Ghoneam et al., year] have analysed the rotating composite shafts dynamic using a developed finite element model. This formulation takes into account the effects of axial, bending and shear deformation present in rotating composite shafts. The effects of different laminate parameters such as stacking sequences, fiber orientations, fiber volume fractions and boundary conditions on natural frequencies and instability thresholds of the composite shaft were investigated. Results were compared to those obtained using the finite element method and experimental measurements through the frequency response function method by applying the autogenously excitation. The comparison between numerical and experimental results proved the efficiency of the developed finite element model which provides an accurate tool for the dynamic analysis of rotating composite shafts. [Boukhalfa et al., 2008] have performed a free vibration analysis of rotating composite shafts using the p-version, hierarchical finite element method, with trigonometric shape functions. The transverse shear deformation, rotary inertia and gyroscopic effect, as well as the coupling effects due to the lamination of composite layers have been incorporated. Results obtained have been evaluated against those available in the literature and the agreement has been found to be good. Therefore, the efficiency and accuracy of the developed formulation were verified.

1.4 Layerwise composite shaft theory

Systems spinning about their longitudinal axis are used in the most diverse fields of modern technology. In fact, the lamination sequence and material properties of individual lamina provide an added flexibility to designers to adjust the stiffness and the strength of the laminate to agree with the structural stiffness and strength requirements. The theoretical concepts and analysis methods help structural engineers to select suitable material for the best performance in a particular laminated shaft application. Therefore, a better understanding of the laminated shaft dynamic behaviour is required to improve their vibration behaviour, eliminate the occurrence of any instability and enhance their efficiency.

Finite element formulations available in the literature, performed for the dynamic analysis of rotating composite shafts, are based on homogenized beam theory such as Equivalent Modulus Beam Theory (EMBT), Modified Equivalent Modulus Beam Theory (Modified EMBT) and Simplified Homogenized Beam Theory (SHBT) and reduced from shell theory such as Layerwise Beam Theory (LBT). Layerwise theory proposed by [Reddy, 1993, 1997] provides a generalization of the layerwise displacement field concept. [Reddy, 1993] have admitted that, unlike the equivalent single layer theories, layerwise theories assume separate displacement field expression for each individual layer, thus providing a kinematically accurate representation of the strain field in laminates ply and allowing accurate determination of layer level stresses. In composite shaft rotor applications, [Singh and Gupta, 1996a,b] have developed the LBT by direct reduction from a layerwise shell theory after imposing the condition of zero cross-sectional distortion which is achieved by using a relationship between the circumferential and the radial displacements. In fact, [Singh and Gupta, 1996a] have presented several advantages of LBT over EMBT

for symmetric and non-symmetric stacking sequences. They showed the improvement obtained in the natural frequency values of composite shafts using LBT through comparisons with results available from other theories as well as from experiments. So, they have proved that LBT is more efficient than EMBT because it takes into account the effects of stacking sequence and thickness shear deformation. Therefore, they have concluded that layerwise displacement field gives a more realistic representation of the actual deformation and that layerwise theory is able to give a more realistic picture of the various stress distributions in different layers. Recently, Gubran and Gupta [2005] have developed the Modified EMBT to take account of the stacking sequence and the different mechanical coupling effects and updated the LBT, reduced from shell theory, to consider the stacking sequence effect and the influence of the shear-normal coupling which was introduced by modifying the expression of the equivalent longitudinal Young's modulus. Authors have shown that natural frequencies obtained using Modified EMBT excluding different mechanical coupling effects agree well with those obtained using LBT and those reported in the literature.

Literature study explains the need of layerwise analysis for laminated composite structural components in order to get more accurate results because of more realistic displacement field [Moreira and Rodrigues, 2006; Moreira et al., 2006; Patil and Shinde, 2014]. In fact, layerwise displacement field becomes more meaningful in multilayered shaft applications because, in practical shaft configurations, different layers may consist of materials with different properties of several orders of magnitude. So, different laminate may have different slopes.

1.5 Composite shaft stability

The present day rotors are much lighter, handle a large amount of energy and operate at much higher speeds. Hence, they are more sensitive to vibration and instability problems. These have given rise to variety interest in rotor dynamics and stability through the last years. In fact, a major issue in rotor dynamics is the dynamic stability of the system. Practically, every rotor has a speed limit beyond which the rotor system becomes unstable and may operate under critical conditions. The level of this threshold depends on several conditions which affect the rotor dynamic behaviour [Gupta, 2011]. Several researches have been developed in literature, their salient features are presented in following, reveals that much more work is needed to fully knowledge and understand the dynamics behaviour of high speed rotors. [Chen and Ku, 1990] have used a Ritz finite element technique for stability analysis of a rotating shaft subjected to axial periodic forces varying with time. The rotating shaft is modeled using Euler-Bernoulli and Timoshenko beam theories and the transverse shear effect is introduced in the formulation using Timoshenko beam theory. This analysis showed that, owing to gyroscopic effects, boundaries of dynamic instability are shifted and instability region size increases as the rotational speed increases. Authors have concluded that rotatory inertia, transverse shear deformation and gyroscopic moment have a destabilizing effect on the dynamic behaviour of a rotating shaft.

Due to the specific strength and stiffness of the fiber reinforced composite materials, metal shafts have been replaced by composite shafts in many applications such as drive shafts for helicopters and automotive industries as stated in section 1.2. Composite materials offer benefits in terms of reduction of the weight and augmentation of the strength, stiffness and damping capacity and provide structural designers the possibility of obtaining required behaviours by changing the stacking sequence of the composite layers in

terms of number and fiber orientation of layers Using finite element model based on Timoshenko beam theory, stability analysis has been performed under periodic axial force by [Chen and Peng, 1998a] and under compressive loads by [Chen and Peng, 1998b]. [Chen and Peng, 1998a] have shown that for the same geometric properties, a steel shaft has a lower frequency than that of composite shaft, however, the steel shaft is more stable than composite shaft since at lower rotational speeds, the shaft disk system is subjected to axial periodic forces. Authors have shown also that gyroscopic effect makes the steel shaft more sensitive to the periodic axial load than the composite shaft. Furthermore, [Chen and Peng, 1998b] have shown that critical speed of the thin walled composite shaft depends on stacking sequence, length/radius ratio and boundary conditions and that for the same buckling load requirement, composite shaft with a suitable stacking sequence may have better dynamic performance than steel shaft.

An accurate prediction of damping effects is also necessary in the stability analysis of rotor dynamic behaviour. Damping is considered as an internal damping in the case of material damping and as an external damping in the case of bearings damping. For rotor design and stability analysis, consideration of internal damping associated with rotating parts is basically important, because it can generate instability in supercritical regions. Especially, for composite shafts which are even more susceptible due to the relatively higher internal damping coming from the matrix and the preference for supercritical operation to acquire maximum advantages [Wettergren and Olsson, 1996]. First investigations by [Newkirk, 1924] have shown that because of internal damping, rotors may undergo violent whirling at speeds above the first critical speed. [Chandra et al., 1999] have summarized research on damping in fiber reinforced composite materials and structures while focusing on polymer composites. They have described damping studies implicating macro-mechanical, micro-mechanical and viscoelastic approaches, as well as models for interphase damping, damping and damage in composites and they have presented also damping analysis involving composite damping mechanisms and methodology applicable. Further, they have critically reviewed some important works associated with the improvement of damping models for thick laminates, the amelioration of laminate damping and the optimization of damping in fiber reinforced composite materials and structures. Besides, many researchers have studied the combined influence of internal and external damping. Results showed that rotor stability is enhanced by increasing the damping of the bearings, however, increasing the internal damping may reduce the instability threshold [Pereira and Silveira, 2000, 2002]. [Pereira and Silveira, 2002] have used an optimization techniques to avoid the instability, reduce the unbalanced response and augment the stability limit speed. They have adopted the Equivalent Modulus Beam Theory (EMBT) developed by [Singh and Gupta, 1996a,b]. In fact, EMBT has many limitations and is only valid for symmetric stacking as stated in section 1.3. After that, [Genta, 2004] have explained that hysteretic internal damping of structure rotating elements is stabilizing in subcritical ranges and destabilizing in supercritical ranges and they have proved also that an error is made when admitting that hysteretic internal damping of rotating elements is destabilizing at all rotational speeds. [Montagnier and Hochard, 2007] have demonstrated similarly that damping associated to the non-rotating elements of the structure has an usual stabilizing effect while damping associated to the rotating elements may provoke instability in supercritical ranges. [Alwan et al., 2010; Gupta et al., 2009] have focused on estimation of damping in rotor system containing a composite solid shaft. Considering composite materials damping, detailed dynamic studies on the effects of different materials like glass/epoxy, boron/epoxy and carbon/epoxy and different stacking sequences on the unbalance responses and natural frequencies have been carried out. [Gupta et al., 2009] have observed that for

the same material, the system natural frequency increases by keeping the innermost layer parallel to the shaft axis, i.e, 0° fiber orientation angle and they have likewise shown that for the same stacking sequence, boron/epoxy structure is more stiffer in bending and torsional modes. [Richardet et al., 2011; Sino et al., 2008] have examined the effect of internal damping on dynamic and stability behaviour of composite rotors. [Sino et al., 2008] have developed the Simplified Homogenized Beam Theory (SHBT) based on Timoshenko beam theory, which takes into account the hysteretic internal damping to evaluate natural frequencies and instability thresholds. The model was introduced to avoid the main drawbacks associated with formulations that consider only symmetric and balanced stacking sequences. However, SHBT does not consider any mechanical coupling effects. The laminate parameters effects such as stacking sequences, fiber orientations and transverse shear effect on natural frequencies and instability thresholds of the internally damped rotating composite shaft were analysed. Results were compared to those obtained using Equivalent Modulus Beam Theory (EMBT), Modified EMBT and Layerwise Beam Theory (LBT) available in the literature. This parametric study showed that the shaft instability thresholds can be very sensitive to laminate parameters. [Richardet et al., 2011] have illustrated and have validated the theoretical formulation proposed by [Sino et al., 2008] by developing an experimental setup to analyse the dynamic instability of an internally damped rotating composite shaft. [Alwan et al., 2010] have estimated experimentally the composite shaft rotor system damping by three different methodologies. Hysteresis loop method, which can be considered as an important tool, has been demonstrated to estimate the damping at any speed. Results of the experimental evaluation of natural torsional frequency obtained in this study agree well with analytical and theoretical results. [Yongsheng et al., 2014] have performed the dynamic analysis of rotating thin walled composite shafts with internal damping which has been introduced using the multi scale damping analysis method. The numerical study showed the influence of design parameters on natural frequencies, critical speeds and instability thresholds of the shaft and proved that the instability always occurs after the critical rotational speed.

1.6 Thesis objectives

An accurate prediction of rotor dynamic characteristics is fundamentally important in the design of rotating machines. The most important portion of this field is focused on determining natural frequencies, critical speeds, unbalance responses and instability thresholds. This thesis concerns the study of the vibratory and stability behaviours of rotating composite shafts, and more exactly, their rotational behaviour taken into account the influences of laminate parameters and considering the transverse shear, rotary inertia and gyroscopic effects as well as the effects of internal damping and different mechanical coupling due to the stacking sequence of different layers of composite materials. A quantitative study of the influence of various parameters on the dynamic and stability behaviours of rotating composite shafts is carried out.

The major objectives of this work are:

- Development and implementation of finite element models based on Timoshenko theory;
  - Equivalent Single Layer Theory (ESLT)
  - Modified Equivalent Single Layer Theory (Modified ESLT)

  - Layerwise Shaft Theory (LST)

- Validation of the shaft finite element models by comparing with results available in the literature;
- Study of the effects of laminate parameters such as fiber orientations, stacking sequences, shear-normal coupling and nature of the material and rotor components like disk position and bearings properties on the dynamic behaviour of rotating composite shafts;
- Analysis of mechanical coupling effects such as bending-twisting and bending-stretching on the dynamic behaviour of rotating composite shafts;
- Study of hysteretic internal damping effects of composite shaft and damping bearings effects on the dynamic and stability behaviours of the rotor;
- Analysis of the dynamic behaviour of functionally graded material shafts.
- Study of viscoelastic damping treatments effects on the rotor dynamics.

1.7 Thesis layout

The present work is organized in six chapters:

- From a bibliographical research, the first chapter presents an overall vision of the field of rotors dynamics and presents a general information on the intervention of composite materials in shafts domain. This chapter introduces also a global vision of the state of the art of the dynamic analysis of rotating composite shafts using different deformation theories. Particulary, Layerwise composite shaft theories available in the literature are investigated. The chapter ends with literature review of the stability analysis of rotating composite shafts.
- The second chapter presents the modelling of the rotor system elements: rigid disk, mass unbalance and bearings. In this chapter, the expression of the kinetic energy of the rigid disk embarked on the shaft, the mass unbalance force and the virtual work of the bearings are determined.
- The third chapter presents the beam theory, its fundamental hypotheses, and the laminate theory used for modelling the rotating composite shafts. In this chapter, the displacement and the expressions of the kinetic and deformation energies of the rotating composite shaft are determined through the formulation of Equivalent Single Layer Theory. This chapter details the finite element formulation to obtain the stiffness matrix, mass matrix and gyroscopic matrix of the rotating composite shaft, in order to determine the equation of motion of the system. The chapter presents a validation of the elaborated program, illustrates and interprets several examples to analyse the influence of various parameters on the dynamic behaviour of rotating composite shafts. This chapter ends by a conclusion listing the main advances of the developed Equivalent Single Layer Theory.
- The fourth chapter details the mathematical modeling and the finite element formulation of Modified Equivalent Single Layer Theory for the dynamic analysis of rotating composite shafts. This theory is generalized to consider the different mechanical coupling effects. In fact, several case studies

are considered in this chapter in order to analyse the influence of different mechanical coupling on the dynamic behaviour of rotating composite shafts. This chapter ends by a conclusion describing the major advances of the developed Modified Equivalent Single Layer Theory.

- In the fifth chapter is described the development of a new finite element based on layerwise theory for rotating laminated shafts. This chapter details the development of Layerwise Shaft Theory and presents several applications of this theory for the dynamic analysis of rotating laminated shafts. The chapter ends by a conclusion enumerating and illustrating the principal advances of the developed Layerwise Shaft Theory.
- The sixth chapter presents the stability analysis of rotating composite shaft while considering the effects of hysteretic internal damping and external damping of the bearings. This chapter illustrates and interprets several studied cases to determine the effect of various studied laminate parameters and bearing characteristics on the stability behaviour of internally damped rotating composite shafts. This chapter ends by a conclusion listing the major advances of the stability analysis of rotating composite shafts.
- The present thesis ends by a conclusion describing the main advances of the developed work and exposes the future works.

Chapter 2

Modeling of Rotor System Elements

2.1 Introduction

This chapter concerns the theoretical approach for the characterization of different rotor system elements which include the shaft, the disk, the mass unbalance and the bearings. The geometry of the rotor system considered in this work is shown in figure 2.1. The theoretical approach for the characterization of the shaft is considered in the following chapters. This chapter focuses only on the characterization of the disk, mass unbalance and bearings. The disk, of external radius R_{De} and internal radius R_{Di} positioned at a distance h, is considered to be rigid. The mass unbalance denoted by m_u is located at a distance d from the geometric center of the shaft. The shaft is supported at its ends by two bearings.

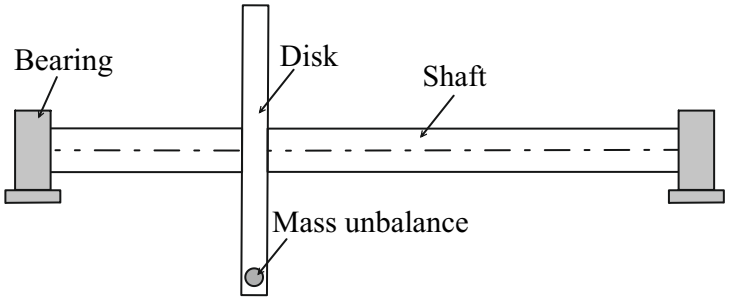

Figure 2.1. Rotor system elements

The equation of motion of the rotor system depends on the equations of motion of each component. Therefore, it is necessary to develop the individual equations of motion of each element. Then, one can assemble them to obtain the general equation of motion of the rotor system. Furthermore, the general equation of motion of the rotor system can be developed using the following approach for the disk, mass unbalance and bearings:

1. Defining the generalized coordinates.
2. Establishing the kinetic energy T and the deformation energy Π.
3. Using the Lagrange's equation to obtain the equation of motion of the rotor system elements:

$$\frac{\mathrm{d}}{\mathrm{d}t}\left(\frac{\partial T}{\partial \dot{q}}\right) - \frac{\partial T}{\partial q} + \frac{\partial \Pi}{\partial q} = Q \tag{2.1}$$

where q is the vector of the generalized coordinates and Q is the vector of generalized forces.

4. Assembling the individual equations of the rotor system elements: discs, mass unbalance and bearings to obtain the general equations of motion.

2.2 Coordinate system

Rotor system is described by two coordinate systems:

- $R_0\,(C, x, y, z)$ which is fixed to the space,
- $R\,(C, x_3, y_3, z_3)$ which is fixed to the cross section of the shaft and the disk and rotates with them.

Both coordinate systems are related through a set of rotation angles. Kinetic energies of the shaft and the disk are a function of the instantaneous angular velocities in $(x_3y_3z_3)$ frame. Therefore, the instantaneous angular velocities expressed in (xyz) frame with $\dot{\theta}_x$ about x axis, $\dot{\theta}_y$ about y axis and $\dot{\theta}_z$ about z axis should be transferred to $(x_3y_3z_3)$ frame.

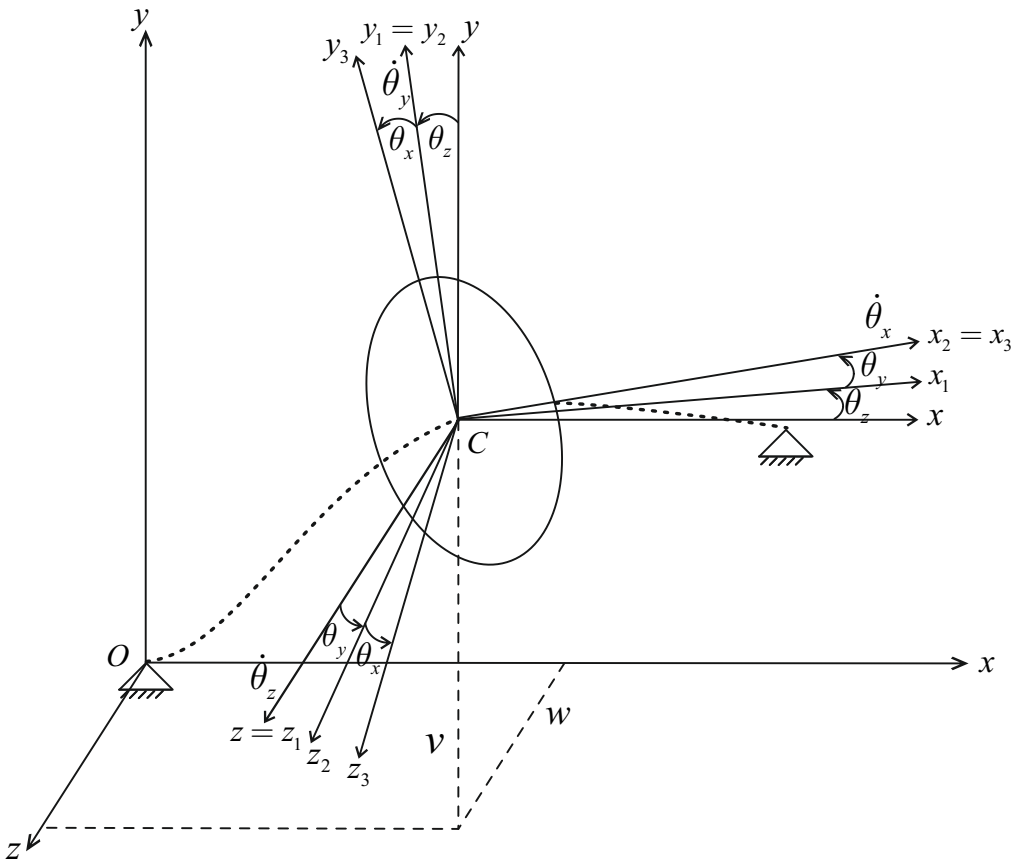

Figure 2.2. Cross section rotation angles

In order to do this, it is necessary to choose an order of rotations and to define two intermediate references, as shown in figure 2.2, to characterize the rotational speed vector Γ_{R/R_0}. The transition of the reference $R_0\,(C, x, y, z)$ to the reference $R\,(C, x_3, y_3, z_3)$ is carried out with aid of three successive rotations which are applied in the following order:

- rotation around (C, z) axis by an amount $\dot{\theta}_z$ which passes $R_0\,(C, x, y, z)$ reference to $R_1\,(C, x_1, y_1, z_1)$ reference where $z_1 = z$,
- rotation around (C, y_1) axis by an amount $\dot{\theta}_y$ which passes $R_1\,(C, x_1, y_1, z_1)$ reference to $R_2\,(C, x_2, y_2, z_2)$ reference where $y_2 = y_1$,
- rotation around (C, x_2) axis by an amount $\dot{\theta}_x$ which passes $R_2\,(C, x_2, y_2, z_2)$ reference to $R\,(C, x_3, y_3, z_3)$ reference where $x_3 = x_2$.

Thus, the instantaneous angular velocity vector is given by:

$$\Gamma_{R/R_0} = \dot{\theta}_z z_1 + \dot{\theta}_y y_2 + \dot{\theta}_x x_3 \tag{2.2}$$

where $\dot{\theta}_x$, $\dot{\theta}_y$ and $\dot{\theta}_z$ are derivatives with respect to time of angular displacements along x, y and z axes respectively.

The relations of passages between different frames of reference, using figures 2.3, are:

$$\begin{cases} z_1 = -\sin\theta_y x_3 + \cos\theta_y z_2 \\ z_2 = -\sin\theta_x y_3 + \cos\theta_x z_3 \\ y_2 = \cos\theta_x y_3 + \sin\theta_x z_3 \end{cases} \tag{2.3}$$

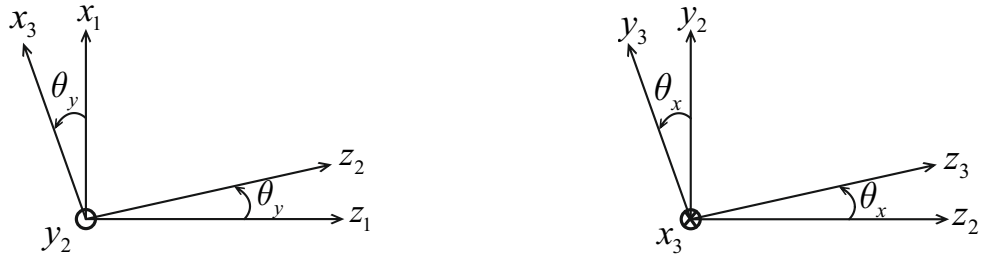

(a) Rotation around y_2 (b) Rotation around x_3

Figure 2.3. Euler's angles

Therefore, the angular velocity vector becomes:

$$\Gamma_{R/R_0} = \begin{Bmatrix} \dot{\theta}_x - \dot{\theta}_z \sin\theta_y \\ -\dot{\theta}_z \cos\theta_y \sin\theta_x + \dot{\theta}_y \cos\theta_x \\ \dot{\theta}_z \cos\theta_y \cos\theta_x + \dot{\theta}_y \sin\theta_x \end{Bmatrix} \tag{2.4}$$

2.3 Rigid disk

An energy method is used to establish the equation of motion of the disk. The disk is assumed to be rigid made of isotropic material. Therefore, the deformation energy is neglected and the disk is described only by the kinetic energy. Coordinate systems of the disk mounted on a rotating shaft, as shown in figure 2.2, are: $R_0\,(xyz)$ which is an inertial coordinate system and $R\,(x_3 y_3 z_3)$ which is fixed to the disk and rotates with it. The disk kinetic energy including the effects of translatory and rotary inertia is given by:

$$T_D = \frac{1}{2} m_D \left(\dot{v}^2 + \dot{w}^2\right) + \frac{1}{2} \Gamma_{R/R_0} . \Big(\left[J_{/C}\right] \Gamma_{R/R_0} \Big) \tag{2.5}$$

where m_D is the mass of the disk, v and w denote the coordinates in R_0 of C which is the geometric center of the disk, the coordinate along x being constant and the tensor of inertia in C, as (xyz) are principal directions of inertia and considering the symmetry, is:

$$\left[J_{/C}\right] = \begin{bmatrix} I_{Dx} & 0 & 0 \\ 0 & I_{Dy} & 0 \\ 0 & 0 & I_{Dy} \end{bmatrix} \tag{2.6}$$

The rotational part of the kinetic energy is calculated with respect to $R\left(x_3y_3z_3\right)$ coordinate system. In fact, the coordinate system $R\left(x_3y_3z_3\right)$, which is fixed to the disk, is related to the inertial coordinate system $R_0\left(xyz\right)$ through a set of three angles θ_x, θ_y and θ_z. It is assumed that the disk rotates around z_1 axis by an amount $\dot{\theta}_z$, then by an amount $\dot{\theta}_y$ around the new axis y_2 and finally it rotates by an amount $\dot{\theta}_x$ around the new axis x_3 as shown in figure 2.2. The angular velocity vector, given in equation (2.4), is:

$$\Gamma_{R/R_0} = \begin{Bmatrix} \dot{\theta}_x - \dot{\theta}_z \sin\theta_y \\ -\dot{\theta}_z \cos\theta_y \sin\theta_x + \dot{\theta}_y \cos\theta_x \\ \dot{\theta}_z \cos\theta_y \cos\theta_x + \dot{\theta}_y \sin\theta_x \end{Bmatrix} \tag{2.7}$$

Thus, using the disk kinetic energy expression (2.5), the tensor of inertia expression (2.6) and the angular velocity vector expression (2.7), the kinetic energy of the disk can be written as:

$$\begin{aligned} T_D = {} & \frac{1}{2} m_D \left(\dot{v}^2 + \dot{w}^2\right) + \frac{1}{2} I_{Dx} \left(\dot{\theta}_x^2 - 2\dot{\theta}_x\dot{\theta}_z \sin\theta_y + \dot{\theta}_z^2 \sin^2\theta_y\right) \\ & + \frac{1}{2} I_{Dy} \left(\dot{\theta}_z^2 \cos^2\theta_y \sin^2\theta_x + \dot{\theta}_y^2 \cos^2\theta_x + \dot{\theta}_z^2 \cos^2\theta_y \cos^2\theta_x + \dot{\theta}_y^2 \sin^2\theta_x\right) \end{aligned} \tag{2.8}$$

In equation (2.8), the angles θ_y and θ_z are assumed small and the angular velocity is assumed constant $\dot{\theta}_x = \Omega$. Therefore, the kinetic energy of the disk including the effects of translatory and rotary inertia as well as gyroscopic ones can be simplified as follows:

$$T_D = \frac{1}{2} m_D \left(\dot{v}^2 + \dot{w}^2\right) + \frac{1}{2} I_{Dd} \left(\dot{\theta}_y^2 + \dot{\theta}_z^2\right) - I_{Dp}\Omega\theta_y\dot{\theta}_z + \frac{1}{2} I_{Dp}\Omega^2 \tag{2.9}$$

where I_{Dd} and I_{Dp} are the diametral moment and the polar moment of inertia of the disk respectively, defined as follows:

$$\begin{cases} I_{Dd} = \dfrac{\pi}{4} \rho_D \left(R_{De}^4 - R_{Di}^4\right) \\ I_{Dp} = \dfrac{\pi}{2} \rho_D \left(R_{De}^4 - R_{Di}^4\right) \end{cases} \tag{2.10}$$

where ρ_D is the mass density of the disk and R_{De} and R_{Di} are respectively the external and the internal radius of the disk. The term $I_{Dd} \left(\dot{\theta}_y^2 + \dot{\theta}_z^2\right)$, given in equation (2.9), represents the rotary inertia effect and $I_{Dp}\Omega\theta_y\dot{\theta}_z$ accounts for the gyroscopic effect

Applying Lagrange's equation (2.1) to the expression of the disk kinetic energy (2.9), one gets:

$$\begin{bmatrix} \dfrac{\mathrm{d}}{\mathrm{d}t}\left(\dfrac{\partial T_D}{\partial \dot{v}}\right) - \dfrac{\partial T_D}{\partial v} \\ \dfrac{\mathrm{d}}{\mathrm{d}t}\left(\dfrac{\partial T_D}{\partial \dot{w}}\right) - \dfrac{\partial T_D}{\partial w} \\ \dfrac{\mathrm{d}}{\mathrm{d}t}\left(\dfrac{\partial T_D}{\partial \dot{\theta}_y}\right) - \dfrac{\partial T_D}{\partial \theta_y} \\ \dfrac{\mathrm{d}}{\mathrm{d}t}\left(\dfrac{\partial T_D}{\partial \dot{\theta}_z}\right) - \dfrac{\partial T_D}{\partial \theta_z} \end{bmatrix} = \begin{bmatrix} m_D & 0 & 0 & 0 \\ 0 & m_D & 0 & 0 \\ 0 & 0 & I_{Dd} & 0 \\ 0 & 0 & 0 & I_{Dd} \end{bmatrix} \begin{Bmatrix} \ddot{v} \\ \ddot{w} \\ \ddot{\theta}_y \\ \ddot{\theta}_z \end{Bmatrix} + \begin{bmatrix} 0 & 0 & 0 & 0 \\ 0 & 0 & 0 & 0 \\ 0 & 0 & 0 & -\Omega I_{Dp} \\ 0 & 0 & \Omega I_{Dp} & 0 \end{bmatrix} \begin{Bmatrix} \dot{v} \\ \dot{w} \\ \dot{\theta}_y \\ \dot{\theta}_z \end{Bmatrix} \tag{2.11}$$

The governing equation of motion for rotating rigid disk can be written as:

$$[M_D]\{\ddot{q}\} + [G_D(\Omega)]\{\dot{q}\} = \{Q_D\} \tag{2.12}$$

where the disk displacement vector $\{q\}$ is given by:

$$\{q\} = \begin{Bmatrix} v & w & \theta_y & \theta_z \end{Bmatrix}^{\mathrm{T}} \tag{2.13}$$

and $\{Q_D\}$ represents the forces and moments that act on the disk which can be resulted from mass unbalance, skew position of the disk on the shaft, interconnection forces and other external effects [Muslmani, 2013]. $[M_D]$ and $[G_D(\Omega)]$, given in equation (2.12), are respectively the mass matrix and the gyroscopic matrix of the disk and are defined as follows:

$$[M_D] = \begin{bmatrix} m_D & 0 & 0 & 0 \\ 0 & m_D & 0 & 0 \\ 0 & 0 & I_{Dd} & 0 \\ 0 & 0 & 0 & I_{Dd} \end{bmatrix} \tag{2.14}$$

$$[G_D(\Omega)] = \begin{bmatrix} 0 & 0 & 0 & 0 \\ 0 & 0 & 0 & 0 \\ 0 & 0 & 0 & -\Omega I_{Dp} \\ 0 & 0 & \Omega I_{Dp} & 0 \end{bmatrix} \tag{2.15}$$

The antisymmetry of the angular velocity dependent gyroscopic matrix $[G_D(\Omega)]$ represents the movement coupling between two planes.

2.4 Mass unbalance

In fact, the main reason of rotor vibrations is the excitation due to the inevitable mass unbalance. The unbalance occurs due to several reasons such as: manufacturing error, thermal deformation and material inhomogeneity.

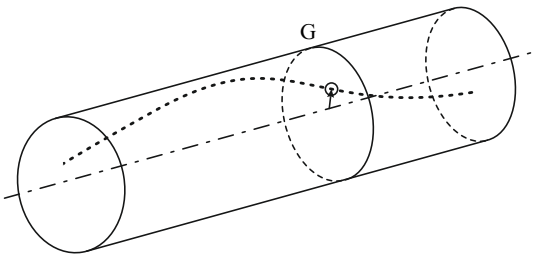

Figure 2.4. Unbalance in a rotor

The unbalance is defined in this work by a mass m_u which is located at a distance d from the geometric center of the shaft C as shown in figure 2.5.

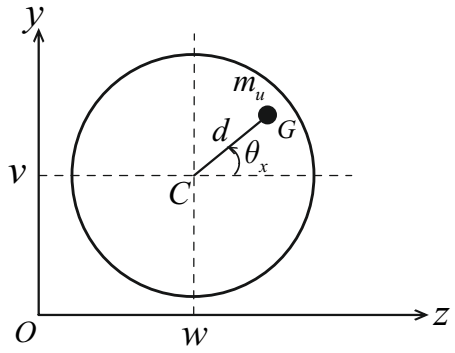

Figure 2.5. Position of the mass unbalance

The mass unbalance remains in a plane perpendicular to x axis and the coordinate along this axis is constant as shown in figure 2.5. The coordinates of the mass unbalance in the reference frame R_0 are defined as:

$$OG_{/R_0} = OC + CG = \begin{Bmatrix} u\,(x,t) + x_c \\ v\,(x,t) + d\sin\theta_x \\ w\,(x,t) + d\cos\theta_x \end{Bmatrix} \tag{2.16}$$

Thus, the velocity of the mass unbalance is defined as:

$$V_{G/R_0} = \frac{\mathrm{d}OG}{\mathrm{d}t} = \begin{Bmatrix} \dot{u} \\ \dot{v} + d\dot{\theta}_x\cos\theta_x \\ \dot{w} - d\dot{\theta}_x\sin\theta_x \end{Bmatrix} \tag{2.17}$$

In equation (2.17), the angular velocity θ_x is assumed constant where $\theta_x = \Omega t$, therefore $\dot{\theta}_x = \Omega$. Therefore, the velocity of the mass unbalance can be written as:

$$V_{G/R_0} = \begin{Bmatrix} \dot{u} \\ \dot{v} + d\Omega\cos(\Omega t) \\ \dot{w} - d\Omega\sin(\Omega t) \end{Bmatrix} \tag{2.18}$$

The kinetic energy T_u of the mass unbalance is determined as follows:

$$\begin{aligned} T_u &= \frac{1}{2} m_u \|V_{G/R_0}\|^2 \\ &= \frac{1}{2} m_u \Big(\dot{u}^2 + \dot{v}^2 + \dot{w}^2 + d^2\Omega^2 + 2d\Omega \cos(\Omega t)\, \dot{v} - 2d\Omega \sin(\Omega t)\, \dot{w} \Big) \end{aligned} \tag{2.19}$$

In equation (2.19), the mass unbalance is much smaller than the rotor mass. So, the first, second and third terms can be neglected. In other hand, the fourth term is constant and has no influence on the equation. This leads to the following equation of the kinetic energy of the mass unbalance:

$$T_u = m_u d\Omega \Big(\cos(\Omega t)\, \dot{v} - \sin(\Omega t)\, \dot{w} \Big) \tag{2.20}$$

The application of Lagrange's equation (2.1) to the expression of the mass unbalance kinetic energy (2.20) gives:

$$\begin{cases} \dfrac{\mathrm{d}}{\mathrm{d}t}\left(\dfrac{\partial T_u}{\partial \dot{v}}\right) - \dfrac{\partial T_u}{\partial v} = -m_u d\Omega^2 \sin(\Omega t) \\ \dfrac{\mathrm{d}}{\mathrm{d}t}\left(\dfrac{\partial T_u}{\partial \dot{w}}\right) - \dfrac{\partial T_u}{\partial w} = -m_u d\Omega^2 \cos(\Omega t) \end{cases} \tag{2.21}$$

Therefore, the resulting mass unbalance force is:

$$\{Q(t)\} = \begin{Bmatrix} -m_u d\Omega^2 \sin(\Omega t) \\ -m_u d\Omega^2 \cos(\Omega t) \end{Bmatrix} \tag{2.22}$$

which can be written as:

$$\begin{aligned} \{Q(t)\} &= \Re\left(\Omega^2 \begin{Bmatrix} \mathrm{j} m_u d \\ -m_u d \end{Bmatrix} \mathrm{e}^{\mathrm{j}\Omega t} \right) \\ &= \Re\Big(\Omega^2 \{b_0\} \mathrm{e}^{\mathrm{j}\Omega t} \Big) \end{aligned} \tag{2.23}$$

where $\Re$ represents the real solution part and $\Omega^2 \{b_0\}$ represents the force vector that is acting because of the mass unbalance where $\{b_0\}$ is a complex vector.

2.5 Bearings

Usually, bearings are considered as flexible elements and they are mathematically modeled as springs and dampers along y and z directions and by cross terms as shown in figure 2.6. The nonlinear relationship between load and deflection in most bearing types makes the analysis more complex. Therefore, in order to avoid this complexity in rotor dynamic analysis, the relation between the linear load and the deflection of the bearing can be assumed [Muslmani, 2013].

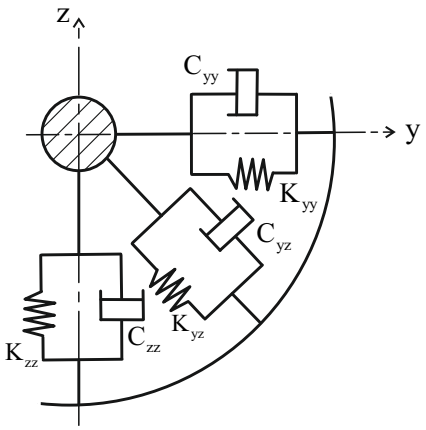

Figure 2.6. Bearing mathematical model

The virtual work δW of the bearings supporting the shaft is [Lalanne and Ferraris, 1990]:

$$\delta W = -K_{yy}v\delta v - K_{yz}w\delta v - K_{zz}w\delta w - K_{zy}v\delta w - C_{yy}\dot{v}\delta v - C_{yz}\dot{w}\delta v - C_{zz}\dot{w}\delta w - C_{zy}\dot{v}\delta w \quad (2.24)$$

which can be written as:

$$\delta W = Q_y\delta v + Q_z\delta w \quad (2.25)$$

where Q_y and Q_z are the components of the generalized force that acts on the shaft by the bearing, defined as:

$$\begin{Bmatrix} Q_y \\ Q_z \end{Bmatrix} = -\begin{bmatrix} k_{yy} & k_{yz} \\ k_{zy} & k_{zz} \end{bmatrix}\begin{Bmatrix} v \\ w \end{Bmatrix} - \begin{bmatrix} c_{yy} & c_{yz} \\ c_{zy} & c_{zz} \end{bmatrix}\begin{Bmatrix} \dot{v} \\ \dot{w} \end{Bmatrix} \quad (2.26)$$

Equation (2.26) can be expressed in the following form:

$$[C_B]\{\dot{q}\} + [K_B]\{q\} = \{Q_B\} \quad (2.27)$$

where $[C_B]$ and $[K_B]$ are respectively the damping and the stiffness matrices of the bearing, $\{Q_B\}$ is the bearing force, defined as:

$$\{Q_B\} = \begin{Bmatrix} Q_y \\ Q_z \end{Bmatrix} \quad (2.28)$$

and $\{q\}$ is the bearing displacement vector, given by:

$$\{q\} = \begin{Bmatrix} v & w \end{Bmatrix}^{\mathrm{T}} \quad (2.29)$$

In general form, when the damping and the stiffness of bearings are in function of the shaft rotational speed Ω, equation (2.27) can be written as follows:

$$[C_B(\Omega)]\{\dot{q}\} + [K_B(\Omega)]\{q\} = \{Q_B\} \quad (2.30)$$

Chapter 3

Finite Element Formulation Based on Equivalent Single Layer Theory

3.1 Introduction

This chapter is dedicated to the mathematical modeling of the dynamic behaviour analysis of rotating composite shafts. It concerns the theoretical approach of the shaft characterization which is considered as a beam with circular cross section where the translatory, rotary inertia and gyroscopic effects are taken into account. The rotating shaft made of composite material is modeled using Timoshenko beam theory and laminate theory. Timoshenko assumption states that the beam cross section is not deformable, does not remain perpendicular to the neutral axis after deformation, i.e, there are rotations for the straight section, and that shearing effect as well as rotary inertia are taken into account (see figure 3.1). In general, a structural element where one of its dimensions (length) is greater than the two others can be considered as a beam. It should be noted that this type of beam element is called 'shaft' when it has a rotational movement or when it is subjected to the torsion. The shaft is assumed to rotate at constant speed about its longitudinal axis x.

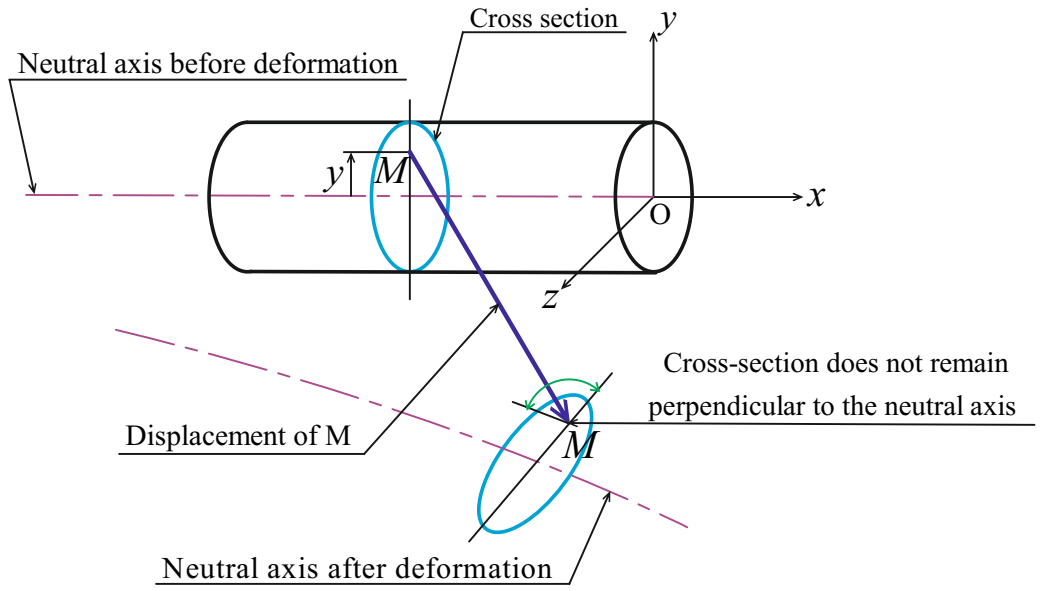

Figure 3.1. Shaft structure before and after deformation

The studied laminated composite shaft can be obtained by stacking several layers with different fiber orientations in different sequences as shown in figure 3.2.

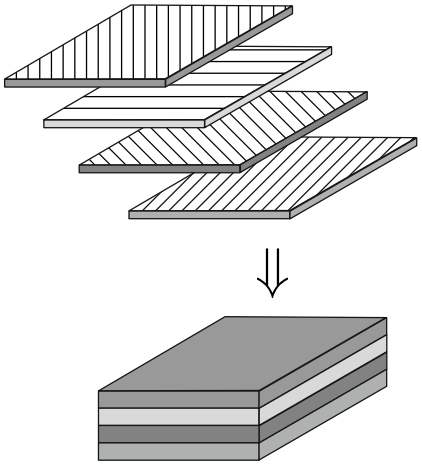

Figure 3.2. Stacking sequence made up of several layers with different fiber orientations

In this chapter, Equivalent Single Layer Theory (ESLT) formulation is proposed to analyse the dynamic behaviour of rotating composite shafts. The developed ESLT consists on defining an equivalent single layer having equivalent mechanical properties of all the orthotropic layers of the laminated shaft. Moreover, this theory is developed to avoid the main drawbacks associated with formulation that does not consider the effects of stacking sequence like Equivalent Modulus Beam Theory (EMBT) developed by [Singh and Gupta, 1996a,b] and formulations which do not take account of the shear-normal coupling effect like EMBT developed by [Singh and Gupta, 1996a,b] and Simplified Homogenized Beam Theory (SHBT) developed by [Sino et al., 2008]. In fact, ESLT formulation takes into account the location and the orientation of different layers and their stacking sequence. Furthermore, the shear-normal coupling effect is introduced directly in this formulation unlike the Modified Equivalent Modulus Beam Theory (Modified EMBT) formulation proposed by [Gubran and Gupta, 2005] where the shear-normal coupling effect is introduced by modifying the expression of the equivalent longitudinal Young's modulus. Here, the relevant strain-displacement and the constitutive relations for laminated composite shafts are directly derived from those of three-dimensional through multiple coordinate transformations and the extended Hamilton's principle is used to derive the differential equation of motion. It can be mathematically stated as:

$$\delta \int_{t_i}^{t_f} (\mathcal{L} + \mathcal{W}) \, \mathrm{d}t = 0 \tag{3.1}$$

where $\mathcal{L}$ is known as the Lagrangian density function or Lagrangian functional and $\mathcal{W}$ represents the work done on the system by non-conservative forces which is not considered in this study.

The Lagrangian functional $\mathcal{L}$ is related to both kinetic and deformation energies denoted respectively T and Π and it is given by the following equation:

$$\mathcal{L} = T - \Pi \tag{3.2}$$

Substituting equation (3.2) in equation (3.1) and considering that variational and integration operators

are interchangeable, Hamilton's principle can thereby be stated as:

$$\int_{t_i}^{t_f} (\delta T - \delta \Pi)\, \mathrm{d}t = 0 \tag{3.3}$$

To determine the kinetic energy of a given mechanical system in a rotational movement, one needs to know the velocity field of the system, which implies knowing the velocity of any generic point through a set of generalized coordinates. Let consider v_M as the velocity vector of any generic point M of the mechanical system and ρ as the material mass density, the kinetic energy T can be determined as follows:

$$T = \frac{1}{2} \int_V \rho v_M^{\mathrm{T}} v_M \mathrm{d}V \tag{3.4}$$

As for the deformation energy, it can be calculated by determining the strain and stress fields of the system. The deformation energy Π is determined using the following expression:

$$\Pi = \frac{1}{2} \int_V \varepsilon^{\mathrm{T}} \sigma \mathrm{d}V \tag{3.5}$$

where ε is the strain field and σ is the stress field. In fact, the strain field is derived from the displacement field using Green's tensor whereas the stress field is calculated using the strains and the elastic constants from the generalized Hooke's law.

3.2 Equivalent Single Layer Theory modeling

Let consider a multilayered composite shaft made of P orthotropic layers as shown in figure 3.3. The laminated composite shaft can be obtained by winding several layers of embedded fibers on a mandrel.

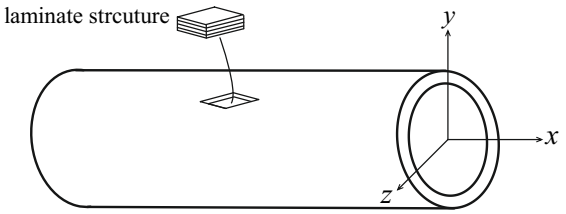

Figure 3.3. Composite shaft

The composite shaft cross section is presented in figure 3.4.

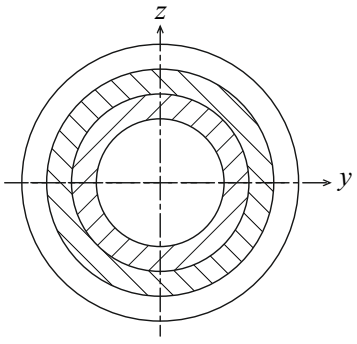

Figure 3.4. Composite shaft cross section

Equivalent Single Layer Theory (ESLT) developed in this work is based on the following assumptions:

- Material of each layer is linearly elastic and has two planes of material symmetry (orthotropic);
- Each layer is of uniform thickness;
- All layers are perfectly bonded together at each interface;
- The displacement field is linear in each layer and continuous at each layer interface.

3.2.1 Displacement field

Considering x as the shaft neutral axis. The continuous displacement field at material points along the shaft cross section is described as follows:

$$\{U(x,y,z,t)\} = \begin{Bmatrix} u_x(x,y,z,t) \\ u_y(x,y,z,t) \\ u_z(x,y,z,t) \end{Bmatrix} = \begin{Bmatrix} -y\theta_z(x,t) + z\theta_y(x,t) \\ v(x,t) \\ w(x,t) \end{Bmatrix} \tag{3.6}$$

where u_x, u_y and u_z are the displacements of a generic point of the shaft cross section along x, y and z directions respectively. The variables $v(x,t)$ and $w(x,t)$ denote respectively the flexural displacements in y and z directions of the point on the reference axis of the shaft, while $\theta_y(x,t)$ and $\theta_z(x,t)$ are the rotation angles of the cross section around y and z axes respectively.

3.2.2 Strain field

Green's strain tensor also known as Green-Lagrange strain tensor, which was first introduced by Green and St. Venant, is given by the following equation:

$$L_{ij} = \frac{1}{2}\left(\frac{\partial u_i}{\partial x_j} + \frac{\partial u_j}{\partial x_i} + \frac{\partial u_k}{\partial x_i}\frac{\partial u_k}{\partial x_j}\right) \tag{3.7}$$

For small deformations, the displacement gradients ${}^{\partial u_i}/_{\partial x_j}$ are small and the quadratic term of L_{ij} can be neglected. Therefore, the simplified strain field expression is given by:

$$\varepsilon_{ij} = \frac{1}{2}\left(\frac{\partial u_i}{\partial x_j} + \frac{\partial u_j}{\partial x_i}\right) \tag{3.8}$$

Denoting respectively u_1, u_2, u_3 as u_x, u_y, u_z and x_1, x_2, x_3 as x, y, z, one gets the strain tensor expression as follows:

$$\{\varepsilon\} = \begin{cases} \varepsilon_{xx} = \dfrac{\partial u_x}{\partial x} \\ \varepsilon_{yy} = \dfrac{\partial u_y}{\partial y} \\ \varepsilon_{zz} = \dfrac{\partial u_z}{\partial z} \\ \gamma_{xy} = 2\varepsilon_{xy} = \dfrac{\partial u_x}{\partial y} + \dfrac{\partial u_y}{\partial x} \\ \gamma_{xz} = 2\varepsilon_{xz} = \dfrac{\partial u_x}{\partial z} + \dfrac{\partial u_z}{\partial x} \\ \gamma_{yz} = 2\varepsilon_{yz} = \dfrac{\partial u_y}{\partial z} + \dfrac{\partial u_z}{\partial y} \end{cases} \tag{3.9}$$

Using equation (3.9) and the displacement field expression (3.6), the strain field expressed in the cartesian coordinate system (x, y, z) has the following form:

$$\{\varepsilon\} = \begin{cases} \varepsilon_{xx} = -y\dfrac{\partial \theta_z}{\partial x} + z\dfrac{\partial \theta_y}{\partial x} \\ \gamma_{xy} = -\theta_z + \dfrac{\partial v}{\partial x} \\ \gamma_{xz} = \theta_y + \dfrac{\partial w}{\partial x} \\ \varepsilon_{yy} = \varepsilon_{zz} = \gamma_{yz} = 0 \end{cases} \tag{3.10}$$

Since the shape of the shaft cross section is assumed circular, it is more convenient to express the stress-strain relations in the cylindrical coordinate system (x, r, ϕ). The strain components in the cylindrical coordinate system can be expressed in terms of their counterparts in the cartesian coordinate system through a transformation matrix (see figure 3.5) as follows:

$$\begin{Bmatrix} \varepsilon_{xx} \\ \varepsilon_{\phi\phi} \\ \varepsilon_{rr} \\ \gamma_{x\phi} \\ \gamma_{r\phi} \\ \gamma_{xr} \end{Bmatrix} = \begin{bmatrix} 1 & 0 & 0 & 0 & 0 & 0 \\ 0 & \sin^2\phi & \cos^2\phi & 0 & -2\cos\phi\sin\phi & 0 \\ 0 & \cos^2\phi & \sin^2\phi & 0 & 2\cos\phi\sin\phi & 0 \\ 0 & 0 & 0 & -\sin\phi & 0 & \cos\phi \\ 0 & -\cos\phi\sin\phi & \cos\phi\sin\phi & 0 & \cos^2\phi - \sin^2\phi & 0 \\ 0 & 0 & 0 & \cos\phi & 0 & \sin\phi \end{bmatrix} \begin{Bmatrix} \varepsilon_{xx} \\ \varepsilon_{yy} \\ \varepsilon_{zz} \\ \gamma_{xy} \\ \gamma_{yz} \\ \gamma_{xz} \end{Bmatrix} \tag{3.11}$$

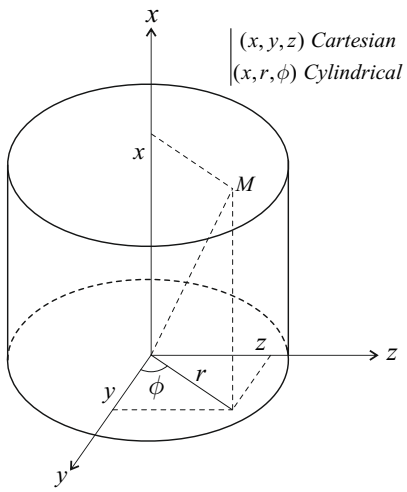

Figure 3.5. Transformation to cylindrical coordinate system (x, r, ϕ)

Considering the strain field expression (3.10) in the cartesian coordinate system (x, y, z) and equation (3.11), the strain components in the cylindrical coordinate system (x, r, ϕ) can be written as follows:

$$\{\varepsilon\} = \begin{cases} \varepsilon_{xx} = -y\dfrac{\partial \theta_z}{\partial x} + z\dfrac{\partial \theta_y}{\partial x} \\ \gamma_{x\phi} = -\gamma_{xy}\sin\phi + \gamma_{xz}\cos\phi \\ \gamma_{xr} = \gamma_{xy}\cos\phi + \gamma_{xz}\sin\phi \\ \varepsilon_{rr} = \varepsilon_{\phi\phi} = \gamma_{r\phi} = 0 \end{cases} \tag{3.12}$$

3.2.3 Stress field

The generalized Hooke's law for an orthotropic material is given by:

$$\{\sigma\} = [Q]\,\{\varepsilon\} \tag{3.13}$$

where $\{\sigma\}$ and $\{\varepsilon\}$ are respectively the stress and strain fields and $[Q]$ is the material stiffness matrix. When linked to the orthotropic axis, equation (3.13) can be written in the matrix form as follows:

$$\begin{Bmatrix} \sigma_{11} \\ \sigma_{22} \\ \sigma_{33} \\ \tau_{23} \\ \tau_{31} \\ \tau_{12} \end{Bmatrix} = \begin{bmatrix} \frac{E_1}{1-\nu_{12}\nu_{21}} & \frac{\nu_{12}E_2}{1-\nu_{12}\nu_{21}} & Q_{13} & 0 & 0 & 0 \\ \frac{\nu_{12}E_2}{1-\nu_{12}\nu_{21}} & \frac{E_2}{1-\nu_{12}\nu_{21}} & Q_{23} & 0 & 0 & 0 \\ Q_{13} & Q_{23} & Q_{33} & 0 & 0 & 0 \\ 0 & 0 & 0 & G_{23} & 0 & 0 \\ 0 & 0 & 0 & 0 & G_{13} & 0 \\ 0 & 0 & 0 & 0 & 0 & G_{12} \end{bmatrix} \begin{Bmatrix} \varepsilon_{11} \\ \varepsilon_{22} \\ \varepsilon_{33} \\ \gamma_{23} \\ \gamma_{31} \\ \gamma_{12} \end{Bmatrix} \tag{3.14}$$

where $(1, 2, 3)$ are the orthotropic axes: 1 is the fiber direction, 2 is the transverse direction of the fiber and 3 is the perpendicular direction to the layer as shown in figure 3.6. The following parameters have to be identified for each layer in the orthotropic axes: E_1 and E_2 are Young's modulus, ν_{12} and ν_{21} are Poisson's ratios and G_{23}, G_{13} and G_{12} are transversal shear modulus. When considering the transversal shear effects, it is usually difficult to estimate the shear modulus G_{23} and G_{13}. Hence, G_{23} and G_{13} are assumed equal to G_{12} [Sino et al., 2008].

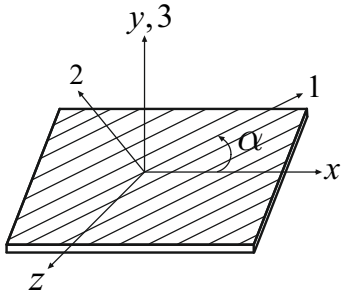

Figure 3.6. Plane of the orthotropic layer

Let consider an arbitrary layer of the laminate whose fiber orientation makes an angle α with respect to the x axis of the cylindrical coordinate system (x, r, ϕ) as shown in figure 3.7.

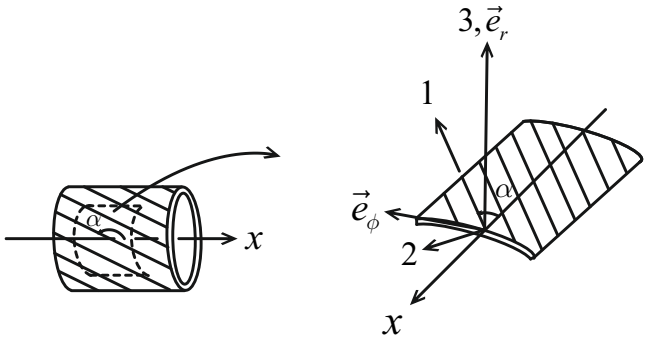

Figure 3.7. Principal material coordinate axes on an arbitrary orthotropic layer

The stress-strain relations expressed in this chosen cylindrical coordinate system are given by:

$$\begin{Bmatrix} \sigma_{xx} \\ \sigma_{\phi\phi} \\ \sigma_{rr} \\ \tau_{r\phi} \\ \tau_{xr} \\ \tau_{x\phi} \end{Bmatrix} = \begin{bmatrix} \bar{Q}_{11} & \bar{Q}_{12} & \bar{Q}_{13} & 0 & 0 & \bar{Q}_{16} \\ \bar{Q}_{12} & \bar{Q}_{22} & \bar{Q}_{23} & 0 & 0 & \bar{Q}_{26} \\ \bar{Q}_{13} & \bar{Q}_{23} & \bar{Q}_{33} & 0 & 0 & \bar{Q}_{36} \\ 0 & 0 & 0 & \bar{Q}_{44} & \bar{Q}_{45} & 0 \\ 0 & 0 & 0 & \bar{Q}_{45} & \bar{Q}_{55} & 0 \\ \bar{Q}_{16} & \bar{Q}_{26} & \bar{Q}_{36} & 0 & 0 & \bar{Q}_{66} \end{bmatrix} \begin{Bmatrix} \varepsilon_{xx} \\ \varepsilon_{\phi\phi} \\ \varepsilon_{rr} \\ \gamma_{r\phi} \\ \gamma_{xr} \\ \gamma_{x\phi} \end{Bmatrix} \tag{3.15}$$

The above equation (3.15) can be expressed in abbreviated form as follows:

$$\{\sigma\} = \left[\bar{Q}\right] \{\varepsilon\} \tag{3.16}$$

where $\left[\bar{Q}\right]$ is the transformed material stiffness matrix of the layer, expressed as [Reddy, 1997]:

$$\left[\bar{Q}\right] = [T]^{\mathrm{T}} [Q] [T] \tag{3.17}$$

where the transformation matrix $[T]$ is given by:

$$[T] = \begin{bmatrix} \cos^2\alpha & \sin^2\alpha & 0 & 0 & 0 & \cos\alpha\sin\alpha \\ \sin^2\alpha & \cos^2\alpha & 0 & 0 & 0 & -\cos\alpha\sin\alpha \\ 0 & 0 & 1 & 0 & 0 & 0 \\ 0 & 0 & 0 & \cos\alpha & -\sin\alpha & 0 \\ 0 & 0 & 0 & \sin\alpha & \cos\alpha & 0 \\ -2\cos\alpha\sin\alpha & 2\cos\alpha\sin\alpha & 0 & 0 & 0 & \cos^2\alpha - \sin^2\alpha \end{bmatrix} \tag{3.18}$$

3.2.4 Deformation energy

The laminated shaft deformation energy is given by:

$$\begin{aligned} \Pi &= \frac{1}{2}\int_V \varepsilon^{\mathrm{T}}\sigma \mathrm{d}V \\ &= \frac{1}{2}\int_V \left(\sigma_{xx}\varepsilon_{xx} + \sigma_{\phi\phi}\varepsilon_{\phi\phi} + \sigma_{rr}\varepsilon_{rr} + \tau_{r\phi}\gamma_{r\phi} + \tau_{xr}\gamma_{xr} + \tau_{x\phi}\gamma_{x\phi}\right) \mathrm{d}V \end{aligned} \tag{3.19}$$

Since $\varepsilon_{\phi\phi} = \varepsilon_{rr} = \gamma_{r\phi} = 0$, the laminated shaft deformation energy can be expressed as follows:

$$\Pi = \frac{1}{2}\int_V \left(\sigma_{xx}\varepsilon_{xx} + \tau_{xr}\gamma_{xr} + \tau_{x\phi}\gamma_{x\phi}\right) \mathrm{d}V \tag{3.20}$$

and the stress-strain relation expressed in equation (3.15) can be simplified as follows:

$$\begin{Bmatrix} \sigma_{xx} \\ \tau_{xr} \\ \tau_{x\phi} \end{Bmatrix} = \begin{bmatrix} \bar{Q}_{11} & 0 & \bar{Q}_{16} \\ 0 & \bar{Q}_{55} & 0 \\ \bar{Q}_{16} & 0 & \bar{Q}_{66} \end{bmatrix} \begin{Bmatrix} \varepsilon_{xx} \\ \gamma_{xr} \\ \gamma_{x\phi} \end{Bmatrix} \tag{3.21}$$

Therefore, the stress components are expressed as follows:

$$\{\sigma\} = \begin{cases} \sigma_{xx} = \bar{Q}_{11}\varepsilon_{xx} + k_s\bar{Q}_{16}\gamma_{x\phi} \\ \tau_{xr} = k_s\bar{Q}_{55}\gamma_{xr} \\ \tau_{x\phi} = k_s\bar{Q}_{16}\varepsilon_{xx} + k_s\bar{Q}_{66}\gamma_{x\phi} \end{cases} \tag{3.22}$$

where k_s is the transverse shear correction factor and $\bar{Q}_{ij}$ are the constitutive terms which are related to the laminate angle α and the elastic constants of principal axes as follows:

$$\begin{cases} \bar{Q}_{11} = Q_{11}\cos^4\alpha + Q_{22}\sin^4\alpha + (2Q_{12} + 4Q_{66})\cos^2\alpha\sin^2\alpha \\ \bar{Q}_{16} = Q_{11}\cos^3\alpha\sin\alpha - Q_{22}\cos\alpha\sin^3\alpha + (Q_{12} + 2Q_{66})\left(\cos\alpha\sin^3\alpha - \cos^3\alpha\sin\alpha\right) \\ \bar{Q}_{55} = Q_{44}\sin^2\alpha + Q_{55}\cos^2\alpha \\ \bar{Q}_{66} = (Q_{11} + Q_{22} - 2Q_{12})\cos^2\alpha\sin^2\alpha + Q_{66}(\cos^2\alpha - \sin^2\alpha)^2 \end{cases} \tag{3.23}$$

Using equations (3.20) and (3.22), the laminated shaft deformation energy can be written as:

$$\Pi = \frac{1}{2}\int_V \left(\bar{Q}_{11}\varepsilon_{xx}^2 + 2k_s\bar{Q}_{16}\gamma_{x\phi}\varepsilon_{xx} + k_s\bar{Q}_{55}\gamma_{xr}^2 + k_s\bar{Q}_{66}\gamma_{x\phi}^2\right)\mathrm{d}V \tag{3.24}$$

where $2k_s\bar{Q}_{16}\gamma_{x\phi}\varepsilon_{xx}$ accounts for the shear-normal coupling effect. Substituting the relations for the cross section rotation where $y = r\cos\phi$ and $z = r\sin\phi$ as shown in figure 3.5 and integrating over the shaft cross sectional area by summing up the contribution of each orthotropic layer, the composite shaft deformation energy can be expressed as:

$$\begin{aligned} \Pi = {} & \frac{1}{2}A_{11}\int_0^L \left[\left(\frac{\partial\theta_y}{\partial x}\right)^2 + \left(\frac{\partial\theta_z}{\partial x}\right)^2\right]\mathrm{d}x + \frac{1}{2}k_sA_{16}\int_0^L \left[-\theta_y\frac{\partial\theta_z}{\partial x} - \frac{\partial\theta_z}{\partial x}\frac{\partial w}{\partial x} + \theta_z\frac{\partial\theta_y}{\partial x} - \frac{\partial\theta_y}{\partial x}\frac{\partial v}{\partial x}\right]\mathrm{d}x \\ & + \frac{1}{2}k_s\left(A_{55} + A_{66}\right)\int_0^L \left[\left(\frac{\partial v}{\partial x}\right)^2 + \left(\frac{\partial w}{\partial x}\right)^2 + \theta_y^2 + \theta_z^2 + 2\theta_y\frac{\partial w}{\partial x} - 2\theta_z\frac{\partial v}{\partial x}\right]\mathrm{d}x \end{aligned} \tag{3.25}$$

where L is the length of the composite shaft. Let consider the pth layer of the composite shaft where R_{p-1} is the inner radius and R_p is the outer radius as shown in figure 3.8.

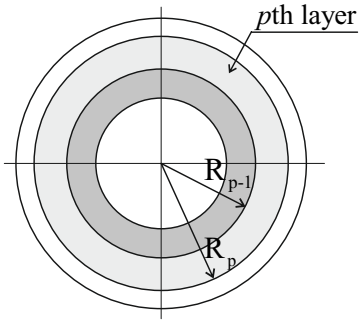

Figure 3.8. Inner and outer radius of the pth layer of the composite shaft

The terms A_{ij} of equation (3.25) are given as follows:

$$\begin{cases} A_{11} = \dfrac{\pi}{4}\displaystyle\sum_{p=1}^{P} \bar{Q}_{11p}\left(R_p^4 - R_{p-1}^4\right) \\ A_{16} = \dfrac{2\pi}{3}\displaystyle\sum_{p=1}^{P} \bar{Q}_{16p}\left(R_p^3 - R_{p-1}^3\right) \\ A_{55} = \dfrac{\pi}{2}\displaystyle\sum_{p=1}^{P} \bar{Q}_{55p}\left(R_p^2 - R_{p-1}^2\right) \\ A_{66} = \dfrac{\pi}{2}\displaystyle\sum_{p=1}^{P} \bar{Q}_{66p}\left(R_p^2 - R_{p-1}^2\right) \end{cases} \tag{3.26}$$

3.2.5 Kinetic energy

The kinetic energy of the rotating laminated shaft including the translatory, rotary inertia and gyroscopic effects is given by:

$$T = \frac{1}{2}\int_0^L \rho A\left(\dot{v}^2 + \dot{w}^2\right)\mathrm{d}x + \frac{1}{2}\int_0^L \rho \Gamma_{R/R_0}.\Big(\left[J_{/C}\right]\Gamma_{R/R_0}\Big)\mathrm{d}x \tag{3.27}$$

where ρ is the mass density of the composite shaft, A is the shaft cross sectional area and v and w denote the coordinates of the point C in y and z directions on the shaft reference axis as shown in figure 2.2. The coordinate along x being constant. The tensor of inertia in C, as xyz are principal directions of inertia and considering the symmetry, is given by:

$$\left[J_{/C}\right] = \begin{bmatrix} I_x & 0 & 0 \\ 0 & I_y & 0 \\ 0 & 0 & I_y \end{bmatrix} \tag{3.28}$$

The angular velocity vector, given in equation (2.4), is:

$$\Gamma_{R/R_0} = \begin{Bmatrix} \dot{\theta}_x - \dot{\theta}_z \sin\theta_y \\ -\dot{\theta}_z \cos\theta_y \sin\theta_x + \dot{\theta}_y \cos\theta_x \\ \dot{\theta}_z \cos\theta_y \cos\theta_x + \dot{\theta}_y \sin\theta_x \end{Bmatrix} \tag{3.29}$$

So, using the composite shaft kinetic energy expression (3.27), the tensor of inertia expression (3.28) and the angular velocity vector expression (3.29), the rotating composite shaft kinetic energy can be written as:

$$\begin{aligned} T = \frac{1}{2}\int_0^L \Big[& \rho A\left(\dot{v}^2 + \dot{w}^2\right) + \rho I_x\left(\dot{\theta}_x^2 - 2\dot{\theta}_x\dot{\theta}_z\sin\theta_y + \dot{\theta}_z^2\sin^2\theta_y\right) \\ & + \rho I_y\left(\dot{\theta}_z^2\cos^2\theta_y\sin^2\theta_x + \dot{\theta}_y^2\cos^2\theta_x + \dot{\theta}_z^2\cos^2\theta_y\cos^2\theta_x + \dot{\theta}_y^2\sin^2\theta_x\right)\Big]\mathrm{d}x \end{aligned} \tag{3.30}$$

In equation (3.30), the angles θ_y and θ_z are assumed small and the angular velocity is assumed constant $\dot{\theta}_x = \Omega$. Integrating over the shaft cross sectional area by summing up the contribution of each

orthotropic layer, the kinetic energy of the rotating laminated shaft including the effects of translatory and rotary inertia as well as the gyroscopic ones can be simplified as follow:

$$T = \frac{1}{2}\int_0^L \left[I_m \left(\dot{v}^2 + \dot{w}^2\right) + I_d\left(\dot{\theta}_y^2 + \dot{\theta}_z^2\right) - 2I_p\Omega\theta_y\dot{\theta}_z + I_p\Omega^2 \right] \mathrm{d}x \tag{3.31}$$

where $I_d\left(\dot{\theta}_y^2 + \dot{\theta}_z^2\right)$ represents the rotary inertia effect and $2I_p\Omega\theta_y\dot{\theta}_z$ accounts for the gyroscopic effect. The mass quantity I_m denotes the mass per unit length of the composite shaft, while I_d and I_p denote respectively the diametrical and the polar moment of inertia of the shaft cross section, defined as:

$$\begin{cases} I_m = \pi \displaystyle\sum_{p=1}^{P} \rho_p \left(R_p^2 - R_{p-1}^2\right) \\ I_d = \dfrac{\pi}{4} \displaystyle\sum_{p=1}^{P} \rho_p \left(R_p^4 - R_{p-1}^4\right) \\ I_p = \dfrac{\pi}{2} \displaystyle\sum_{p=1}^{P} \rho_p \left(R_p^4 - R_{p-1}^4\right) \end{cases} \tag{3.32}$$

3.2.6 Variational formulation

Hamilton's principle is herein adopted (see section 3.1):

$$\delta \int_{t_i}^{t_f} (T - \Pi)\, \mathrm{d}t = 0 \tag{3.33}$$

Introducing kinetic energy T expression (3.31) and deformation energy Π expression (3.25) into Hamilton's principle (3.33) and performing the variation and an integration by parts, and since the above stated Hamilton's principle must be verified for an arbitrary $\{\delta d\} = \{\delta v, \delta w, \delta\theta_y, \delta\theta_z\}^{\mathrm{T}}$, the variational statement can be expressed as follows:

$$\begin{aligned} &\int_0^L \left[\delta v I_m \ddot{v} + \delta w I_m \ddot{w} + \delta\theta_y I_d \ddot{\theta}_y + \delta\theta_z I_d \ddot{\theta}_z + \delta\theta_y I_p \Omega \dot{\theta}_z - \delta\theta_z I_p \Omega \dot{\theta}_y \right] \mathrm{d}x \\ &+ \int_0^L \left[\frac{\partial}{\partial x}(\delta v)\left(Q_{xr}^{(2)} - Q_{x\phi}^{(1)}\right) + \frac{\partial}{\partial x}(\delta w)\left(Q_{xr}^{(1)} + Q_{x\phi}^{(2)}\right) + \delta\theta_y\left(Q_{xr}^{(1)} + Q_{x\phi}^{(2)}\right) + \delta\theta_z\left(Q_{x\phi}^{(1)} - Q_{xr}^{(2)}\right) \right. \\ &\qquad \left. + \frac{\partial}{\partial x}(\delta\theta_y) M_y + \frac{\partial}{\partial x}(\delta\theta_z) M_z \right] \mathrm{d}x = 0 \quad \forall\, \delta v, \delta w, \delta\theta_y, \delta\theta_z \end{aligned} \tag{3.34}$$

where the stress resultants $Q_{xr}^{(1)}$, $Q_{xr}^{(2)}$, $Q_{x\phi}^{(1)}$, $Q_{x\phi}^{(2)}$ and the stress couples M_y, M_z are defined as follows:

$$\begin{cases} Q_{xr}^{(1)} = k_s A_{55}\left(\theta_y + \dfrac{\partial w}{\partial x}\right) \\ Q_{xr}^{(2)} = k_s A_{55}\left(-\theta_z + \dfrac{\partial v}{\partial x}\right) \\ Q_{x\phi}^{(1)} = \dfrac{1}{2} k_s A_{16} \dfrac{\partial\theta_y}{\partial x} + k_s A_{66}\left(\theta_z - \dfrac{\partial v}{\partial x}\right) \\ Q_{x\phi}^{(2)} = -\dfrac{1}{2} k_s A_{16} \dfrac{\partial\theta_z}{\partial x} + k_s A_{66}\left(\theta_y + \dfrac{\partial w}{\partial x}\right) \end{cases} \tag{3.35}$$

$$\begin{cases} M_y = A_{11}\dfrac{\partial \theta_y}{\partial x} + \dfrac{1}{2}k_s A_{16}\left(\theta_z - \dfrac{\partial v}{\partial x}\right) \\ M_z = A_{11}\dfrac{\partial \theta_z}{\partial x} - \dfrac{1}{2}k_s A_{16}\left(\theta_y + \dfrac{\partial w}{\partial x}\right) \end{cases} \tag{3.36}$$

3.3 Finite element modeling

In order to solve the system of differential equations using the finite element method, the shaft needs to be discretized into several elements as shown in figure 3.9.

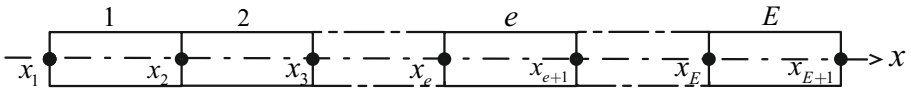

Figure 3.9. Discretization of the shaft in finite elements

It is usually convenient to define the domain of the shaft element in terms of a natural coordinate ξ rather than a system global coordinate x. So, its domain is always the same for any element of the shaft which facilitates the numerical integration of the element matrices using the Gauss quadrature. The natural coordinate system has its origin at the center of the element and the element domain is $-1 < \xi < 1$ as it is shown in figure 3.10.

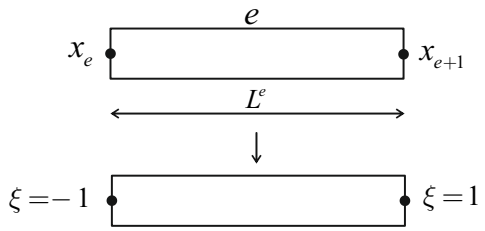

Figure 3.10. Natural coordinate

The global coordinate x can then be determined from the natural coordinate ξ as follows:

$$x(\xi) = N_1 x_e + N_2 x_{e+1} = \begin{bmatrix} N_1 & N_2 \end{bmatrix} \begin{bmatrix} x_e \\ x_{e+1} \end{bmatrix} \tag{3.37}$$

where N_1 and N_2 are the shape functions defined in the natural coordinate system that interpolate the geometry of the shaft and are given by [Hinton and Owen, 1981]:

$$N_1 = \frac{1-\xi}{2} \qquad \text{and} \qquad N_2 = \frac{1+\xi}{2} \tag{3.38}$$

To obtain the derivative of a shape function defined in the natural coordinate system with respect to the global spatial variable x, one can do as follows:

$$\frac{\mathrm{d}N}{\mathrm{d}\xi} = \frac{\mathrm{d}N}{\mathrm{d}x}\underbrace{\frac{\mathrm{d}x}{\mathrm{d}\xi}}_{J} \tag{3.39}$$

Therefore,

$$\frac{\mathrm{d}N}{\mathrm{d}x} = \frac{\mathrm{d}N}{\mathrm{d}\xi} J^{-1} \tag{3.40}$$

with J is the Jacobian of the transformation defined for the shaft element as:

$$J = \frac{\mathrm{d}}{\mathrm{d}\xi}\left(\begin{bmatrix} N_1 & N_2 \end{bmatrix} \begin{bmatrix} x_e \\ x_{e+1} \end{bmatrix} \right) = \begin{bmatrix} \frac{\mathrm{d}N_1}{\mathrm{d}\xi} & \frac{\mathrm{d}N_2}{\mathrm{d}\xi} \end{bmatrix} \begin{bmatrix} x_e \\ x_{e+1} \end{bmatrix} \tag{3.41}$$

3.3.1 Finite element definition

The developed shaft finite element has two nodes as shown in figure 3.11. For each node, the element has four degrees of freedom: two displacements v and w and two slopes θ_y and θ_z about y and z axes respectively.

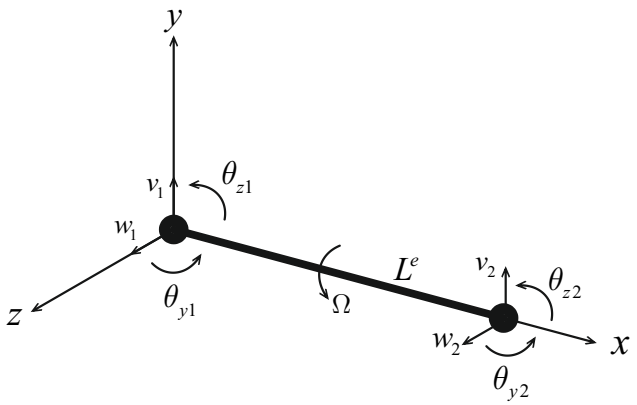

Figure 3.11. Shaft finite element

The displacement interpolations can be defined as:

$$v = \sum_{i=1}^{2} N_i v_i \qquad w = \sum_{i=1}^{2} N_i w_i \qquad \theta_y = \sum_{i=1}^{2} N_i \theta_{y_i} \qquad \theta_z = \sum_{i=1}^{2} N_i \theta_{z_i} \tag{3.42}$$

Taking a matrix notation, let:

$$v = N_v q^e \qquad w = N_w q^e \qquad \theta_y = N_{\theta_y} q^e \qquad \theta_z = N_{\theta_z} q^e \tag{3.43}$$

$$\frac{\partial v}{\partial x} = B_v q^e \qquad \frac{\partial w}{\partial x} = B_w q^e \qquad \frac{\partial \theta_y}{\partial x} = B_{\theta_y} q^e \qquad \frac{\partial \theta_z}{\partial x} = B_{\theta_z} q^e \tag{3.44}$$

where the elemental vector of nodal degrees of freedom, shape functions matrices and deformation matrices are defined as follows:

$$\{q^e\} = \begin{Bmatrix} v_1 & w_1 & \theta_{y_1} & \theta_{z_1} & v_2 & w_2 & \theta_{y_2} & \theta_{z_2} \end{Bmatrix}^{\mathrm{T}} \tag{3.45}$$

$$\begin{aligned} N_v &= \begin{bmatrix} N_1 & 0 & 0 & 0 & N_2 & 0 & 0 & 0 \end{bmatrix} \\ N_w &= \begin{bmatrix} 0 & N_1 & 0 & 0 & 0 & N_2 & 0 & 0 \end{bmatrix} \\ N_{\theta_y} &= \begin{bmatrix} 0 & 0 & N_1 & 0 & 0 & 0 & N_2 & 0 \end{bmatrix} \\ N_{\theta_z} &= \begin{bmatrix} 0 & 0 & 0 & N_1 & 0 & 0 & 0 & N_2 \end{bmatrix} \end{aligned} \tag{3.46}$$

$$
\begin{aligned}
B_v &= J^{-1}\begin{bmatrix}\frac{\partial N_1}{\partial \xi} & 0 & 0 & 0 & \frac{\partial N_2}{\partial \xi} & 0 & 0 & 0\end{bmatrix} \\
B_w &= J^{-1}\begin{bmatrix}0 & \frac{\partial N_1}{\partial \xi} & 0 & 0 & 0 & \frac{\partial N_2}{\partial \xi} & 0 & 0\end{bmatrix} \\
B_{\theta_y} &= J^{-1}\begin{bmatrix}0 & 0 & \frac{\partial N_1}{\partial \xi} & 0 & 0 & 0 & \frac{\partial N_2}{\partial \xi} & 0\end{bmatrix} \\
B_{\theta_z} &= J^{-1}\begin{bmatrix}0 & 0 & 0 & \frac{\partial N_1}{\partial \xi} & 0 & 0 & 0 & \frac{\partial N_2}{\partial \xi}\end{bmatrix}
\end{aligned}
\tag{3.47}
$$

3.3.2 Weak form finite element discretization

The global weak form described in equation (3.34) can be expressed as the sum of the elemental forms leading to the definition of the elemental matrices. Adding the contribution of all the E finite elements, the global form can be expressed as:

$$
\begin{aligned}
\sum_{e=1}^{E}\Bigg(&\int_0^{L^e}\left[\delta v I_m \ddot{v} + \delta w I_m \ddot{w} + \delta\theta_y I_d \ddot{\theta}_y + \delta\theta_z I_d \ddot{\theta}_z + \delta\theta_y I_p \Omega \dot{\theta}_z - \delta\theta_z I_p \Omega \dot{\theta}_y\right] \mathrm{d}x \\
&+ \int_0^{L^e}\Bigg[\frac{\partial}{\partial x}(\delta v)\left(Q_{xr}^{(2)} - Q_{x\phi}^{(1)}\right) + \frac{\partial}{\partial x}(\delta w)\left(Q_{xr}^{(1)} + Q_{x\phi}^{(2)}\right) + \delta\theta_y\left(Q_{xr}^{(1)} + Q_{x\phi}^{(2)}\right) \\
&\quad + \delta\theta_z\left(Q_{x\phi}^{(1)} - Q_{xr}^{(2)}\right) + \frac{\partial}{\partial x}(\delta\theta_y) M_y + \frac{\partial}{\partial x}(\delta\theta_z) M_z\Bigg] \mathrm{d}x\Bigg) = 0
\end{aligned}
\tag{3.48}
$$

where the generalized variables are restricted to the domain of integration L^e and an approximation is considered at a local level in each finite element as stated in equation (3.42).

The relation between the elemental degrees of freedom and the global ones is established through the connectivity matrices $[R^e]$, expressed as:

$$
\{q^e\} = [R^e]\{q\} \tag{3.49}
$$

where $\{q\}$ represents the vector of global degrees of freedom.

Substituting equation (3.42) into equation (3.48) yields:

$$
\sum_{e=1}^{E}\left(\{\delta q^e\}^{\mathrm{T}}[M^e]\{\ddot{q}^e\} + \{\delta q^e\}^{\mathrm{T}}[G^e(\Omega)]\{\dot{q}^e\} + \{\delta q^e\}^{\mathrm{T}}[K^e]\{q^e\}\right) = 0 \tag{3.50}
$$

where the elementary mass matrix $[M^e]$, the elementary gyroscopic matrix $[G^e(\Omega)]$ and the elementary stiffness matrix $[K^e]$ are given by:

$$
[M^e]_{8\times 8} = \begin{bmatrix}[M_v] & 0 & 0 & 0 \\ 0 & [M_w] & 0 & 0 \\ 0 & 0 & [M_{\theta_y}] & 0 \\ 0 & 0 & 0 & [M_{\theta_z}]\end{bmatrix} \tag{3.51}
$$

$$
[G^e(\Omega)]_{8\times 8} = \begin{bmatrix}0 & 0 & 0 & 0 \\ 0 & 0 & 0 & 0 \\ 0 & 0 & 0 & [G_1(\Omega)] \\ 0 & 0 & -[G_1(\Omega)]^{\mathrm{T}} & 0\end{bmatrix} \tag{3.52}
$$

$$[K^e]_{8\times 8} = \begin{bmatrix} [K_v] & 0 & [K_1] & [K_2] \\ 0 & [K_w] & [K_3] & [K_4] \\ [K_1]^{\mathrm{T}} & [K_3]^{\mathrm{T}} & [K_{\theta_y}] & [K_5] \\ [K_2]^{\mathrm{T}} & [K_4]^{\mathrm{T}} & [K_5]^{\mathrm{T}} & [K_{\theta_z}] \end{bmatrix} \tag{3.53}$$

The elementary mass components, given in equation (3.51), are expressed as follows:

$$\begin{cases} [M_v]_{2\times 2} = \displaystyle\int_{-1}^{1} N_v^{\mathrm{T}} I_m N_v \det(J)\,\mathrm{d}\xi \\ [M_w]_{2\times 2} = \displaystyle\int_{-1}^{1} N_w^{\mathrm{T}} I_m N_w \det(J)\,\mathrm{d}\xi \\ [M_{\theta_y}]_{2\times 2} = \displaystyle\int_{-1}^{1} N_{\theta_y}^{\mathrm{T}} I_d N_{\theta_y} \det(J)\,\mathrm{d}\xi \\ [M_{\theta_z}]_{2\times 2} = \displaystyle\int_{-1}^{1} N_{\theta_z}^{\mathrm{T}} I_d N_{\theta_z} \det(J)\,\mathrm{d}\xi \end{cases} \tag{3.54}$$

The components of the elementary gyroscopic matrix are given as follows:

$$[G_1(\Omega)]_{2\times 2} = \Omega \int_{-1}^{1} N_{\theta_y}^{\mathrm{T}} I_p N_{\theta_z} \det(J)\,\mathrm{d}\xi \tag{3.55}$$

The elementary stiffness terms, given in equation (3.53), are expressed as follows:

$$\begin{cases} [K_v]_{2\times 2} = -\displaystyle\int_{-1}^{1} B_v^{\mathrm{T}} k_s (A_{55} + A_{66}) B_v \det(J)\,\mathrm{d}\xi \\ [K_1]_{2\times 2} = -\dfrac{1}{2}\displaystyle\int_{-1}^{1} B_v^{\mathrm{T}} k_s A_{16} B_{\theta_y} \det(J)\,\mathrm{d}\xi \\ [K_2]_{2\times 2} = \displaystyle\int_{-1}^{1} B_v^{\mathrm{T}} k_s (A_{55} + A_{66}) N_{\theta_z} \det(J)\,\mathrm{d}\xi \\ [K_w]_{2\times 2} = \displaystyle\int_{-1}^{1} B_w^{\mathrm{T}} k_s (A_{55} + A_{66}) B_w \det(J)\,\mathrm{d}\xi \\ [K_3]_{2\times 2} = \displaystyle\int_{-1}^{1} B_w^{\mathrm{T}} k_s (A_{55} + A_{66}) N_{\theta_y} \det(J)\,\mathrm{d}\xi \\ [K_4]_{2\times 2} = -\dfrac{1}{2}\displaystyle\int_{-1}^{1} B_w^{\mathrm{T}} k_s A_{16} B_{\theta_z} \det(J)\,\mathrm{d}\xi \\ [K_{\theta_y}]_{2\times 2} = \displaystyle\int_{-1}^{1} B_{\theta_y}^{\mathrm{T}} A_{11} B_{\theta_y} \det(J)\,\mathrm{d}\xi + \int_{-1}^{1} N_{\theta_y}^{\mathrm{T}} k_s (A_{55} + A_{66}) N_{\theta_y} \det(J)\,\mathrm{d}\xi \\ [K_5]_{2\times 2} = \dfrac{1}{2}\displaystyle\int_{-1}^{1} B_{\theta_y}^{\mathrm{T}} k_s A_{16} N_{\theta_z} \det(J)\,\mathrm{d}\xi - \dfrac{1}{2}\int_{-1}^{1} B_{\theta_z}^{\mathrm{T}} k_s A_{16} N_{\theta_y} \det(J)\,\mathrm{d}\xi \\ [K_{\theta_z}]_{2\times 2} = \displaystyle\int_{-1}^{1} B_{\theta_z}^{\mathrm{T}} A_{11} B_{\theta_z} \det(J)\,\mathrm{d}\xi + \int_{-1}^{1} N_{\theta_z}^{\mathrm{T}} k_s (A_{55} + A_{66}) N_{\theta_z} \det(J)\,\mathrm{d}\xi \end{cases} \tag{3.56}$$

The elementary mass, gyroscopic and stiffness matrices are thus obtained as the sum of the contribution of each orthotropic layer through the terms defined in equations (3.26) and (3.32).

3.4 Equation of motion

The introduction of the connectivity (3.49) in equation (3.50) yields:

$$\{\delta q\}^{\mathrm{T}}[M]\{\ddot{q}\} + \{\delta q\}^{\mathrm{T}}[G(\Omega)]\{\dot{q}\} + \{\delta q\}^{\mathrm{T}}[K]\{q\} = \{0\} \qquad \forall \{\delta q\} \tag{3.57}$$

where the assembled global mass $[M]$, gyroscopic $[G(\Omega)]$ and stiffness $[K]$ matrices are defined by:

$$\begin{cases} [M] = \sum_{e=1}^{E} [R^e]^{\mathrm{T}} [M^e] [R^e] \\ [G(\Omega)] = \sum_{e=1}^{E} [R^e]^{\mathrm{T}} [G^e(\Omega)] [R^e] \\ [K] = \sum_{e=1}^{E} [R^e]^{\mathrm{T}} [K^e] [R^e] \end{cases} \tag{3.58}$$

The global semi-discrete equations of motion of the rotating composite shaft are given by the non trivial solution of equation (3.57), yielding:

$$[M]\{\ddot{q}\} + [G(\Omega)]\{\dot{q}\} + [K]\{q\} = \{0\} \tag{3.59}$$

where $[M]$ is the symmetric mass matrix, $[G(\Omega)]$ is the skew-symmetric gyroscopic matrix which depends on the rotational speed Ω and $[K]$ is the stiffness matrix. The stiffness matrix $[K]$ may be symmetric or non-symmetric in the case of non-symmetric bearings stiffness. $\{\ddot{q}\}$, $\{\dot{q}\}$ and $\{q\}$ are respectively nodal acceleration, velocity and displacement vectors.

3.5 Modal analysis

Considering the case of free vibration, the equation of motion of undamped gyroscopic system is given by:

$$[M]\{\ddot{q}\} + [G(\Omega)]\{\dot{q}\} + [K]\{q\} = \{0\} \tag{3.60}$$

The equation of motion for free vibration of undamped gyroscopic system, given in equation (3.60), is a $2nd$ order differential equation. Since we are also considering the gyroscopic effect, therefore we have to treat the system of equations with three matrices which leads to a quadratic eigenvalue problem. To solve the associated problem by using standard algorithms, we will therefore re-write equation (3.60) in the first order form.

Equation (3.60) can be written as:

$$[M]\{\ddot{q}\} = -[G(\Omega)]\{\dot{q}\} - [K]\{q\} \tag{3.61}$$

and it can be associated the identity equation as:

$$[M]\{\dot{q}\} = [M]\{\dot{q}\} \tag{3.62}$$

The above two equations can be re-written as a single set of equations as:

$$\begin{bmatrix} [M] & [0] \\ [0] & [M] \end{bmatrix} \begin{Bmatrix} \dot{q} \\ \ddot{q} \end{Bmatrix} = \begin{bmatrix} [0] & [M] \\ -[K] & -[G(\Omega)] \end{bmatrix} \begin{Bmatrix} q \\ \dot{q} \end{Bmatrix} \tag{3.63}$$

Denoting the state-space vector $\{x\}$ as:

$$\{x\} = \begin{Bmatrix} q \\ \dot{q} \end{Bmatrix} \tag{3.64}$$

Substituting the $2n$ state-space vector $\{x\}$, defined in equation (3.64), in equation (3.63), the dynamic equilibrium equation (3.60) can be written in the first order form as:

$$[A]\{\dot{x}\} + [B(\Omega)]\{x\} = \{0\} \tag{3.65}$$

which is the state-space form of the equation of motion of the undamped gyroscopic system where the $2n \times 2n$ matrix $[A]$ is a real symmetric positive definite matrix and the $2n \times 2n$ matrix $[B(\Omega)]$ is a real non-symmetric matrix which depends on the rotational speed Ω, defined as:

$$[A] = \begin{bmatrix} [M] & [0] \\ [0] & [M] \end{bmatrix} \qquad \text{and} \qquad [B(\Omega)] = \begin{bmatrix} [0] & -[M] \\ [K] & [G(\Omega)] \end{bmatrix} \tag{3.66}$$

The solution of equation (3.65) can be assumed as:

$$\{x\} = \{X\}\, \mathrm{e}^{\lambda t} \tag{3.67}$$

where $\{X\}$ is a magnitude vector and λ is the inverse of a time constant. They are written as:

$$\{X\} = \{\{\psi\}, \lambda\{\psi\}\}^{\mathrm{T}} \quad \text{and} \quad \lambda = \mathrm{j}\omega \tag{3.68}$$

with ψ are the eigenvectors and ω are the eigenfrequencies. $\{X\}$ and λ are solutions of the equation:

$$\big([B(\Omega)] + \lambda[A]\big)\{X\} = \{0\} \tag{3.69}$$

The system therefore allows $2n$ eigenvectors $\{X_r\}$ associated with the eigenvalues λ_r which are the roots of the characteristic equation:

$$\det\big([B(\Omega)] + \lambda[A]\big) = 0 \tag{3.70}$$

3.6 Frequency Response Function - FRF

The equation of motion of forced vibration of undamped gyroscopic system is given as:

$$[M]\{\ddot{q}(t)\} + [G(\Omega)]\{\dot{q}(t)\} + [K]\{q(t)\} = \{f(t)\} \tag{3.71}$$

Considering the steady state excitation as:

$$f(t) = \bar{F}(\mathrm{j}\omega)\, \mathrm{e}^{\mathrm{j}\omega t} \tag{3.72}$$

The steady state response is given by:

$$q(t) = \bar{Q}(\mathrm{j}\omega)\, \mathrm{e}^{\mathrm{j}\omega t} \tag{3.73}$$

where $\mathrm{j} = \sqrt{-1}$, ω is the forcing frequency, $\bar{Q}(\mathrm{j}\omega)$ is the complex vector (displacements phaser) and $\bar{F}$ is the amplitude vector of the applied mechanical forces.

Substituting equations (3.73) and (3.72) into equation (3.71) yields:

$$\left(K + \mathrm{j}\omega G\left(\Omega\right) - \omega^2 M\right)\bar{Q}\left(\mathrm{j}\omega\right) = \bar{F} \tag{3.74}$$

For an excitation applied at the ith degree of freedom (*dof*) and a displacement measured in the oth *dof*, the frequency response function (FRF) can be obtained by solving equation (3.74) for different values of frequency:

$$\left(K + \mathrm{j}\omega_l G\left(\Omega\right) - \omega_l^2 M\right)\bar{Q}\left(\mathrm{j}\omega_l\right) = \bar{F}_i \tag{3.75}$$

where $\bar{F}_i$ denotes a force vector with a non-zero component in the ith *dof* and all other elements equal to zero and $\bar{Q}\left(\mathrm{j}\omega_l\right)$ is the resulting complex response vector (displacements) solution at frequency ω_l. Thus, the receptance FRF at frequency ω_l is given by:

$$\alpha_{oi}\left(\mathrm{j}\omega_l\right) = \frac{\bar{q}_o\left(\mathrm{j}\omega_l\right)}{\bar{f}_i} \tag{3.76}$$

where $\bar{f}_i$ is the amplitude of the input force and $\bar{q}_o\left(\mathrm{j}\omega_l\right)$ is the displacement response phaser extracted from the oth *dof* of the vector $\bar{Q}\left(\mathrm{j}\omega_l\right)$. In fact, the frequency response model can be generated from the results of many discrete frequency calculations of equation (3.75), in which the rotational speed Ω is fixed as explained in figure 3.12.

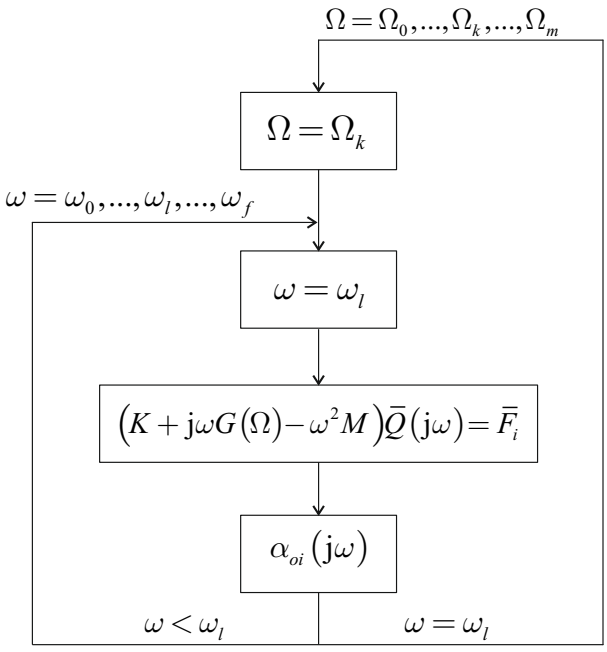

Figure 3.12. Response model generation diagram

The system response can also be velocity or acceleration [Ewins, 1984]. Replacing the displacement response $\bar{Q}\left(\mathrm{j}\omega\right)$ with velocity $\mathrm{j}\omega\bar{Q}\left(\mathrm{j}\omega\right)$ and acceleration $-\omega^2\bar{Q}\left(\mathrm{j}\omega\right)$, two new types of FRF's can be defined in following.

The mobility FRF is given by:

$$Y_{oi}\left(\mathrm{j}\omega_l\right) = \mathrm{j}\omega\frac{\bar{q}_o\left(\mathrm{j}\omega_l\right)}{\bar{f}_i} \tag{3.77}$$

which, taken into account equation (3.76), may also be written as:

$$Y_{oi}\left(\mathrm{j}\omega_l\right) = \mathrm{j}\omega\alpha_{oi}\left(\mathrm{j}\omega_l\right) \tag{3.78}$$

The accelerance FRF is given by:

$$A_{oi}\left(\mathrm{j}\omega_l\right) = -\omega^2 \frac{\bar{q}_o\left(\mathrm{j}\omega_l\right)}{\bar{f}_i} \tag{3.79}$$

which, taken into account equation (3.76), may also be written as:

$$A_{oi}\left(\mathrm{j}\omega_l\right) = -\omega^2\alpha_{oi}\left(\mathrm{j}\omega_l\right) \tag{3.80}$$

3.7 Results and discussion

Based on the developed ESLT, the established finite element model was implemented in a Matlab code and validated with results available in the literature. Different analysis have been carried out. The study of the influence of several parameters such as the physical and geometric parameters, stacking sequence, fiber orientation, boundary conditions and nature of the composite materials on the dynamic behaviour of the rotating composite shaft is presented in the following sections.

3.7.1 Validation of Equivalent Single Layer Theory formulation

The model is developed to avoid the main drawbacks associated with EMBT. The objective is to estimate the extent of difference in results obtained using ESLT by varying the stacking sequence of a simply supported composite shaft made of carbon/epoxy of typical dimensions and parameters given below. The material properties of each carbon/epoxy layer are given in table 3.1. Results from the present work using ESLT are compared with those obtained using EMBT proposed by [Singh and Gupta, 1996b] as shown in table 3.2.

- $L = 1$ m, mean radius $= R_m = 0.05$ m, wall thickness $= h = 4$ mm;
- Shear correction factor: $k_s = 1/2$ [Freund and Karakoc, 2016; Gubran and Gupta, 2005].

Table 3.1. Carbon/epoxy shaft material properties

Material	E_1 (GPa)	E_2 (GPa)	G_{ij} (GPa)	ν_{12}	ρ (kg/m^3)
Carbon/epoxy	130	10	7	0.25	1500

In this study, the stacking sequence consists of four layers: three layers with fibers oriented at 45° and one layer with fibers oriented at 0°. The position of the layer with 0° fiber orientation varies from the inner to the outer radius and the associated changes of the bending natural frequencies are given in table 3.2.

Table 3.2. Variation of the bending natural frequencies (Hz) with stacking sequences using ESLT

Stacking sequences	1st bending	2nd bending	3rd bending
$[0, 45, 45, 45]$	322	1148	2242
$[45, 0, 45, 45]$	326	1159	2258
$[45, 45, 0, 45]$	329	1170	2275
$[45, 45, 45, 0]$	333	1181	2292
EMBT [Singh and Gupta, 1996b]	314	1166	2376

The variation of the bending natural frequencies can be explained as under. The layer with 0° fiber orientation angle has longitudinal modulus longer than the layer with 45° fiber orientation angle. Consequently, the position of the layer with 0° fiber orientation angle largely governs the bending deformation energy of the shaft. It can be noticed that when the layer fiber orientation angle of the outer radius changes from 0° to 45°, the bending frequencies decrease, primarily due to decrease in the longitudinal modulus. When the layer with 0° fiber orientation angle occupies the outer radius, the shaft becomes more stiffer which explains the highest bending frequencies obtained for $[45, 45, 45, 0]$ stacking sequence.

Let consider now the rotor test proposed by [Sino et al., 2008] which is a composite shaft with two rigid steel discs supported by two bearings at the ends as shown in figure 3.13. The fundamental bending natural frequencies of the rotor test with different stacking sequences in both symmetric and non-symmetric configurations with 8 layers of equal thickness is analysed.

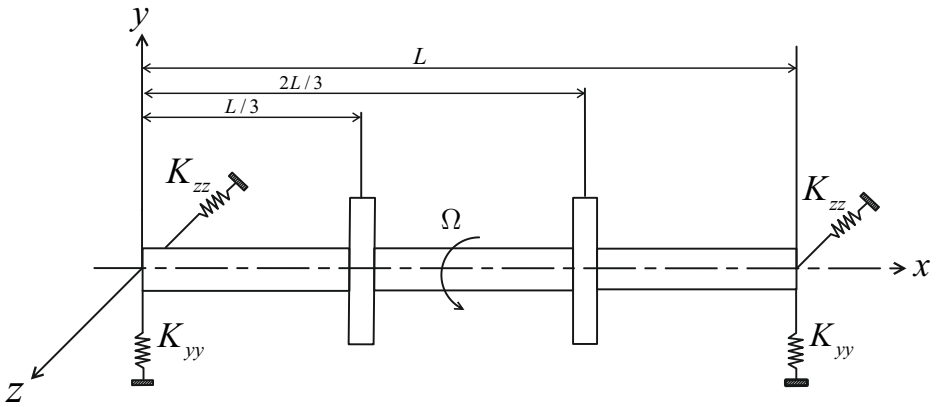

Figure 3.13. Shaft with two rigid discs supported by two bearings

This rotor system presents the following geometric and material properties:

- Carbon/epoxy shaft: $L = 1.2$ m, outer radius $= R_o = 0.048$ m, wall thickness $= h = 0.008$ m, $E_1 = 172.7$ GPa, $E_2 = 7.2$ GPa, $G_{ij} = 3.76$ GPa, $\nu_{12} = 0.3$, $\rho = 1446.2$ kg/m^3;
- Shear correction factor: $k_s = 1/2$;
- Steel disk: inner radius $= R_{Di} = 0.048$ m, outer radius $= R_{Di} = 0.15$ m, thickness $= h_D = 0.05$ m, $\rho_D = 7800$ kg/m^3;

- Anisotropic bearings: $K_{yy} = 1 \times 10^8$ N/m, $K_{zz} = 1 \times 10^7$ N/m, $K_{yz} = K_{zy} = 0$ N/m.

Results obtained using ESLT are compared with those obtained using SHBT developed by [Sino et al., 2008] as shown in table 3.3.

Table 3.3. Effect of stacking sequence on the fundamental bending natural frequency ω_1 (Hz)

Stacking Sequence	SHBT [Sino et al., 2008]	**ESLT**
1: $[\pm 75]_{8S}$	16.88	17.54
2: $[90_2, 45, 0]_S$	39.87	40.62
3: $[90, 0, 90, 45, 90, 45, 0, 90]$	40.08	40.79
4: $[90, 45, 0_2]_S$	50.71	49.37
5: $[0_2, 45_2, 90_2, 0_2]$	50.91	49.42
6: $[0_2, 90, 45]_S$	50.92	49.53
7: $[45, 0, 45, 0, 90, 0, 90, 0]$	51.36	49.64

Results associated with different stacking sequences and different fiber orientations, listed in table 3.3, and obtained using ESLT are close to those obtained using SHBT proposed by [Sino et al., 2008]. The first stacking sequence is in balanced and symmetric configuration. Thus, the shear-normal coupling is present. In fact, ESLT takes account of the shear-normal coupling effects, while SHBT does not consider any mechanical coupling effects. Therefore, results from this work are slightly different from those obtained using SHBT for the first stacking sequence. Stacking sequences 2 and 3 have four layers with fibers oriented at $90°$, two layers with fibers oriented at $45°$ and two with fibers oriented at $0°$, while stacking sequences 4-7 consist of four layers with fibers oriented at $0°$, two layers with fibers oriented at $45°$ and two with fibers oriented at $90°$. Variation of 18% for the first bending natural frequency is obtained when comparing stacking sequences 2 to 6. The contribution of each orthotropic layer depends on its orientation with respect to the shaft axis and its distance from the longitudinal shaft axis. Obtained results revealed that fiber orientations and stacking sequences of the composite shaft have a great influence on the fundamental natural frequency of the rotating rotor.

3.7.2 Unbalance response

A rotor system proposed by [Lalanne and Ferraris, 1990], which is a steel shaft with three rigid steel discs supported by two bearing as shown in figure 3.14, is considered.

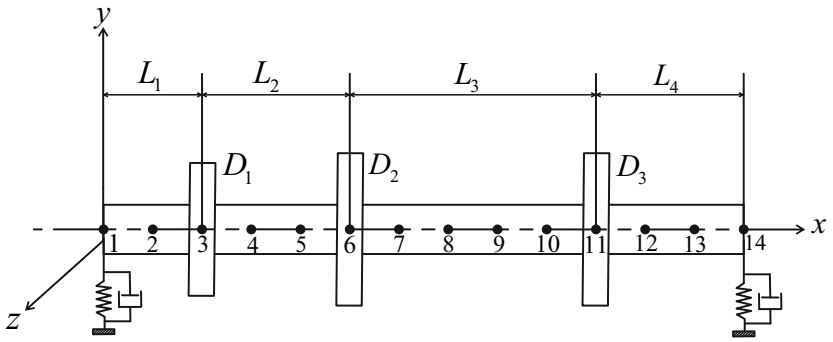

Figure 3.14. Rotor system

The two bearings are assumed identical and defined as: K_{yy} = 7×10^7 N/m, K_{zz} = 5×10^7 N/m, K_{yz} = K_{zy} = 0 and C_{yy} = 7×10^2 N/m, C_{zz} = 5×10^2 N/m, C_{yz} = C_{zy} = 0. A mass unbalance of 200 g mm is assumed to be situated on the disk D_2. The steel discs geometric data are given in table 3.4 and the steel shaft geometric and material properties are given as follows:

- $L_1 = 0.2$ m, $L_2 = 0.3$ m, $L_3 = 0.5$ m, $L_4 = 0.3$ m, radius = $R = 0.05$ m;
- Steel: $E = 2 \times 10^{11}$ Pa, $\nu = 0.3$, $\rho = 7800$ kg/m^3;
- The shaft uses 13 finite elements of equal length.

Table 3.4. Discs geometric data (m)

Disk	Inner radius	Outer radius	Thickness
D_1	0.05	0.12	0.05
D_2	0.05	0.2	0.05
D_3	0.05	0.2	0.06

Results for the displacement at the node 6 for both cases without and with mass unbalance are shown in figure 3.15. It can be observed that the displacement amplitude increases in case with mass unbalance.

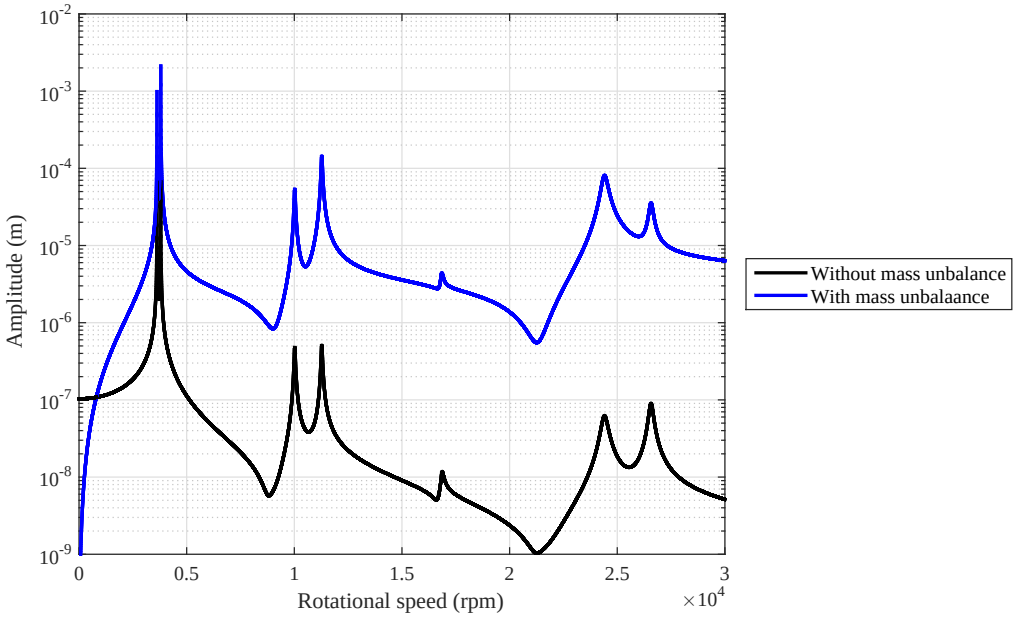

Figure 3.15. Mass unbalance response

In the case with mass unbalance, critical speeds, amplitude of the response at node 6 and accuracy percentage of the amplitude, obtained from this work, are given in table 3.5. Obtained results are compared with those obtained by [Lalanne and Ferraris, 1990] as shown in table 3.5.

Table 3.5. Critical speed (rpm), amplitude of the response (m) and accuracy percentage of the amplitude

	[Lalanne and Ferraris, 1990, p.74]	Present work
1st peak	3620.5 0.938×10^{-3}	3621 0.9856×10^{-3} 4.8%
2nd peak	3798.3 0.210×10^{-2}	3798 0.2116×10^{-2} 0.7%
3rd peak	10018 0.499×10^{-4}	10020 0.5331×10^{-4} 6.4%
4th peak	11281 0.130×10^{-3}	11280 0.1428×10^{-3} 9%
5th peak	16787 0.421×10^{-5}	16860 0.4361×10^{-5} 3.5%
6th peak	24418 0.684×10^{-4}	24410 0.8009×10^{-4} 14.6%
7th peak	26611 0.311×10^{-4}	26570 0.3524×10^{-4} 11.7%

Obtained critical speeds are satisfactory when comparing with those obtained by [Lalanne and Ferraris, 1990]. A variation between 0.7% and 9% is obtained when comparing the amplitude of the receptance from the 1st peak to the 5th peak, while variation between 11.7% and 14.6% is obtained when comparing the 6th peak to the 7th peak.

In the above example, an isotropic configuration is assumed, while now a hybrid configuration is taken into account. Let consider a simply supported shaft with one rigid steel disk at $L/3$ position (see figure 3.13). A mass unbalance of 10^{-4} kg positioned at 0.15 m from the center of the disk is considered. In this case, the length of the shaft is $L = 1.3$ m and the outer diameter is $D_o = 50$ mm. Four different configurations of the shaft are analysed such as: aluminium shaft, composite shaft and two hybrid configurations like: [aluminium,composite] and [composite,aluminium] shafts. The composite shaft consists of four layers made of carbon/epoxy. The carbon/epoxy material properties are defined in table 3.1. The stacking sequence considered in this case is $[0, 90, 90, 0]$. The aluminium material properties are defined as: $E = 66 \times 10^9$ Pa, $\nu = 0.33$ and $\rho = 2680$ kg/m^3. Figure 3.16 shows the

unbalance response of point receptance type for the different configurations. In fact, the response is considered on the associated node.

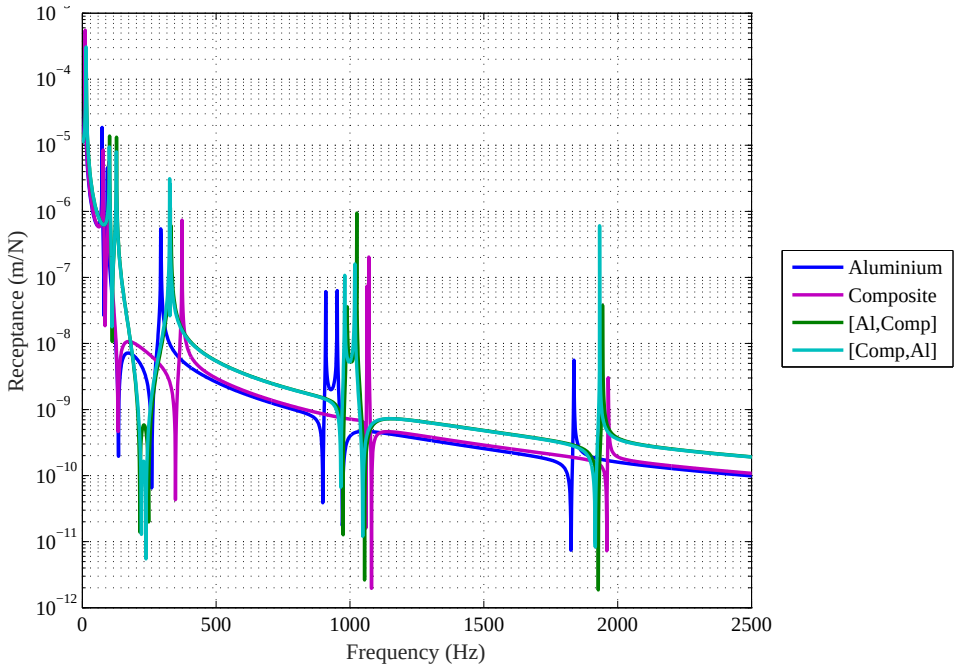

Figure 3.16. Unbalance response for different configurations

It can be observed from figure 3.16 that for low frequencies below 200Hz, natural frequencies of both configurations [Al,Comp] and [Comp,Al] are higher than those of aluminium and composite configurations, while for frequencies higher than 200Hz, natural frequencies of both hybrid configurations are between that of composite configuration and aluminium configuration. It can be noted that both hybrid configurations have a slight difference in the natural frequencies. It can be observed also that as the frequency increases, as the receptance amplitude of the different configurations decreases. The receptance amplitude of [Al,Comp] and [Comp,Al] depends on the frequency in which the rotor is performing.

3.7.3 Gyroscopic effect

In order to analyse the gyroscopic effect on the dynamic behaviour of the structure, a simply supported rotor with two rigid steel discs of the same geometric and material parameters as the rotor test (section 3.7.1) is analysed. The stacking sequence considered is $[90, 0, 90, 45, 90, 45, 0, 90]$.

A modal analysis is performed to illustrate the effects of changing rotor speeds from a non-rotating to a high rotational speed and to follow the frequencies associated with the bending modes. Figure 3.17 shows the forward and backward natural frequencies over a wide speed range. From this figure, it can be observed that frequencies of the first bending modes do change over the rotational speed range. In fact, the backward mode (BW) decreases in frequency, while the forward mode (FW) increases. The explanation for this behaviour is the 'gyroscopic effect'. First consider the forward whirl. As the shaft speed increases, the gyroscopic effects essentially act like an increasingly stiff spring on the motion of the

rotating shaft. Increasing stiffness acts to increase the natural frequency. For backward whirl, the effect is reversed. Increasing rotor spin speed acts to reduce the effective stiffness, thus reducing the natural frequency.

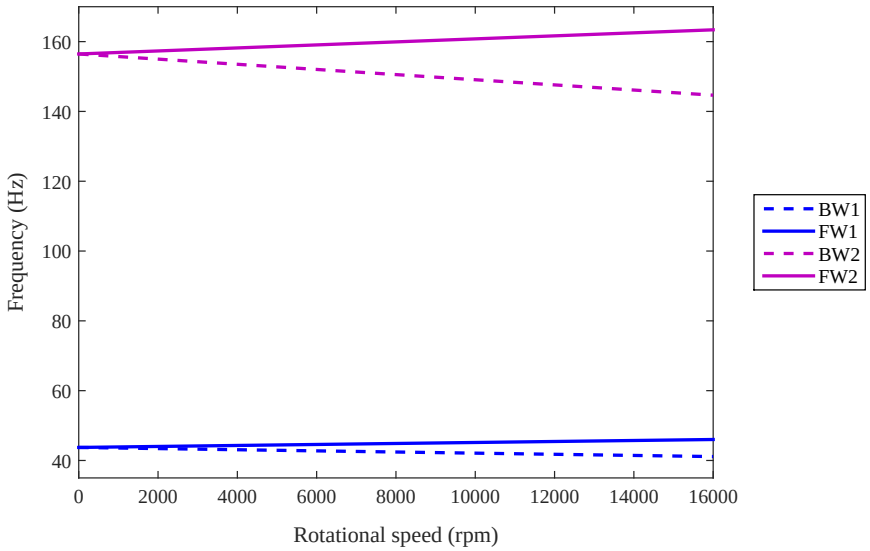

Figure 3.17. Campbell diagram for bending modes of the rotating structure

3.7.4 Boundary conditions effect

Let consider the same geometric and material properties of the structure presented in section 3.7.3 with different boundary conditions. Figure 3.18 shows the variation of the first bending frequencies in terms of the rotational speed with different boundary conditions. The gyroscopic coupling of the rotating structures induces a forward or backward movement according to the direction of rotating movement of the rotor. In the case of forward, this movement is in the same direction with the rotor rotation and in the case of backward, this movement is in the opposite direction with the rotor rotation.

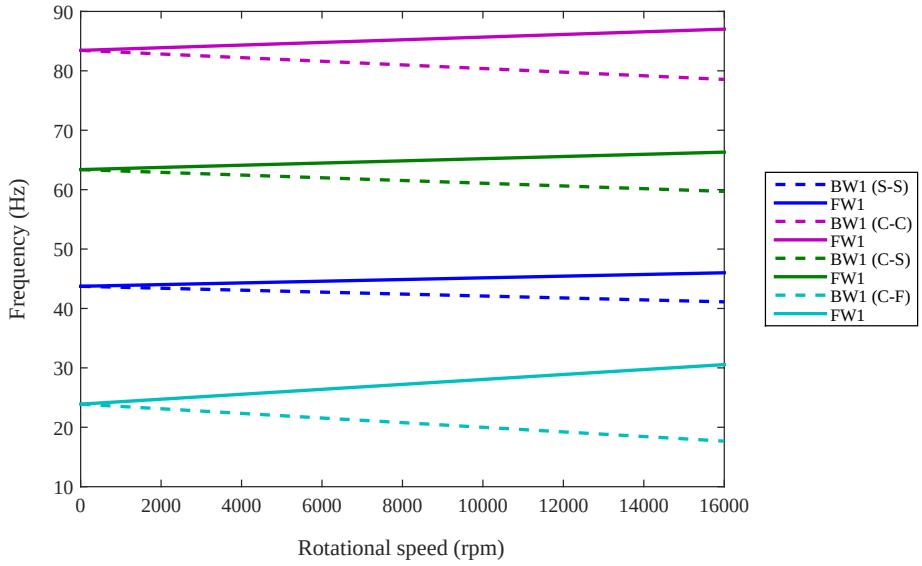

Figure 3.18. First pairs of the bending mode for different boundary conditions

It can be observed from figure 3.18 that the higher bending frequencies are for the clamped structure (C-C) and the lowest one are for the structure which is clamped at one extremity and free at the other extremity (C-F).

3.7.5 Fiber orientation effect

In order to show the effects of fiber orientations on natural frequencies, a rotor of the same geometric and material properties as the rotor test (section 3.7.1) simply supported and without discs is analysed. The considered shaft is made of isotropic or orthotropic material. The stacking sequence of composite material consists of one single layer $[\alpha]$. Figure 3.19 shows the Campbell diagram of the first pairs of the bending mode for the composite shaft and for the steel and aluminium shafts.

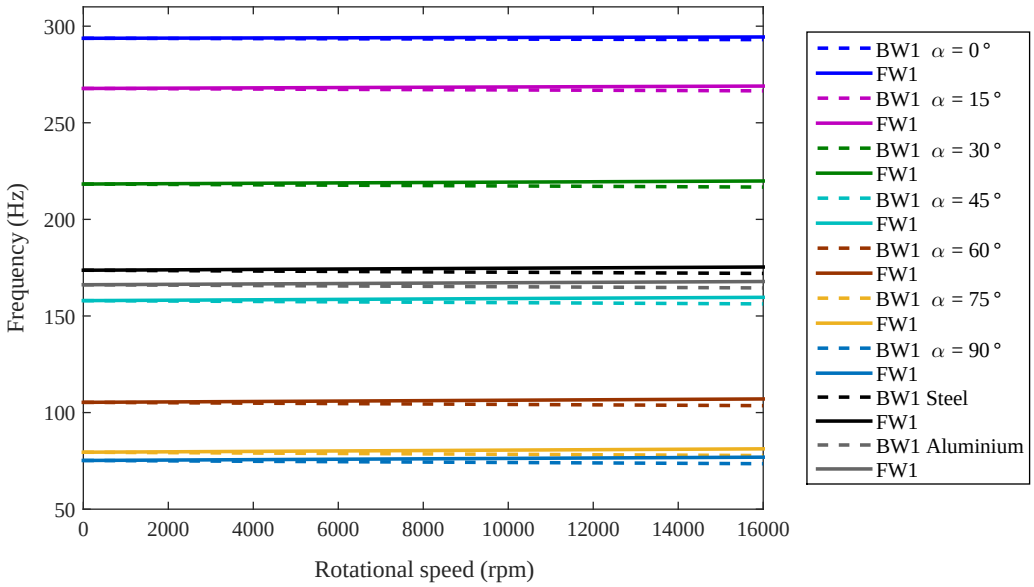

Figure 3.19. First pairs of the bending mode for different fiber orientations

It can be noted from figure 3.19 that, for $75°$ and $90°$ fiber orientation angles, the bending natural frequencies of the rotating composite shaft are very similar and have the lowest bending frequencies, while for $0°$ fiber angle, the bending natural frequencies are the highest. Figure 3.19 shows also the first pairs of the bending mode of a rotating steel shaft ($E = 210$ GPa, $\nu = 0.36$ and $\rho = 7800$ kg/m^3) and aluminium shaft ($E = 66$ GPa, $\nu = 0.33$ and $\rho = 2680$ kg/m^3). The first pairs of the bending mode of the rotating steel shaft and aluminium shaft are close to those of the rotating composite shaft where the layer fiber orientation angle is $45°$.

It can be observed also from figures 3.19 and 3.20 that bending frequencies of composite shaft decrease as the fiber orientations increase, because the equivalent stiffness of the shaft decreases when the fiber orientation increases. So, to increase the bending natural frequencies of a particular configuration, one or more layers with fibers oriented at $0°$ can be added at the outer radius, thus stiffening the composite shaft.

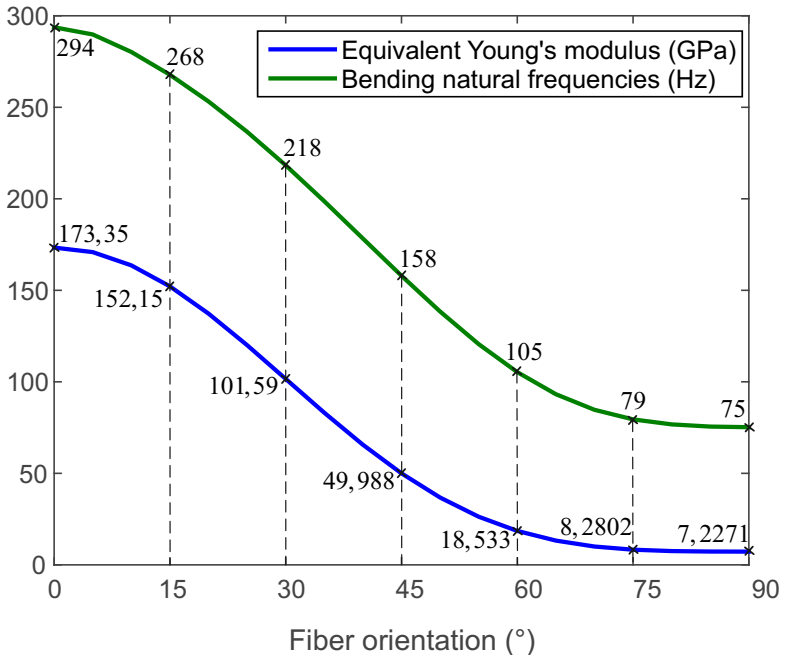

Figure 3.20. Equivalent Young's modulus and first bending natural frequencies for different fiber orientations

Figure 3.21 shows the Campbell diagram of the first twisting mode for the composite shaft made of one single layer $[\alpha]$. It can be observed from figure 3.21 that gyroscopic coupling does not affect the twisting mode. The highest frequencies are those of the layer with fibers oriented at $45°$ and the lowest one are those for the layers with fibers oriented at $0°$ and $90°$. This behaviour can be explained using figure 3.22.

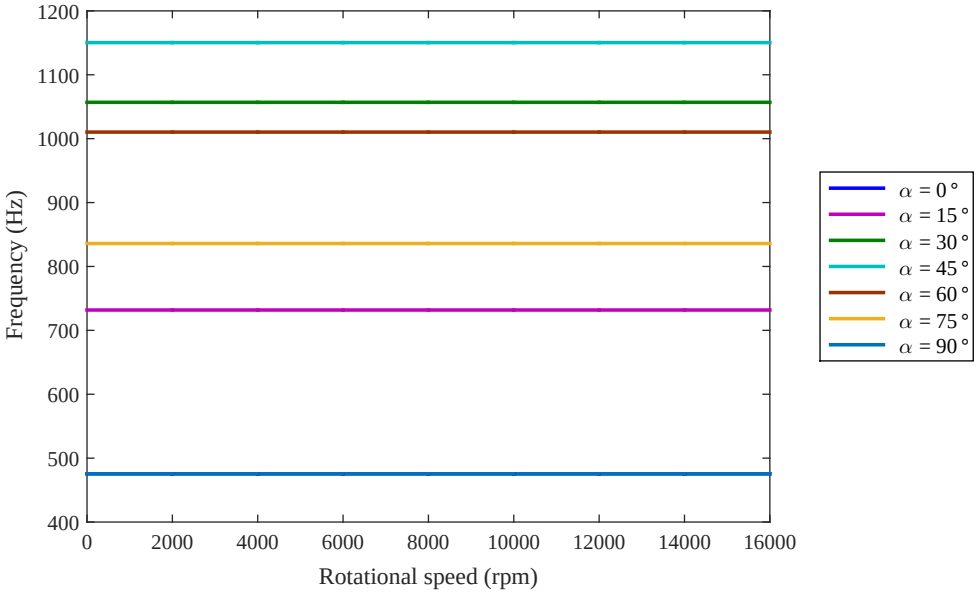

Figure 3.21. First twisting mode for different fiber orientations

Figure 3.22 shows the variation of the equivalent twisting modulus $\bar{Q}_{66}$ with fiber orientations. It can be observed that the highest equivalent twisting modulus corresponds to the layer with fibers oriented at $45°$ and the lowest one corresponds to the layers with fibers oriented at $0°$ and $90°$. In this case, layers with fibers oriented at $30°$ and $60°$, layers with fibers oriented at $15°$ and $75°$ and layers with fibers oriented at $0°$ and $90°$ have equal equivalent twisting modulus.

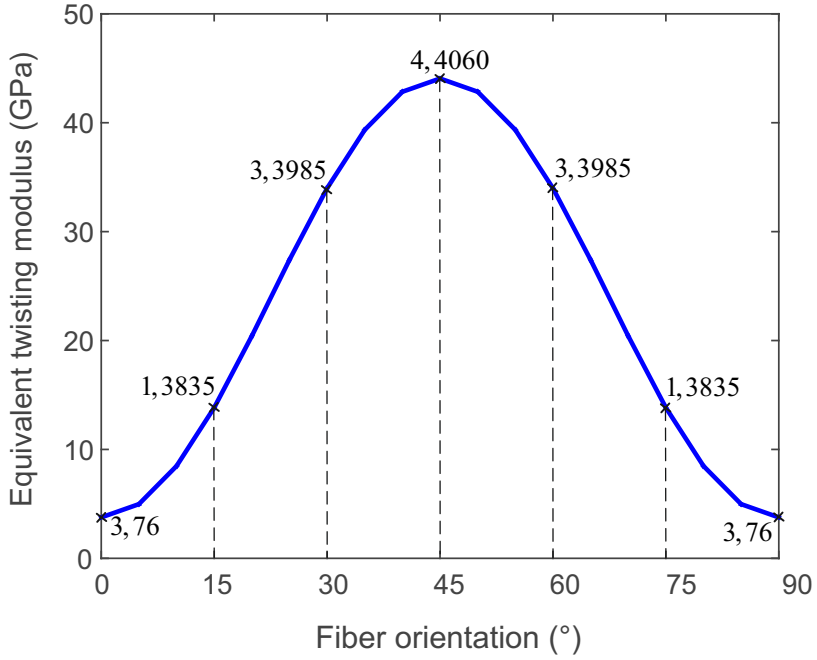

Figure 3.22. Equivalent twisting modulus $\bar{Q}_{66}$ for different fiber orientations

3.7.6 Stacking sequence effect

To analyse the influence of stacking sequences on natural frequencies, a rotor of the same geometric and material parameters as the rotor test (section 3.7.1) simply supported and without discs is considered. In this study, the stacking sequence consists of four layers, two layers with fibers oriented at $90°$ and two layers with fibers oriented at $0°$. Variation of the bending natural frequencies for different stacking sequences (symmetric and non-symmetric) is given in table 3.6.

Table 3.6. Variation of the bending natural frequencies (Hz) with stacking sequences

Configurations	1st Bending	2nd Bending	3rd Bending
$[90, 90, 0, 0]$	245	734	1261
$[0, 0, 90, 90]$	222	695	1221
$[0, 90, 90, 0]$	235	717	1244
$[90, 0, 0, 90]$	234	715	1242
$[0, 90, 0, 90]$	229	706	1233
$[90, 0, 90, 0]$	240	726	1253

Campbell diagram of the first pairs of the bending mode of the rotating shaft for different stacking sequences is shown in figure 3.23. It can be noted that for symmetric stacking sequences, the natural bending frequencies of the rotating composite shaft are very similar and have a slight dependance on fiber orientations of the layer. It can be observed also from figure 3.23 that the highest bending natural frequencies correspond to the stacking sequence where maximum number of layers with fibers oriented at $0°$ occupy the outer radius and that the lowest bending natural frequencies correspond to the stacking sequence where maximum number of layers with fibers oriented at $0°$ occupy the inner radius.

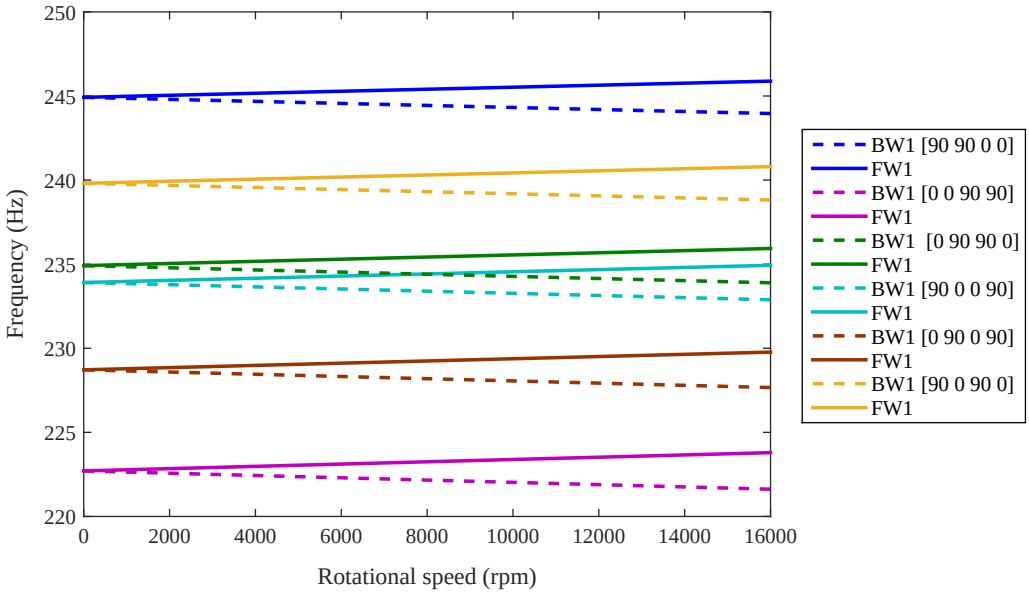

Figure 3.23. First pairs of the bending mode for different staking sequences

The stacking sequence made of four layers, two of them with fibers oriented at $45°$ and two with fibers oriented at $0°$ is now considered. Twisting frequencies of different stacking sequences (symmetric and non-symmetric) is given table 3.7.

Table 3.7. Variation of the twisting frequencies (Hz) with stacking sequence

Configurations	1st Twisting	2nd Twisting	3rd Twisting
$[45, 45, 0, 0]$	1082	2172	3274
$[0, 0, 45, 45]$	1201	2410	3634
$[0, 45, 45, 0]$	1142	2290	3453
$[45, 0, 0, 45]$	1147	2302	3471
$[0, 45, 0, 45]$	1173	2354	3550
$[45, 0, 45, 0]$	1114	2235	3370

Campbell diagram of the first twisting mode of the rotating shaft for different stacking schemes is shown in figure 3.24. It can be noted that for symmetric stacking sequences, the twisting natural frequencies of the rotating composite shaft are very similar and have a slight dependance on fiber orientations of the layer. It can be observed also from figure 3.24 that the highest twisting natural

frequencies correspond to the stacking sequence where maximum number of layers with fibers oriented at $45°$ occupy the outer radius and that the lowest twisting natural frequencies correspond to the stacking sequence where maximum number of layers with fibers oriented at $45°$ occupy the inner radius.

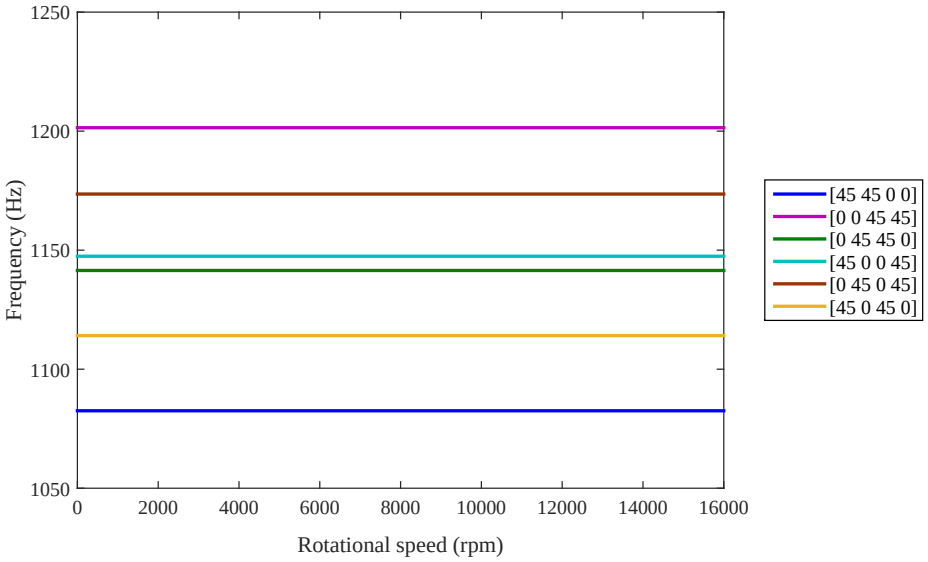

Figure 3.24. First twisting mode for different staking sequences

3.7.7 Shear-normal coupling effect

In order to show the influence of the shear-normal coupling on the rotating structure dynamic behaviour, the same geometric and material properties of the rotor test (section 3.7.1) clamped at one extremity and with one rigid steel disk at the free extremity is considered. The stacking sequence of the carbon/epoxy shaft consists of one layer $[\alpha]$. Figure 3.25 shows the variation of the equivalent shear-normal coupling term for different fiber orientations.

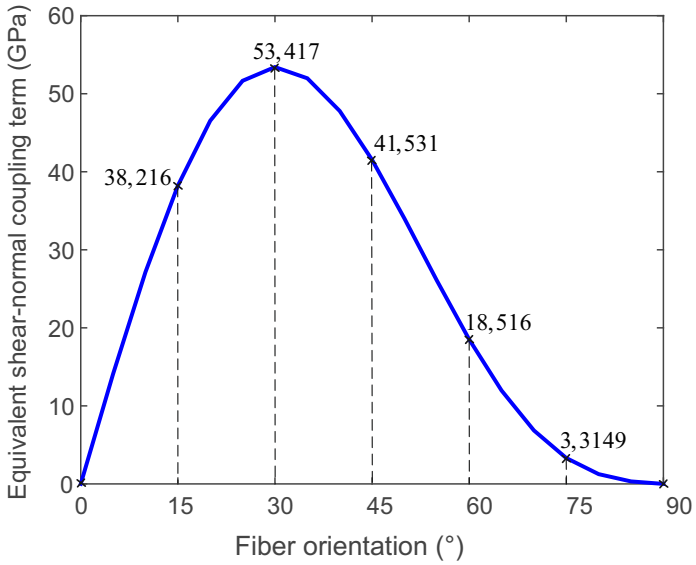

Figure 3.25. Equivalent shear-normal coupling term for different fiber orientations

It can be observed from figure 3.25 that for $0°$ and $90°$ fiber orientation angles, the equivalent shear-normal coupling term is equal to zero. In this case, the shear-normal coupling effect can be neglected. While, for other fiber orientations, the equivalent shear-normal coupling term is different from zero and presents the highest value for $30°$ fiber orientation angle. An important variation is obtained when comparing the different values of the shear-normal coupling term for the different fiber orientations. It can be concluded that shear-normal coupling effect should not be neglected for fiber orientations different from $0°$ and $90°$.

Figure 3.26 shows a comparison between the equivalent Young's modulus and the equivalent shear-normal coupling term for different fiber orientations.

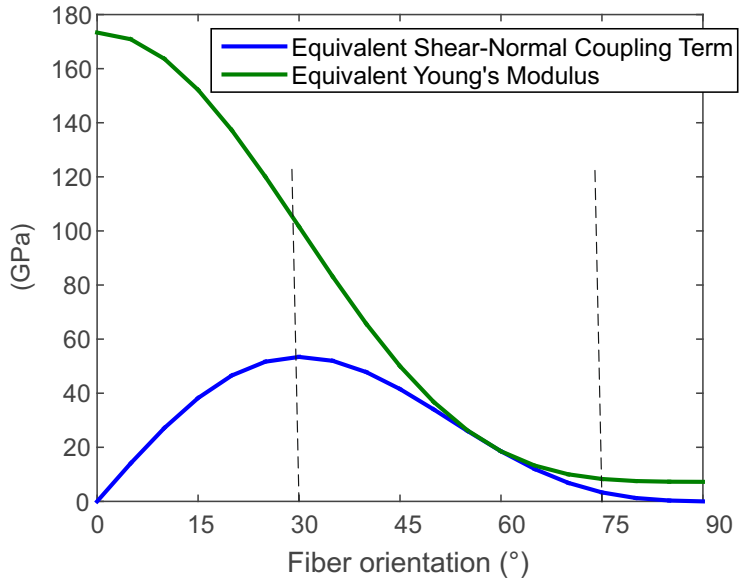

Figure 3.26. Comparison between the equivalent Young's modulus and the equivalent shear-normal coupling term for different fiber orientations

This comparison confirms what was concluded from figure 3.25. In fact, it can be observed from figure 3.26 that, especially for the region where the fiber orientation is between $30°$ and $75°$, the shear-normal coupling effect is more significant. Actually, for $60° \pm 5°$, the equivalent shear-normal coupling term and the equivalent Young's modulus have almost the same values.

3.7.8 Materials properties effect

The same geometric properties as the rotor test (section 3.7.1) simply supported without discs are considered. Here, the composite shaft is made of different composite materials. The chosen stacking sequence is $[90, 0, 90, 45, 90, 45, 0, 90]$. The mechanical properties of different composite materials are defined in table 3.8.

Table 3.8. Mechanical properties of different composite materials

Composite Materials	E_1 (GPa)	E_2 (GPa)	G_{ij} (GPa)	ν_{12}	ρ (kg/m^3)
Carbon/epoxy (C-E)	172.7	7.2	3.76	0.3	1446.2
Boron/epoxy (B-E)	211	24.1	6.9	0.36	1967
Glass/epoxy (G-E)	40	5	4	0.28	1800

Figure 3.27 gives the first pairs of the bending mode of the rotating composite shaft. It can be concluded from figure 3.27 that the bending frequencies depend on the nature of the composite materials. It can be noted that the carbon/epoxy and the boron/epoxy have nearly the same bending natural frequencies which are higher than those of the glass/epoxy.

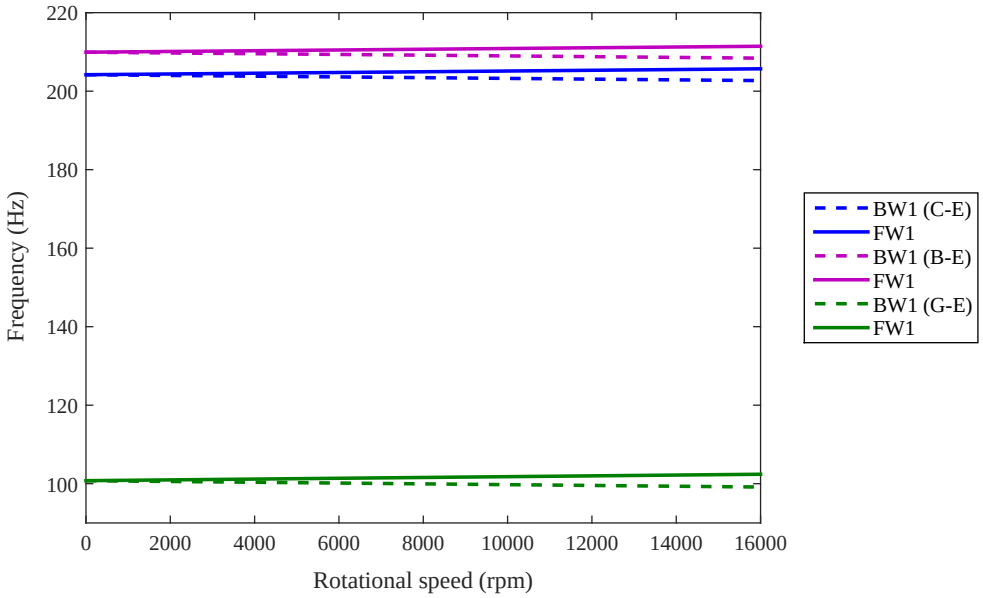

Figure 3.27. First pairs of the bending mode for different composite materials

Considering now the same above example of rotating shaft but with different composite materials for each layer. A different classifications of materials for the 8 layers with equal thicknesses are taken into account as following:

- 1M: [B-E (90°,0°,90°) / G-E (45°,90°,45°) / C-E (0°,90°)]
- 2M: [C-E (90°,0°,90°) / G-E (45°,90°,45°) / B-E (0°,90°)]
- 3M: [G-E (90°,0°,90°) / B-E (45°,90°,45°) / C-E (0°,90°)]

As it can be observed from figure 3.28, for 1M and 2M, the frequencies are nearly similar due to the symmetric materials classification used in the different layers so they have a slight dependance on the stacking sequence of the layers. However, for 3M, the bending frequencies are smaller than those obtained for 1M and 2M.

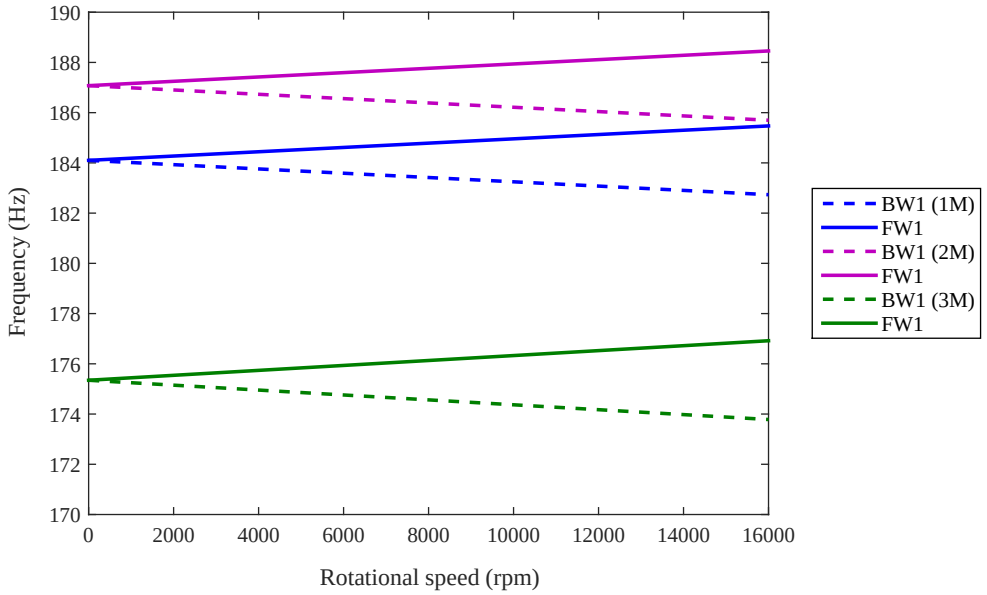

Figure 3.28. First pairs of the bending mode for different composite materials in each layer

Let consider now the case of hybrid configurations where the shaft is made of composite materials and aluminium. The characteristics of the studied hybrid shaft, which are free at both ends, are defined as follows:

- $L_1 = 1.3$ m, outer diameter $= D_o = 0.05$ m;
- Number of composite layers $= 4$, composite layer thickness $= 0.4$ mm;
- Stacking sequence: a combination of 2 layers with 0° fiber orientation angle and 2 layers with 90° fiber orientation angle;
- Aluminium layer thickness $= 1.5$ mm.

The mechanical properties of composite materials and aluminium are defined respectively in tables 3.9 and 3.10.

Table 3.9. Mechanical properties of composite materials

Composite Materials	E_1 (GPa)	E_2 (GPa)	G_{ij} (GPa)	ν_{12}	ρ (kg/m^3)
Boron/epoxy	211	24.1	6.9	0.36	1967
Carbon/epoxy	130	10	7	0.25	1500
Glass/epoxy	40	5	4	0.28	1800

Table 3.10. Mechanical properties of aluminium

Isotropic material	E (GPa)	ν	ρ (kg/m^3)
Aluminium	66	0.33	2680

Tables 3.11, 3.12 and 3.13 give respectively the lowest bending natural frequencies of different composite materials, of aluminium and hybrid configurations.

Table 3.11. Lowest bending natural frequencies (Hz) of different composite materials with different stacking sequences

Configurations	Composite materials	1st	2nd	3rd	4th
$[0, 90, 90, 0]$	Boron/epoxy	271	690	1224	1817
	Carbon/epoxy	242	636	1171	1801
	Glass/epoxy	127	340	644	1021
$[90, 90, 0, 0]$	Boron/epoxy	276	700	1239	1834
	Carbon/epoxy	247	647	1189	1824
	Glass/epoxy	129	346	654	1035

It can be observed from table 3.11 that the nature of composite materials affects the behaviour of the composite shaft. The highest bending natural frequencies are obtained using the boron/epoxy material and the lowest bending frequencies are obtained using the glass/epoxy. It can be observed also that the number and the position of the layer with 0° fiber orientation angle affects the behaviour of the composite shaft. In fact, as higher is the number of layers with 0° fiber orientation angle positioned at the outer radius, higher is the bending natural frequencies.

Table 3.12. Lowest bending natural frequencies (Hz) of aluminium

Isotropic material	1st	2nd	3rd	4th
Aluminium	178	487	942	1533

Table 3.13. Lowest bending natural frequencies (Hz) of hybrid configurations

Configurations	Composite materials	1st	2nd	3rd	4th
$[Al, 0, 90, 90, 0]$	Boron/epoxy	224	600	1134	1795
	Carbon/epoxy	200	543	1039	1668
	Glass/epoxy	151	411	795	1293
$[0, 90, 90, 0, Al]$	Boron/epoxy	216	583	1105	1756
	Carbon/epoxy	198	537	1028	1653
	Glass/epoxy	157	429	828	1343
$[Al, 90, 90, 0, 0]$	Boron/epoxy	226	608	1147	1812
	Carbon/epoxy	203	549	1050	1684
	Glass/epoxy	152	414	800	1299
$[90, 90, 0, 0, Al]$	Boron/epoxy	219	589	1117	1773
	Carbon/epoxy	200	542	1038	1667
	Glass/epoxy	158	431	831	1349

It can be observed from tables 3.11, 3.12 and 3.13 that the use of aluminium material with boron/epoxy and carbon/epoxy decreases the bending natural frequencies of the composite shaft. While, the use of aluminium material with glass/epoxy increases the bending natural frequencies of the glass/epoxy shaft. On the other hand, the use of aluminium material with boron/epoxy and carbon/epoxy increases the bending natural frequencies of the aluminium shaft. While, the use of aluminium material with Glass/epoxy decreases the bending natural frequencies of the aluminium shaft.

3.7.9 Disk position effect

In order to analyse the influence of the disk position x on natural frequencies of the rotating composite shaft, the same geometric and materials parameters as the rotor test (section 3.7.1) simply supported with one rigid steel disk are taken into account. The geometric parameters of the disk are defined in the section 3.7.1. The stacking sequence is $[90, 0, 90, 45, 90, 45, 0, 90]$. Figures 3.29 and 3.30 show respectively the Campbell diagrams of the first and the second pairs of the bending mode of a rotating composite shaft with different disk positions.

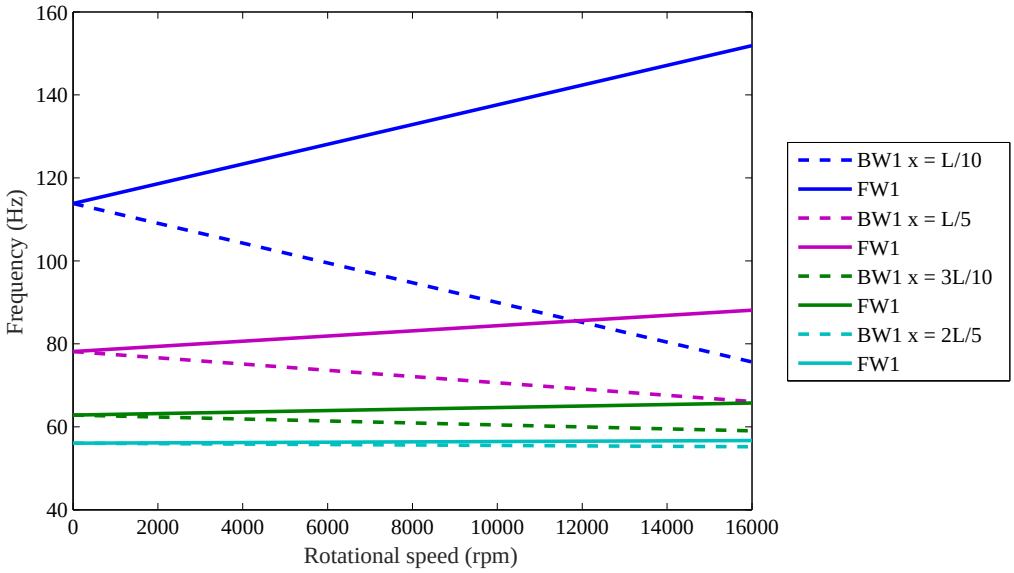

Figure 3.29. First pairs of the bending mode for different disk positions

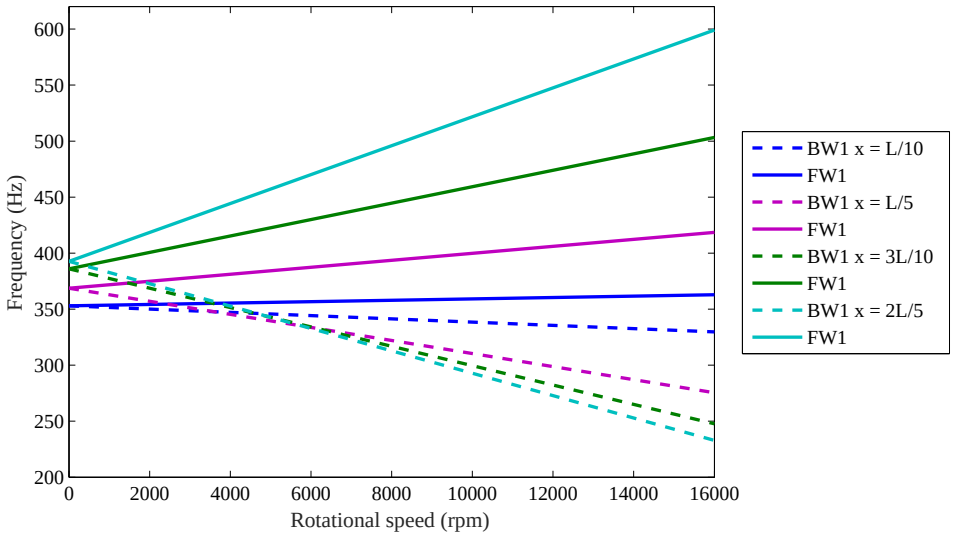

Figure 3.30. Second pairs of the bending mode for different disk positions

It can be noted from figure 3.29 that when the disk approaches to the supports, the first bending natural frequencies and the gyroscopic effect increase. However, using figure 3.30, when the disk approaches to the supports the second bending natural frequencies and the gyroscopic effect decrease. This behaviour is explained by the first symmetric mode shape and the second anti-symmetric mode shape.

3.7.10 Elastic bearings effect

The same material and geometric proprieties as the rotor test (section 3.7.1) without discs and supported by two bearings is considered. Figure 3.31 shows the variation of the first pair of the bending mode of the rotating composite shaft supported on elastic bearings with the rotational speed for different bearings stiffness. In this example, the bearings are isotropic which means that their stiffness are the same in two orthogonal directions as: $K_{yy} = K_{zz} = K_p$ and $K_{yz} = K_{zy} = 0$.

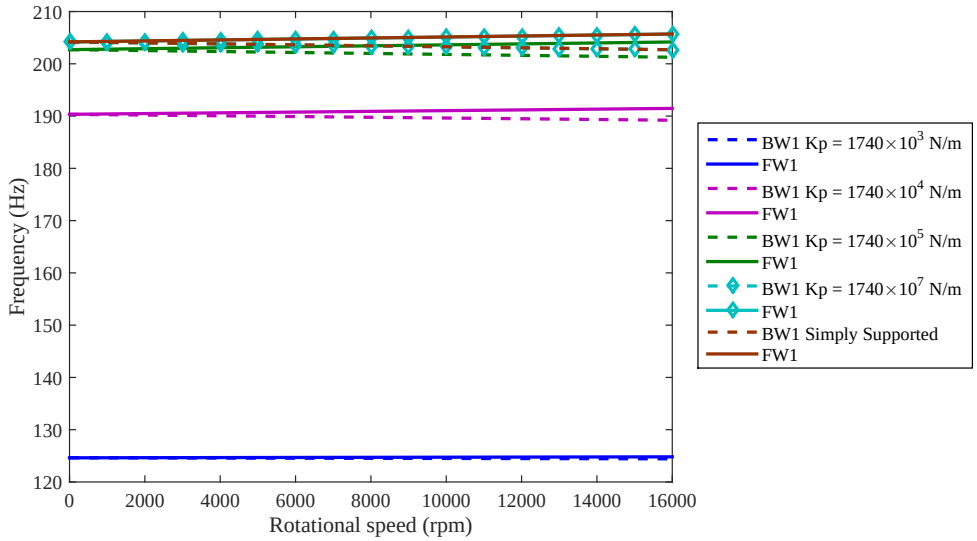

Figure 3.31. First pair of the bending mode for different bearings stiffness

It can be observed from figure 3.31, when the value of K_p increases, the bending natural frequencies increase. When considering the two highest values of K_p, the natural frequencies are very similar and tend to the natural frequencies of a simply supported rotating composite shaft, where K_p tends to the infinity.

The same example is considered with anisotropic bearings which means that their stiffness is different in two orthogonal directions to the rotation axis. In this case, the rotor is asymmetric. The mechanical characteristics of the two bearings are: $K_{yy} = 1.74 \times 10^{12}$ N/m, $K_{zz} = 1.74 \times 10^{7}$ N/m and $K_{yz} = K_{zy} = 0$. Figure 3.32 shows the variation of the first three pairs of the bending mode of the rotating composite shaft supported on anisotropic bearings with the rotational speed.

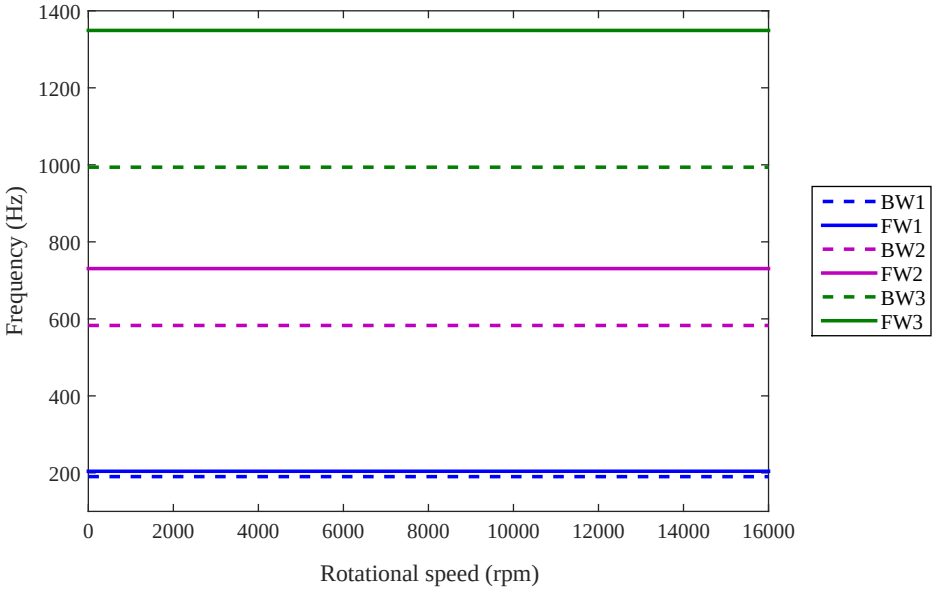

Figure 3.32. First three pairs of the bending mode of the rotating composite shaft supported on anisotropic bearings

It can be observed from figure 3.32 that the separation of the frequencies on forward and backward starts on a rotational speed equal to zero, instead of the case of isotropic bearings (the same frequency for both modes in the stationary case). This separation is due to the anisotropic bearings which make the shaft's system (shaft and bearings) asymmetric. Thus, the values of the bending frequencies are different in orthogonal directions.

3.8 Conclusion

Several examples have been processed in order to validate Equivalent Single Layer Theory and to determine the influence of different geometrical and physical parameters on rotating composite shaft dynamic behaviour. This analysis has allowed us to reach the following conclusions:

- The gyroscopic effect induces a coupling of the orthogonal displacements to the rotation axis which has the consequence of separating natural frequencies to a forward and backward movement

according to the direction of the shaft rotating movement.

- The variation of the stacking sequence and the fiber orientation has significative effects on the dynamic behaviour of rotating composite shafts.
- Dynamic characteristics such as natural frequencies and critical speeds of the rotating composite shafts are influenced by changing stacking sequences, fiber orientations, length, mean diameter, nature of the materials, rotational speeds and boundary conditions.
- Natural frequencies of the rotating steel shaft and aluminium shaft are close to those of the rotating composite shaft where the fibers of the layer are oriented at $45°$.
- Elastic bearings properties and disk positions have an important influence on the dynamic characteristics of the rotating composite shafts.

The main advances of ESLT, developed in this chapter, is the consideration of the effects of fiber orientation and stacking sequence and the direct introduction of shear-normal coupling effects. The study of other mechanical coupling effects will be presented in the following chapter by developing the Modified Equivalent Single Layer Theory (Modified ESLT).

Chapter 4

Generalized Finite Element Formulation Based on Modified Equivalent Single Layer Theory

4.1 Introduction

Similarly to Equivalent Single Layer Theory (ESLT), a multilayered composite shaft made of P orthotropic layers is considered. However, Modified Equivalent Single Layer Theory (Modified ESLT) is generalized not only to account for the location and the orientation of different layers and their stacking sequence and the shear-normal coupling effect but also to include different mechanical coupling effects.

4.2 Displacement field

The following displacement field of a rotating composite shaft is assumed by choosing the coordinate axis x to coincide with the shaft axis [Chang et al., 2004a]:

$$\{U(x,y,z,t)\} = \begin{Bmatrix} u_x(x,y,z,t) \\ u_y(x,y,z,t) \\ u_z(x,y,z,t) \end{Bmatrix} = \begin{Bmatrix} u(x,t) - y\theta_z(x,t) + z\theta_y(x,t) \\ v(x,t) - z\theta_x(x,t) \\ w(x,t) + y\theta_x(x,t) \end{Bmatrix} \tag{4.1}$$

where u_x, u_y and u_z are the displacements of a generic point of the shaft cross section in x, y and z directions. The variables $u(x,t)$, $v(x,t)$ and $w(x,t)$ are respectively the flexural displacements in x, y and z directions of the point on the reference axis of the shaft, while $\theta_y(x,t)$ and $\theta_z(x,t)$ are the rotation angles of the cross section about y and z axis respectively and $\theta_x(x,t)$ is the angular displacement of the cross section due to the torsion deformation of the shaft.

4.3 Strain field

Using equation (3.9) and the displacement field expression (4.1), the strain field can be expressed as follows:

$$\{\varepsilon\} = \begin{cases} \varepsilon_{xx} = \dfrac{\partial u}{\partial x} - y\dfrac{\partial \theta_z}{\partial x} + z\dfrac{\partial \theta_y}{\partial x} \\ \gamma_{xy} = -\theta_z + \dfrac{\partial v}{\partial x} - z\dfrac{\partial \theta_x}{\partial x} \\ \gamma_{xz} = \theta_y + \dfrac{\partial w}{\partial x} + y\dfrac{\partial \theta_x}{\partial x} \\ \varepsilon_{yy} = \varepsilon_{zz} = \gamma_{yz} = 0 \end{cases} \tag{4.2}$$

Since the shape of the shaft cross section is assumed circular, it is more convenient to express the stress-strain relations in the cylindrical coordinate system (x, r, ϕ). Using equation (3.11) and the strain field expression (4.2), the strain components in the cylindrical coordinate system (x, r, ϕ) can be expressed as follows:

$$\{\varepsilon\} = \begin{cases} \varepsilon_{xx} = \dfrac{\partial u}{\partial x} - y\dfrac{\partial \theta_z}{\partial x} + z\dfrac{\partial \theta_y}{\partial x} \\ \gamma_{x\phi} = -\gamma_{xy}\sin\phi + \gamma_{xz}\cos\phi \\ \gamma_{xr} = \gamma_{xy}\cos\phi + \gamma_{xz}\sin\phi \\ \varepsilon_{rr} = \varepsilon_{\phi\phi} = \gamma_{r\phi} = 0 \end{cases} \tag{4.3}$$

4.4 Stress field

The generalized Hooke's law for an orthotropic material where $[Q]$ is the material stiffness matrix is given by:

$$\{\sigma\} = [Q]\{\varepsilon\} \tag{4.4}$$

Using the same development as in section 3.2.3, we obtain the abbreviated form of the stress field expression in the cylindrical coordinate system (x, r, ϕ) as follows:

$$\{\sigma\} = \left[\bar{Q}\right]\{\varepsilon\} \tag{4.5}$$

where $\left[\bar{Q}\right]$ is the transformed material stiffness matrix of the layer which is expressed in equation (3.17).

4.5 Deformation energy

The composite shaft deformation energy is given by:

$$\begin{aligned} \Pi &= \frac{1}{2}\int_V \varepsilon^{\mathrm{T}}\sigma \mathrm{d}V \\ &= \frac{1}{2}\int_V \left(\sigma_{xx}\varepsilon_{xx} + \sigma_{\phi\phi}\varepsilon_{\phi\phi} + \sigma_{rr}\varepsilon_{rr} + \tau_{r\phi}\gamma_{r\phi} + \tau_{xr}\gamma_{xr} + \tau_{x\phi}\gamma_{x\phi}\right)\mathrm{d}V \end{aligned} \tag{4.6}$$

Since $\varepsilon_{\phi\phi} = \varepsilon_{rr} = \gamma_{r\phi} = 0$, the composite shaft deformation energy can be expressed as follows:

$$\Pi = \frac{1}{2}\int_V \left(\sigma_{xx}\varepsilon_{xx} + \tau_{xr}\gamma_{xr} + \tau_{x\phi}\gamma_{x\phi}\right)\mathrm{d}V \tag{4.7}$$

and the stress-strain relation expressed in equation (3.15) can be simplified as follows:

$$\begin{Bmatrix} \sigma_{xx} \\ \tau_{xr} \\ \tau_{x\phi} \end{Bmatrix} = \begin{bmatrix} \bar{Q}_{11} & 0 & \bar{Q}_{16} \\ 0 & \bar{Q}_{55} & 0 \\ \bar{Q}_{16} & 0 & \bar{Q}_{66} \end{bmatrix} \begin{Bmatrix} \varepsilon_{xx} \\ \gamma_{xr} \\ \gamma_{x\phi} \end{Bmatrix} \tag{4.8}$$

Therefore, the stress components are expressed as follows:

$$\{\sigma\} = \begin{cases} \sigma_{xx} = \bar{Q}_{11}\varepsilon_{xx} + k_s\bar{Q}_{16}\gamma_{x\phi} \\ \tau_{xr} = k_s\bar{Q}_{55}\gamma_{xr} \\ \tau_{x\phi} = k_s\bar{Q}_{16}\varepsilon_{xx} + k_s\bar{Q}_{66}\gamma_{x\phi} \end{cases} \tag{4.9}$$

where k_s is the transverse shear correction factor and $\bar{Q}_{ij}$ are the constitutive terms which are related to the laminate angle α and the elastic constants of principal axes, defined in equations (3.23). Using equations (4.7) and (4.9), the composite shaft deformation energy can be written as:

$$\Pi = \frac{1}{2}\int_V \left(\bar{Q}_{11}\varepsilon_{xx}^2 + 2k_s\bar{Q}_{16}\gamma_{x\phi}\varepsilon_{xx} + k_s\bar{Q}_{55}\gamma_{xr}^2 + k_s\bar{Q}_{66}\gamma_{x\phi}^2\right)\mathrm{d}V \tag{4.10}$$

where $2k_s\bar{Q}_{16}\gamma_{x\phi}\varepsilon_{xx}$ accounts for the shear-normal coupling effect. Replacing the relations for the cross section rotation where $y = r\cos\phi$ and $z = r\sin\phi$ as shown in figure 3.5 and integrating over the shaft cross sectional area by summing up the contribution of each orthotropic layer, the composite shaft deformation energy can be written as:

$$\begin{aligned}\Pi = {} & \frac{1}{2}D_{11}\int_0^L \left(\frac{\partial u}{\partial x}\right)^2 \mathrm{d}x + \frac{1}{2}A_{11}\int_0^L \left[\left(\frac{\partial \theta_y}{\partial x}\right)^2 + \left(\frac{\partial \theta_z}{\partial x}\right)^2\right]\mathrm{d}x + \frac{1}{2}k_sD_{66}\int_0^L \left(\frac{\partial \theta_x}{\partial x}\right)^2 \mathrm{d}x \\ & + \frac{1}{2}k_sA_{16}\int_0^L \left[2\frac{\partial \theta_x}{\partial x}\frac{\partial u}{\partial x} - \theta_y\frac{\partial \theta_z}{\partial x} - \frac{\partial \theta_z}{\partial x}\frac{\partial w}{\partial x} + \theta_z\frac{\partial \theta_y}{\partial x} - \frac{\partial \theta_y}{\partial x}\frac{\partial v}{\partial x}\right]\mathrm{d}x \\ & + \frac{1}{2}k_s\left(A_{55}+A_{66}\right)\int_0^L \left[\left(\frac{\partial v}{\partial x}\right)^2 + \left(\frac{\partial w}{\partial x}\right)^2 + \theta_y^2 + \theta_z^2 + 2\theta_y\frac{\partial w}{\partial x} - 2\theta_z\frac{\partial v}{\partial x}\right]\mathrm{d}x\end{aligned} \tag{4.11}$$

where L is the length of the composite shaft. Considering the pth layer of the composite shaft where R_{p-1} is the inner radius and R_p is the outer radius, as shown in figure 3.8, the terms A_{ij} and D_{ij}, given in equation (4.11), are expressed as follows:

$$\begin{cases} A_{11} = \dfrac{\pi}{4}\displaystyle\sum_{p=1}^{P}\bar{Q}_{11p}\left(R_p^4 - R_{p-1}^4\right) \\ A_{16} = \dfrac{2\pi}{3}\displaystyle\sum_{p=1}^{P}\bar{Q}_{16p}\left(R_p^3 - R_{p-1}^3\right) \\ A_{55} = \dfrac{\pi}{2}\displaystyle\sum_{p=1}^{P}\bar{Q}_{55p}\left(R_p^2 - R_{p-1}^2\right) \\ A_{66} = \dfrac{\pi}{2}\displaystyle\sum_{p=1}^{P}\bar{Q}_{66p}\left(R_p^2 - R_{p-1}^2\right) \\ D_{11} = \pi\displaystyle\sum_{p=1}^{P}\bar{Q}_{11p}\left(R_p^2 - R_{p-1}^2\right) \\ D_{66} = \dfrac{\pi}{2}\displaystyle\sum_{p=1}^{P}\bar{Q}_{66p}\left(R_p^4 - R_{p-1}^4\right) \end{cases} \tag{4.12}$$

4.6 Kinetic energy

The kinetic energy of the rotating composite shaft including the effects of translatory and rotary inertia as well as gyroscopic ones is described as:

$$T = \frac{1}{2}\int_0^L \rho A\left(\dot{u}^2 + \dot{v}^2 + \dot{w}^2\right)\mathrm{d}x + \frac{1}{2}\int_0^L \rho\Gamma_{R/R_0}.\Big(\left[J_{/P}\right]\Gamma_{R/R_0}\Big)\mathrm{d}x \tag{4.13}$$

where ρ is the shaft mass density and A is the shaft cross sectional area. As defined in figure 2.2, u, v and w denote respectively the coordinates of the point C in x, y and z directions on the shaft reference axis. The tensor of inertia in C, as xyz are principal directions of inertia and considering the symmetry, is given by:

$$\left[J_{/C}\right] = \begin{bmatrix} I_x & 0 & 0 \\ 0 & I_y & 0 \\ 0 & 0 & I_y \end{bmatrix} \tag{4.14}$$

The angular velocity vector given in equation (2.4) is expressed as follows:

$$\Gamma_{R/R_0} = \begin{Bmatrix} \dot{\Psi} - \dot{\theta}_z \sin\theta_y \\ -\dot{\theta}_z \cos\theta_y \sin\Psi + \dot{\theta}_y \cos\Psi \\ \dot{\theta}_z \cos\theta_y \cos\Psi + \dot{\theta}_y \sin\Psi \end{Bmatrix} \tag{4.15}$$

where $\dot{\theta}_z$, $\dot{\theta}_y$ and $\dot{\Psi}$ can be regarded as the Euler's angles and represent respectively the rotation angles of the cross section about z, y_1 and x_2 axes as shown in figure 2.2. $\dot{\Psi}$, $\dot{\theta}_y$ and $\dot{\theta}_z$ are the derivatives with respect to time of the angular displacements along x, y and z axes respectively. The rotation Ψ can be resolved into two parts as $\Psi = \theta_x + \Omega t$, where θ_x is the angular displacement of the cross section due to the shaft torsion deformation and Ω is the shaft rotational speed which is assumed constant.

Therefore, using the kinetic energy expression (4.13), the tensor of inertia expression (4.14) and the angular velocity vector expression (4.15), the rotating composite shaft kinetic energy can be written as:

$$\begin{aligned} T = \frac{1}{2}\int_0^L \Big[& \rho A\left(\dot{u}^2 + \dot{v}^2 + \dot{w}^2\right) + \rho I_x \left(\dot{\theta}_x^2 + \Omega^2 + \dot{\theta}_z^2 \sin^2\theta_y + 2\Omega\dot{\theta}_x - 2\dot{\theta}_x\dot{\theta}_z \sin\theta_y - 2\Omega\dot{\theta}_z \sin\theta_y\right) \\ & + \rho I_y \left(\dot{\theta}_z^2 \cos^2\theta_y \sin^2\Psi + \dot{\theta}_y^2 \cos^2\Psi + \dot{\theta}_z^2 \cos^2\theta_y \cos^2\Psi + \dot{\theta}_y^2 \sin^2\Psi\right)\Big] \mathrm{d}x \end{aligned} \tag{4.16}$$

In equation (4.16), the angles Ψ, θ_y and θ_z are assumed small. Integrating over the shaft cross sectional area by summing up the contribution of each orthotropic layer, the kinetic energy of the rotating laminated shaft including the effects of translatory and rotary inertia as well as the gyroscopic ones can be expressed as follow:

$$T = \frac{1}{2}\int_0^L \left[I_m\left(\dot{u}^2 + \dot{v}^2 + \dot{w}^2\right) + I_d\left(\dot{\theta}_y^2 + \dot{\theta}_z^2\right) + I_p\dot{\theta}_x^2 + I_p\Omega^2 + 2I_p\Omega\dot{\theta}_x - 2I_p\Omega\theta_y\dot{\theta}_z \right] \mathrm{d}x \tag{4.17}$$

where $I_d\left(\dot{\theta}_y^2 + \dot{\theta}_z^2\right)$ represents the rotary inertia effect and $2I_p\Omega\theta_y\dot{\theta}_z$ accounts for the gyroscopic effect. The mass quantity I_m denotes the mass per unit length of the composite shaft, while I_d and I_p denote respectively the diametrical and the polar moment of inertia of the shaft cross section, defined in equation (3.32).

4.7 Variational formulation

Hamilton's principle is herein adopted (see section 3.1):

$$\delta \int_{t_i}^{t_f} \left(T - \Pi\right) \mathrm{d}t = 0 \tag{4.18}$$

Introducing kinetic energy T expression (4.17) and deformation energy Π expression (4.11) into Hamilton's principle (4.18) and performing the variation and an integration by parts, and since the above stated Hamilton's principle must be verified for an arbitrary $\{\delta d\} = \{\delta u, \delta v, \delta w, \delta\theta_x, \delta\theta_y, \delta\theta_z\}^{\mathrm{T}}$, the variational statement can be expressed as follows:

$$\begin{aligned}
&\int_0^L \left[\delta u I_m \ddot{u} + \delta v I_m \ddot{v} + \delta w I_m \ddot{w} + \delta\theta_y I_d \ddot{\theta}_y + \delta\theta_z I_d \ddot{\theta}_z + \delta\theta_x I_p \ddot{\theta}_x + \delta\theta_y I_p \Omega \dot{\theta}_z - \delta\theta_z I_p \Omega \dot{\theta}_y\right] \mathrm{d}x \\
&+ \int_0^L \Bigg[\frac{\partial}{\partial x}(\delta u) N_x + \frac{\partial}{\partial x}(\delta v)\left(Q_{xr}^{(2)} - Q_{x\phi}^{(1)}\right) + \frac{\partial}{\partial x}(\delta w)\left(Q_{xr}^{(1)} + Q_{x\phi}^{(2)}\right) + \delta\theta_y\left(Q_{xr}^{(1)} + Q_{x\phi}^{(2)}\right) \\
&\qquad + \delta\theta_z\left(Q_{x\phi}^{(1)} - Q_{xr}^{(2)}\right) + \frac{\partial}{\partial x}(\delta\theta_x) M_{x\phi} + \frac{\partial}{\partial x}(\delta\theta_y) M_y \\
&\qquad + \frac{\partial}{\partial x}(\delta\theta_z) M_z \Bigg] \mathrm{d}x = 0 \quad \forall\, \delta u, \delta v, \delta w, \delta\theta_x, \delta\theta_y, \delta\theta_z
\end{aligned} \tag{4.19}$$

where the stress resultants N_x, $Q_{xr}^{(1)}$, $Q_{xr}^{(2)}$, $Q_{x\phi}^{(1)}$, $Q_{x\phi}^{(2)}$ are defined as follows:

$$\begin{cases}
N_x = D_{11}\dfrac{\partial u}{\partial x} + k_s A_{16}\dfrac{\partial\theta_x}{\partial x} \\
Q_{xr}^{(1)} = k_s A_{55}\left(\theta_y + \dfrac{\partial w}{\partial x}\right) \\
Q_{xr}^{(2)} = k_s A_{55}\left(-\theta_z + \dfrac{\partial v}{\partial x}\right) \\
Q_{x\phi}^{(1)} = \dfrac{1}{2}k_s A_{16}\dfrac{\partial\theta_y}{\partial x} + k_s A_{66}\left(\theta_z - \dfrac{\partial v}{\partial x}\right) \\
Q_{x\phi}^{(2)} = -\dfrac{1}{2}k_s A_{16}\dfrac{\partial\theta_z}{\partial x} + k_s A_{66}\left(\theta_y + \dfrac{\partial w}{\partial x}\right)
\end{cases} \tag{4.20}$$

and the stress couples $M_{x\phi}$, M_y, M_z being defined as follows:

$$\begin{cases}
M_{x\phi} = k_s A_{16}\dfrac{\partial u}{\partial x} + k_s D_{66}\dfrac{\partial\theta_x}{\partial x} \\
M_y = A_{11}\dfrac{\partial\theta_y}{\partial x} + \dfrac{1}{2}k_s A_{16}\left(\theta_z - \dfrac{\partial v}{\partial x}\right) \\
M_z = A_{11}\dfrac{\partial\theta_z}{\partial x} - \dfrac{1}{2}k_s A_{16}\left(\theta_y + \dfrac{\partial w}{\partial x}\right)
\end{cases} \tag{4.21}$$

4.8 Finite element definition

The developed finite element has two nodes as shown in figure 4.1. In this case, for each node, the element has six degrees of freedom: three displacements u, v, and w and three slopes about x, y and z axes denoted respectively θ_x, θ_y and θ_z.

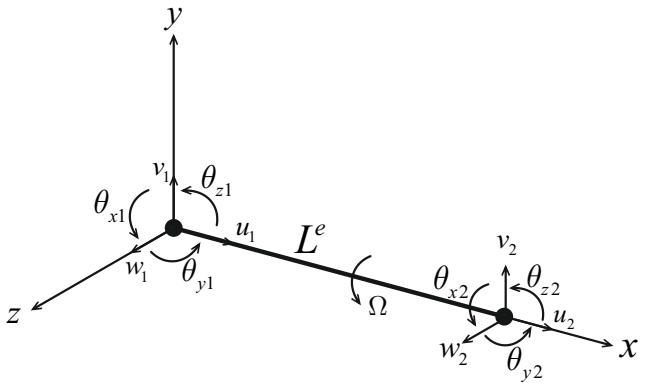

Figure 4.1. Shaft finite element

The displacement interpolations can be defined as follow:

$$\begin{aligned} u &= \sum_{i=1}^{2} N_i u_i \qquad v = \sum_{i=1}^{2} N_i v_i \qquad w = \sum_{i=1}^{2} N_i w_i \\ \theta_x &= \sum_{i=1}^{2} N_i \theta_{x_i} \qquad \theta_y = \sum_{i=1}^{2} N_i \theta_{y_i} \qquad \theta_z = \sum_{i=1}^{2} N_i \theta_{z_i} \end{aligned} \tag{4.22}$$

Using the matrical notation, let:

$$u = N_u q^e \quad v = N_v q^e \quad w = N_w q^e \quad \theta_x = N_{\theta_x} q^e \quad \theta_y = N_{\theta_y} q^e \quad \theta_z = N_{\theta_z} q^e \tag{4.23}$$

$$\frac{\partial u}{\partial x} = B_u q^e \quad \frac{\partial v}{\partial x} = B_v q^e \quad \frac{\partial w}{\partial x} = B_w q \quad \frac{\partial \theta_x}{\partial x} = B_{\theta_x} q^e \quad \frac{\partial \theta_y}{\partial x} = B_{\theta_y} q^e \quad \frac{\partial \theta_z}{\partial x} = B_{\theta_z} q^e \tag{4.24}$$

where the elemental vector of nodal degrees of freedom, shape functions matrices and deformation matrices are formed as follows:

$$\{q^e\} = \begin{Bmatrix} u_1 & v_1 & w_1 & \theta_{x_1} & \theta_{y_1} & \theta_{z_1} & u_2 & v_2 & w_2 & \theta_{x_2} & \theta_{y_2} & \theta_{z_2} \end{Bmatrix}^{\mathrm{T}} \tag{4.25}$$

$$\begin{aligned} N_u &= \begin{bmatrix} N_1 & 0 & 0 & 0 & 0 & 0 & N_2 & 0 & 0 & 0 & 0 & 0 \end{bmatrix} \\ N_v &= \begin{bmatrix} 0 & N_1 & 0 & 0 & 0 & 0 & 0 & N_2 & 0 & 0 & 0 & 0 \end{bmatrix} \\ N_w &= \begin{bmatrix} 0 & 0 & N_1 & 0 & 0 & 0 & 0 & 0 & N_2 & 0 & 0 & 0 \end{bmatrix} \\ N_{\theta_x} &= \begin{bmatrix} 0 & 0 & 0 & N_1 & 0 & 0 & 0 & 0 & 0 & N_2 & 0 & 0 \end{bmatrix} \\ N_{\theta_y} &= \begin{bmatrix} 0 & 0 & 0 & 0 & N_1 & 0 & 0 & 0 & 0 & 0 & N_2 & 0 \end{bmatrix} \\ N_{\theta_z} &= \begin{bmatrix} 0 & 0 & 0 & 0 & 0 & N_1 & 0 & 0 & 0 & 0 & 0 & N_2 \end{bmatrix} \end{aligned} \tag{4.26}$$

$$
\begin{aligned}
B_u &= J^{-1}\begin{bmatrix} \frac{\partial N_1}{\partial \xi} & 0 & 0 & 0 & 0 & 0 & \frac{\partial N_2}{\partial \xi} & 0 & 0 & 0 & 0 & 0 \end{bmatrix} \\
B_v &= J^{-1}\begin{bmatrix} 0 & \frac{\partial N_1}{\partial \xi} & 0 & 0 & 0 & 0 & 0 & \frac{\partial N_2}{\partial \xi} & 0 & 0 & 0 & 0 \end{bmatrix} \\
B_w &= J^{-1}\begin{bmatrix} 0 & 0 & \frac{\partial N_1}{\partial \xi} & 0 & 0 & 0 & 0 & 0 & \frac{\partial N_2}{\partial \xi} & 0 & 0 & 0 \end{bmatrix} \\
B_{\theta_x} &= J^{-1}\begin{bmatrix} 0 & 0 & 0 & \frac{\partial N_1}{\partial \xi} & 0 & 0 & 0 & 0 & 0 & \frac{\partial N_2}{\partial \xi} & 0 & 0 \end{bmatrix} \\
B_{\theta_y} &= J^{-1}\begin{bmatrix} 0 & 0 & 0 & 0 & \frac{\partial N_1}{\partial \xi} & 0 & 0 & 0 & 0 & 0 & \frac{\partial N_2}{\partial \xi} & 0 \end{bmatrix} \\
B_{\theta_z} &= J^{-1}\begin{bmatrix} 0 & 0 & 0 & 0 & 0 & \frac{\partial N_1}{\partial \xi} & 0 & 0 & 0 & 0 & 0 & \frac{\partial N_2}{\partial \xi} \end{bmatrix}
\end{aligned}
\tag{4.27}
$$

4.9 Weak form finite element discretization

The global weak form described in equation (4.19) can be expressed as the sum of the elemental forms leading to the definition of the elemental matrices. Adding the contribution of all the E finite elements, the global form can be expressed as:

$$
\begin{aligned}
\sum_{e=1}^{E}\Bigg(\int_0^{L^e} &\left[\delta u I_m \ddot{u} + \delta v I_m \ddot{v} + \delta w I_m \ddot{w} + \delta\theta_y I_d \ddot{\theta}_y + \delta\theta_z I_d \ddot{\theta}_z + \delta\theta_x I_p \ddot{\theta}_x + \delta\theta_y I_p \Omega \dot{\theta}_z - \delta\theta_z I_p \Omega \dot{\theta}_y\right] \mathrm{d}x \\
&+ \int_0^{L^e} \Bigg[\frac{\partial}{\partial x}(\delta u) N_x + \frac{\partial}{\partial x}(\delta v)\left(Q_{xr}^{(2)} - Q_{x\phi}^{(1)}\right) + \frac{\partial}{\partial x}(\delta w)\left(Q_{xr}^{(1)} + Q_{x\phi}^{(2)}\right) + \delta\theta_y\left(Q_{xr}^{(1)} + Q_{x\phi}^{(2)}\right) \\
&\quad + \delta\theta_z\left(Q_{x\phi}^{(1)} - Q_{xr}^{(2)}\right) + \frac{\partial}{\partial x}(\delta\theta_x) M_{x\phi} + \frac{\partial}{\partial x}(\delta\theta_y) M_y + \frac{\partial}{\partial x}(\delta\theta_z) M_z \Bigg] \mathrm{d}x \Bigg) = 0
\end{aligned}
\tag{4.28}
$$

where the generalized variables are restricted to the domain of integration L^e and an approximation is considered at a local level in each finite element as stated in equation (4.22).

The relation between the elemental degrees of freedom and the global ones is established through the connectivity matrices $[R^e]$, expressed as:

$$
\{q^e\} = [R^e]\{q\} \tag{4.29}
$$

where $\{q\}$ represents the vector of global degrees of freedom.

Substituting equation (4.22) into equation (4.28) yields:

$$
\sum_{e=1}^{E}\left(\{\delta q^e\}^{\mathrm{T}}[M^e]\{\ddot{q}^e\} + \{\delta q^e\}^{\mathrm{T}}[G^e(\Omega)]\{\dot{q}^e\} + \{\delta q^e\}^{\mathrm{T}}[K^e]\{q^e\}\right) = 0 \tag{4.30}
$$

where the elementary mass matrix $[M^e]$, the elementary gyroscopic matrix $[G^e(\Omega)]$ and the elementary stiffness matrix $[K^e]$ are given by:

$$
[M^e]_{12\times 12} = \begin{bmatrix} [M_u] & 0 & 0 & 0 & 0 & 0 \\ 0 & [M_v] & 0 & 0 & 0 & 0 \\ 0 & 0 & [M_w] & 0 & 0 & 0 \\ 0 & 0 & 0 & [M_{\theta_x}] & 0 & 0 \\ 0 & 0 & 0 & 0 & \left[M_{\theta_y}\right] & 0 \\ 0 & 0 & 0 & 0 & 0 & [M_{\theta_z}] \end{bmatrix} \tag{4.31}
$$

$$[G^e(\Omega)]_{12\times12} = \begin{bmatrix} 0 & 0 & 0 & 0 & 0 & 0 \\ 0 & 0 & 0 & 0 & 0 & 0 \\ 0 & 0 & 0 & 0 & 0 & 0 \\ 0 & 0 & 0 & 0 & 0 & 0 \\ 0 & 0 & 0 & 0 & 0 & [G_1(\Omega)] \\ 0 & 0 & 0 & 0 & -[G_1(\Omega)]^{\mathrm{T}} & 0 \end{bmatrix} \tag{4.32}$$

$$[K^e]_{12\times12} = \begin{bmatrix} [K_u] & 0 & 0 & [K_1] & 0 & 0 \\ 0 & [K_v] & 0 & 0 & [K_2] & [K_3] \\ 0 & 0 & [K_w] & 0 & [K_4] & [K_5] \\ [K_1]^{\mathrm{T}} & 0 & 0 & [K_{\theta_x}] & 0 & 0 \\ 0 & [K_2]^{\mathrm{T}} & [K_4]^{\mathrm{T}} & 0 & [K_{\theta_y}] & [K_6] \\ 0 & [K_3]^{\mathrm{T}} & [K_5]^{\mathrm{T}} & 0 & [K_6]^{\mathrm{T}} & [K_{\theta_z}] \end{bmatrix} \tag{4.33}$$

The elementary mass components, given in equation (4.31), are expressed as follow:

$$\begin{cases} [M_u]_{2\times2} = \displaystyle\int_{-1}^{1} N_u^{\mathrm{T}} I_m N_u \det(J)\,\mathrm{d}\xi \\ [M_v]_{2\times2} = \displaystyle\int_{-1}^{1} N_v^{\mathrm{T}} I_m N_v \det(J)\,\mathrm{d}\xi \\ [M_w]_{2\times2} = \displaystyle\int_{-1}^{1} N_w^{\mathrm{T}} I_m N_w \det(J)\,\mathrm{d}\xi \\ [M_{\theta_x}]_{2\times2} = \displaystyle\int_{-1}^{1} N_{\theta_x}^{\mathrm{T}} I_p N_{\theta_x} \det(J)\,\mathrm{d}\xi \\ [M_{\theta_y}]_{2\times2} = \displaystyle\int_{-1}^{1} N_{\theta_y}^{\mathrm{T}} I_d N_{\theta_y} \det(J)\,\mathrm{d}\xi \\ [M_{\theta_z}]_{2\times2} = \displaystyle\int_{-1}^{1} N_{\theta_z}^{\mathrm{T}} I_d N_{\theta_z} \det(J)\,\mathrm{d}\xi \end{cases} \tag{4.34}$$

The components of the elementary gyroscopic matrix are given as follows:

$$[G_1(\Omega)]_{2\times2} = \Omega \int_{-1}^{1} N_{\theta_y}^{\mathrm{T}} I_p N_{\theta_z} \det(J)\,\mathrm{d}\xi \tag{4.35}$$

The elementary stiffness terms, given in equation (4.33), are expressed as follows:

$$\begin{cases} [K_u]_{2\times2} = \displaystyle\int_{-1}^{1} B_u^{\mathrm{T}} D_{11} B_u \det(J)\,\mathrm{d}\xi \\ [K_1]_{2\times2} = \displaystyle\int_{-1}^{1} B_u^{\mathrm{T}} k_s A_{16} B_{\theta_x} \det(J)\,\mathrm{d}\xi \\ [K_v]_{2\times2} = -\displaystyle\int_{-1}^{1} B_v^{\mathrm{T}} k_s (A_{55}+A_{66}) B_v \det(J)\,\mathrm{d}\xi \\ [K_2]_{2\times2} = -\dfrac{1}{2}\displaystyle\int_{-1}^{1} B_v^{\mathrm{T}} k_s A_{16} B_{\theta_y} \det(J)\,\mathrm{d}\xi \\ [K_3]_{2\times2} = \displaystyle\int_{-1}^{1} B_v^{\mathrm{T}} k_s (A_{55}+A_{66}) N_{\theta_z} \det(J)\,\mathrm{d}\xi \\ [K_w]_{2\times2} = \displaystyle\int_{-1}^{1} B_w^{\mathrm{T}} k_s (A_{55}+A_{66}) B_w \det(J)\,\mathrm{d}\xi \end{cases} \tag{4.36}$$

$$\begin{cases} [K_4]_{2\times2} = \displaystyle\int_{-1}^{1} B_w^{\mathrm{T}} k_s \left(A_{55} + A_{66}\right) N_{\theta_y} \det\left(J\right) \mathrm{d}\xi \\ [K_5]_{2\times2} = -\dfrac{1}{2} \displaystyle\int_{-1}^{1} B_w^{\mathrm{T}} k_s A_{16} B_{\theta_z} \det\left(J\right) \mathrm{d}\xi \\ [K_{\theta_x}]_{2\times2} = \displaystyle\int_{-1}^{1} B_{\theta_x}^{\mathrm{T}} k_s D_{66} B_{\theta_x} \det\left(J\right) \mathrm{d}\xi \\ \left[K_{\theta_y}\right]_{2\times2} = \displaystyle\int_{-1}^{1} B_{\theta_y}^{\mathrm{T}} A_{11} B_{\theta_y} \det\left(J\right) \mathrm{d}\xi + \int_{-1}^{1} N_{\theta_y}^{\mathrm{T}} k_s \left(A_{55} + A_{66}\right) N_{\theta_y} \det\left(J\right) \mathrm{d}\xi \\ [K_6]_{2\times2} = \dfrac{1}{2} \displaystyle\int_{-1}^{1} B_{\theta_y}^{\mathrm{T}} k_s A_{16} N_{\theta_z} \det\left(J\right) \mathrm{d}\xi - \frac{1}{2} \int_{-1}^{1} B_{\theta_z}^{\mathrm{T}} k_s A_{16} N_{\theta_y} \det\left(J\right) \mathrm{d}\xi \\ [K_{\theta_z}]_{2\times2} = \displaystyle\int_{-1}^{1} B_{\theta_z}^{\mathrm{T}} A_{11} B_{\theta_z} \det\left(J\right) \mathrm{d}\xi + \int_{-1}^{1} N_{\theta_z}^{\mathrm{T}} k_s \left(A_{55} + A_{66}\right) N_{\theta_z} \det\left(J\right) \mathrm{d}\xi \end{cases} \tag{4.37}$$

The elementary mass, gyroscopic and stiffness matrices are thus obtained as the sum of the contribution of each orthotropic layer through the terms defined in equations (3.32) and (4.12).

4.10 Results and discussion

4.10.1 Validation of Modified Equivalent Single Layer Theory formulation

The lowest critical speeds of a composite shaft are analysed and compared with those available in the literature to validate the present model. The simply supported composite hollow shaft made of boron/epoxy, which was first studied by [Zinberg and Symonds, 1970], then by [Singh and Gupta, 1996a] and [Gubran and Gupta, 2005] and recently by [Sino et al., 2008] is investigated here. The geometric and material properties of the boron/epoxy shaft are:

- $L = 2.47$ m, mean radius $= R_m = 0.0635$ m, wall thickness $= h = 0.132 \times 10^{-3}$ m;
- $E_1 = 211$ GPa, $E_2 = 24.1$ GPa, $G_{ij} = 6.9$ GPa, $\nu_{12} = 0.36$, $\rho = 1967$ kg/m^3;
- 10 layers of equal thickness from the inner layer $[90°, 45°, -45°, [0°]_6, 90°]$;
- Shear correction factor: $k_s = 1/2$.

The first critical speed obtained by different investigators using different formulations is given in table 4.1. Percentages shown in table 4.1 are those of the difference between critical speed obtained using ESLT and Modified ESLT and those obtained using different formulations available in the literature.

Table 4.1. Comparison of the first critical speed (rpm) obtained by different investigators

Investigators	Critical speed (rpm)	%	Methods
[Zinberg and Symonds, 1970]	5500	4.7%	Experimental, forced vibration resonance for the shaft supported on rolling element bearing conditions but under non-rotating conditions.
	5780	0.2%	Equivalent Modulus Beam Theory (EMBT)
[Singh and Gupta, 1996a]	5746	0.4%	EMBT
	5620	2.6%	Layerwise Beam Theory (LBT)
[Gubran and Gupta, 2005]	5552	3.8%	Modified EMBT
	5820	0.9%	LBT
[Sino et al., 2008]	5435	5.8%	Simplified Homogenized Beam Theory (SHBT)
Present work	5769		Equivalent Single Layer Theory (ESLT)
	5769		Modified Equivalent Single Layer Theory (Modified ESLT)

Comparing different results, it appears that results obtained using ESLT and Modified ESLT are close to those obtained using EMBT proposed by [Zinberg and Symonds, 1970] and [Singh and Gupta, 1996a] and LBT proposed by [Gubran and Gupta, 2005]. [Singh and Gupta, 1996a,b] showed that EMBT is adequate for estimation of critical speeds but may predict inaccurate results for non-symmetric stacking sequences. On the other hand, authors showed that LBT reduced from shell theory avoids the main drawbacks associated with EMBT but this method requires the development of a complex beam element with a high number of degrees of freedom dependent on the number of layers. Therefore, it can be concluded that ESLT and Modified ESLT are quite adequate for the dynamic analysis of rotating composite shafts. In fact, both theories present the same bending behaviour. The only difference that Modified ESLT includes also the stretching and the twisting behaviours.

In order to show the influence of mechanical couplings on the dynamic behaviour of the structure, a rotor of the same geometric and materials properties as the rotor test (section 3.7.1), clamped at one extremity and with one rigid steel disk at the free extremity is analysed in all subsequent subsections. The considered stacking sequence is $[90, 0, 90, 45, 90, 45, 0, 90]$. The different mechanical coupling effects which will be studied in following are: bending-bending, bending-shear and stretching-twisting coupling effects. The bending-bending and shear-normal coupling effects are introduced through both theories (ESLT and Modified ESLT) at the displacement field expression of each one. While, stretching-twisting coupling effect is introduced only through Modified ESLT. Modified ESLT will be used for the analysis of mechanical coupling effects on the dynamic behaviour of the rotor in the following sections.

4.10.2 Bending-bending coupling effect

Considering the rotating modal analysis and the frequency response function of transfer receptance type of the rotating composite shaft.

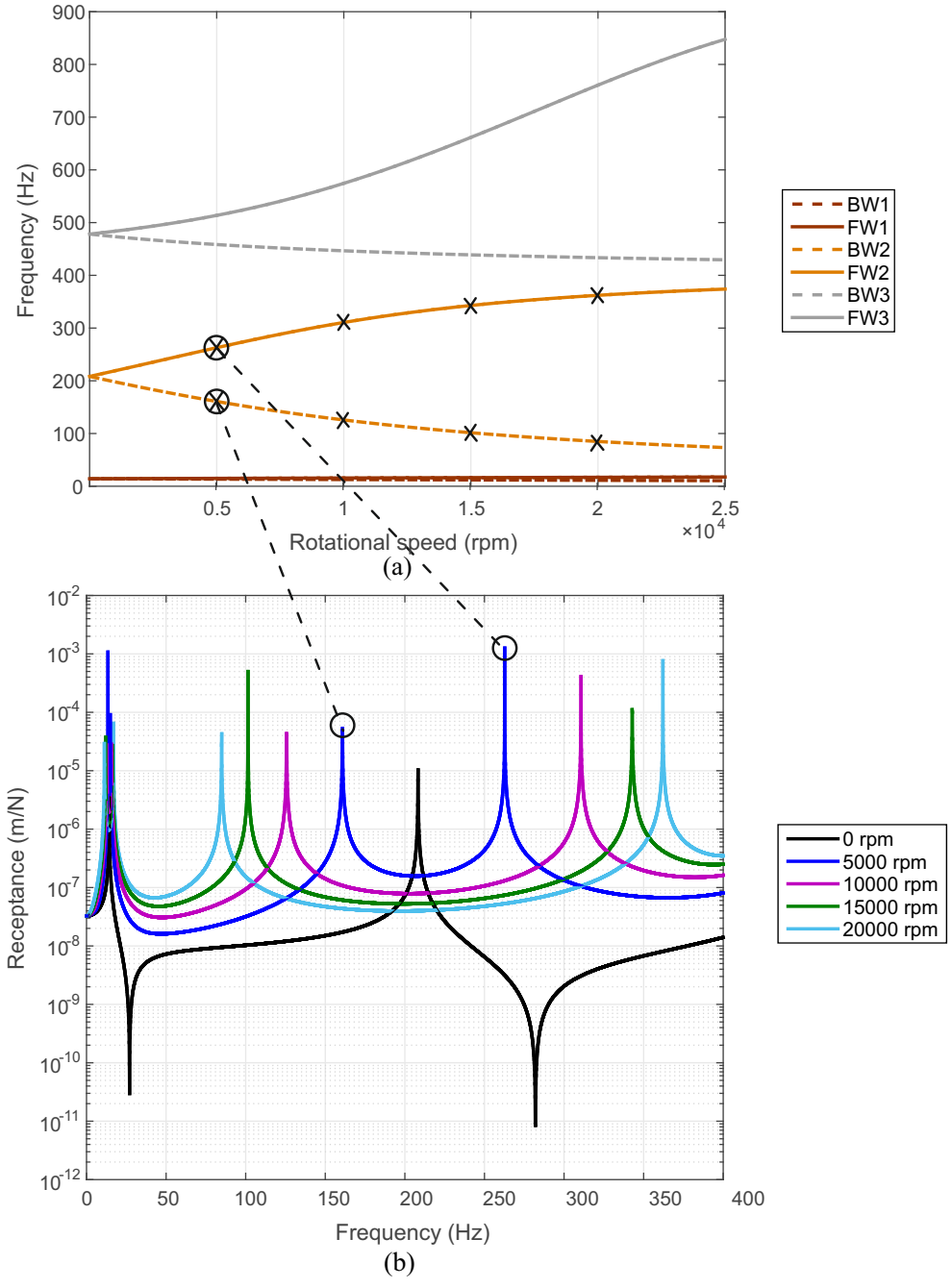

Figure 4.2. Bending-bending coupling effect

As shown in figure 4.2(b), in the case of rotating shaft, the coupling between bending along y and z directions is present. It can be observed also from figure 4.2(a) that the gyroscopic effect is more important for higher bending frequencies and for higher rotational speeds which it is confirmed in figure

4.2(b) where the difference between the third and the fourth bending frequencies is more higher when the rotational speed are increasing. When we pass to the fifth and the sixth bending frequencies the difference will be more higher for higher rotational speed.

To illustrate the bending-bending coupling effect, a stacking sequence which consists of one single layer $[\alpha]$ is now considered. Figures 4.3, 4.4 and 4.5 give the frequency response function of transfer receptance type using ESLT for different fiber angles: $60°$, $90°$ and $180°$ respectively.

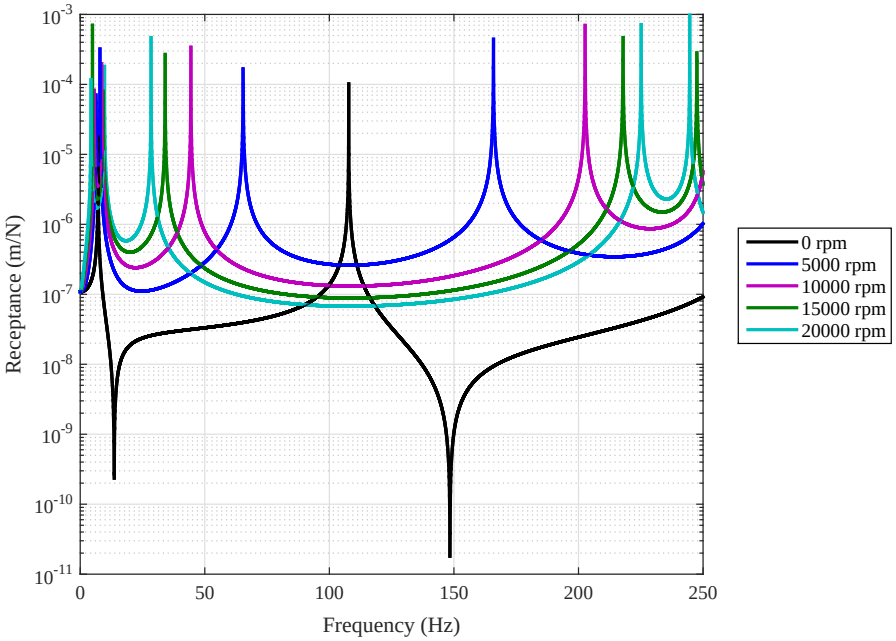

Figure 4.3. Bending-bending coupling effect, case: $60°$ fiber angle

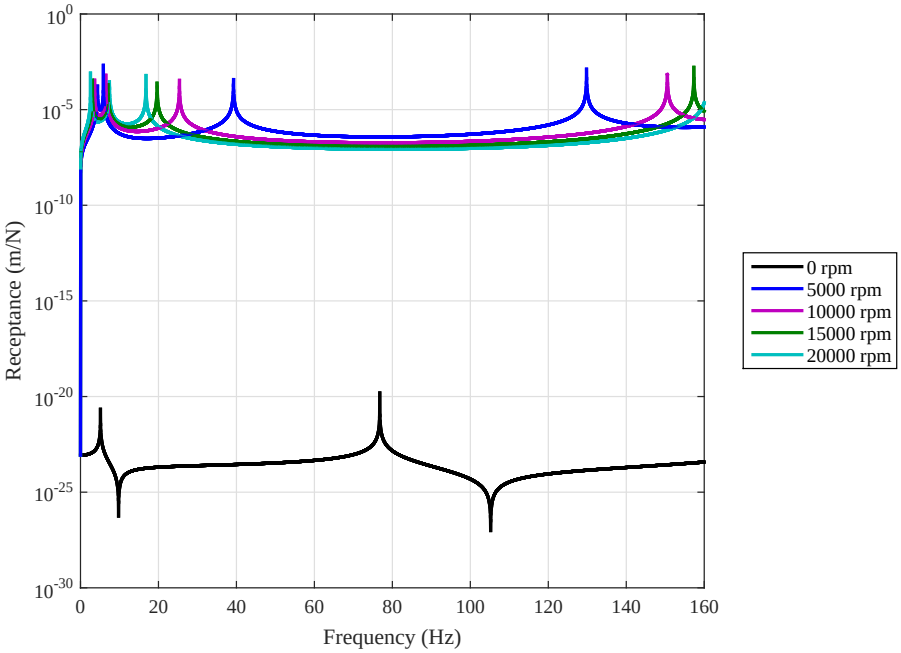

Figure 4.4. Bending-bending coupling effect, case: $90°$ fiber angle

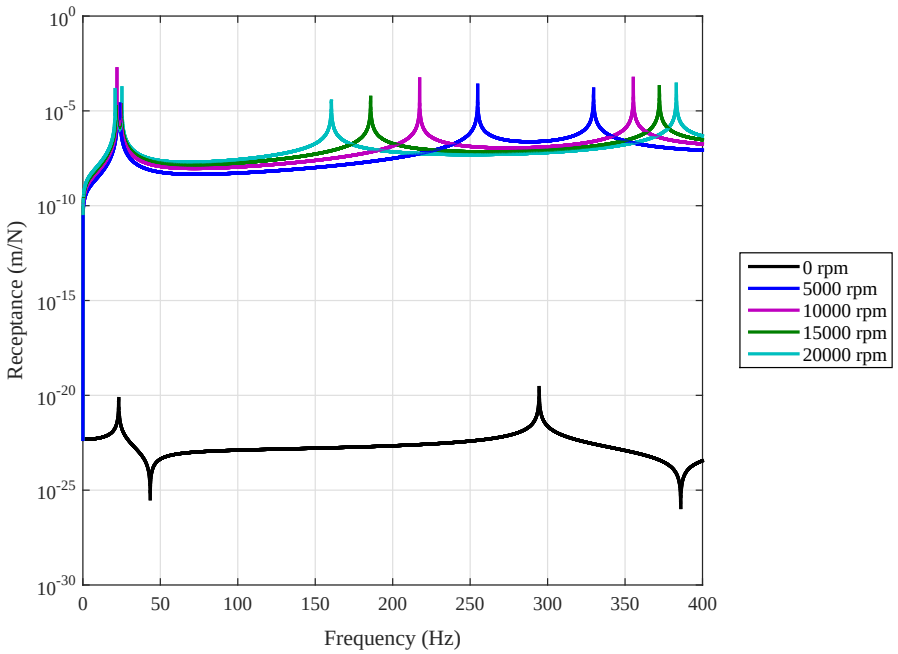

Figure 4.5. Bending-bending coupling effect, case: $180°$ fiber angle

It can be observed from figures 4.4 and 4.5 that for the case of non rotating shaft for $90°$ and $180°$ fiber angles, the bending-bending coupling effect can be neglected and assumed not present as for $0°$ fiber angle. While, it can be observed from figure 4.3 that for the case of non rotating shaft for $60°$ fiber angle, the bending-bending coupling effect is present. However, in the case of the rotating shaft, the bending-bending coupling effect is always present for different fiber orientation angles. Primary, this is due to the gyroscopic effect and the fiber orientation effect.

4.10.3 Shear-normal coupling effect

In the case of rotating shaft, the shear-normal coupling in (x, y) plane is present as shown in figure 4.6 due to the presence of the coupling terms in the stiffness matrix between v and θ_z (see equation (3.53)). The same results will be found for the shear-normal coupling in (x, z) plane.

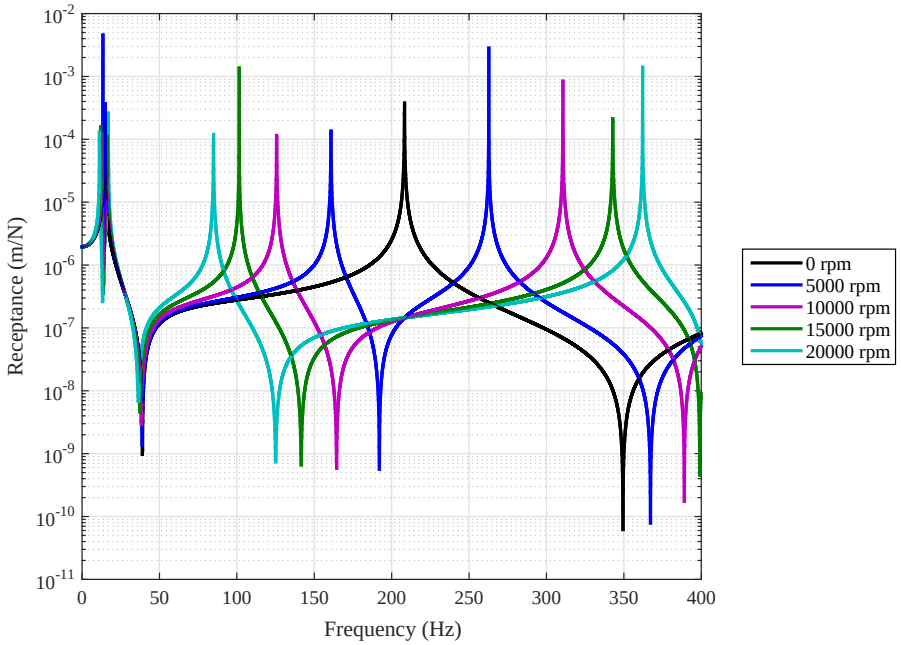

Figure 4.6. Shear-normal coupling effect

It can be observed that the bending natural frequencies shown in table 4.2 are the same as the natural frequencies (see figure 4.6) given by the shear-normal coupling which confirms the presence of the coupling between the bending and the shear.

Table 4.2. First and second pairs of bending modes (Hz)

Rotational speed (rpm)	BW1	FW1	BW2	FW2
0	13.1	13.1	186.0	186.0
5000	12.4	13.8	140.5	235.6
10000	11.7	14.5	107.6	272.6
15000	10.9	15.0	85.70	293.5
20000	10.2	15.6	71.30	305.0

4.10.4 Stretching-twisting coupling effect

A rotor of the same geometric and materials properties as the test rotor (section 3.7.1) without discs and mounted on rigid supports ($K_{yy} = K_{zz} = 1 \times 10^7$ N/m) is considered. The stacking sequence is $[90, 0, 90, 45, 90, 45, 0, 90]$. In order to show the stretching-twisting coupling effect as predicted by the Modified ESLT on the dynamic behaviour of the structure, natural frequencies values are calculated in the non rotating case and are given in table 4.3. The 7th mode and the 10th mode indicate the natural frequencies for the twisting and the stretching modes.

Table 4.3. Natural frequencies (Hz) using Modified ESLT

1st pair bending mode	2nd pair bending mode	3rd pair bending mode	7th mode	4th pair bending mode	10th mode
181	505	833	886	1317	1778

In order to analyse the gyroscopic effect on the twisting and the stretching behaviours, figure 4.7 is considered. As we can see from the figure, by changing the rotational speed, there is no change in the curve of twisting and stretching. So, the gyroscopic effect has not an influence on the stretching and the twisting behaviours.

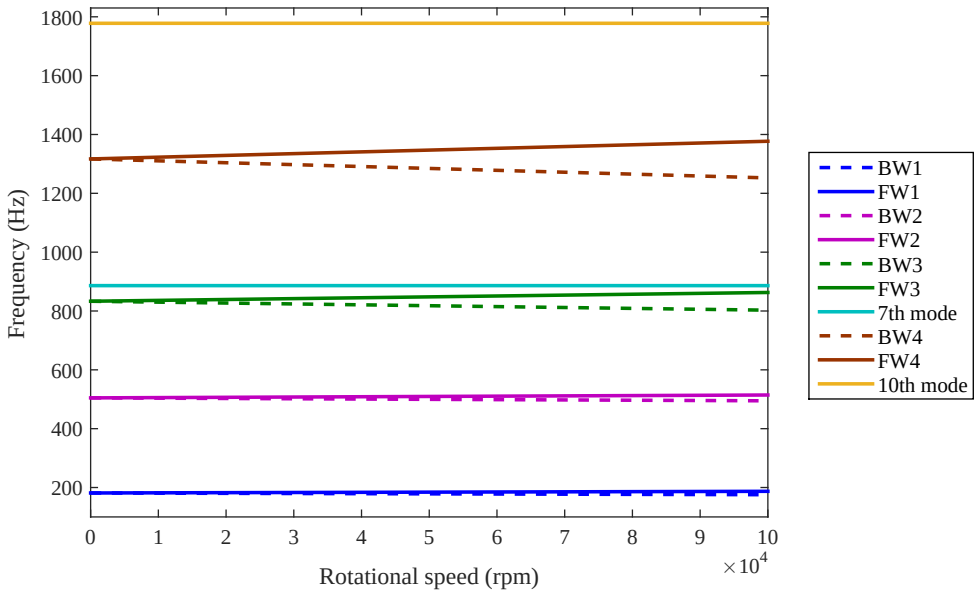

Figure 4.7. Gyroscopic effect on the twisting and the stretching frequencies

It can be seen from figure 4.8 that the three curves have the same natural frequencies which are 886 Hz and 1778 Hz as given in table 4.3. Even when we tried to uncouple the stretching and the twisting by using the same nature of excitation and response, we found the same natural frequencies. These results show that the two effects can not be uncoupled. In all cases, the coupling between the stretching and the twisting will be present.

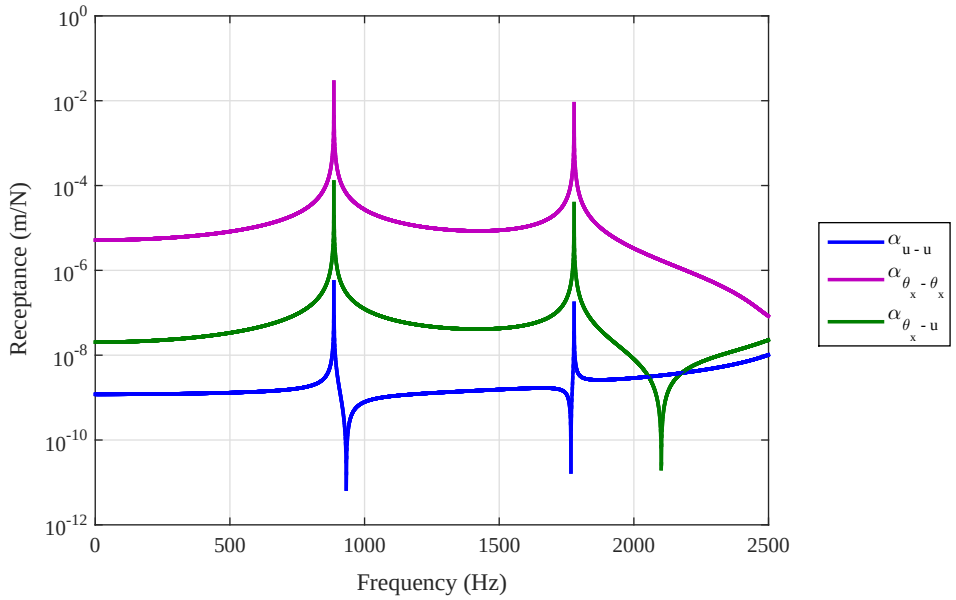

Figure 4.8. Stretching-twisting coupling effect

To illustrate the stretching-twisting coupling effect, a stacking sequence which consists of one single layer $[\alpha]$ is considered now. Figures 4.9 and 4.10 give the frequency response function of transfer receptance type for different fibre angles of composite material: $60°$, $90°$ and $180°$.

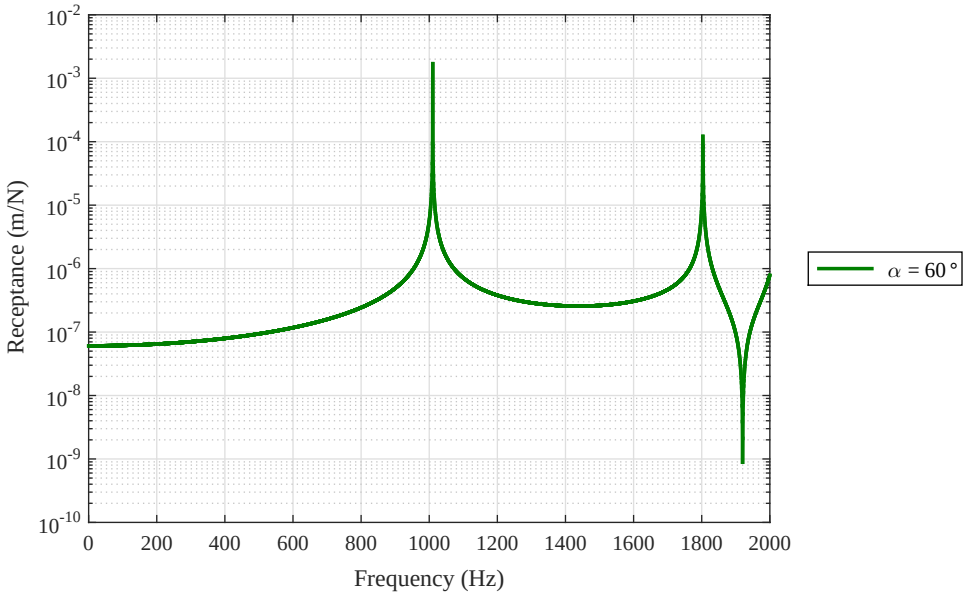

Figure 4.9. Stretching-twisting coupling effect, case: $60°$ fibre angle

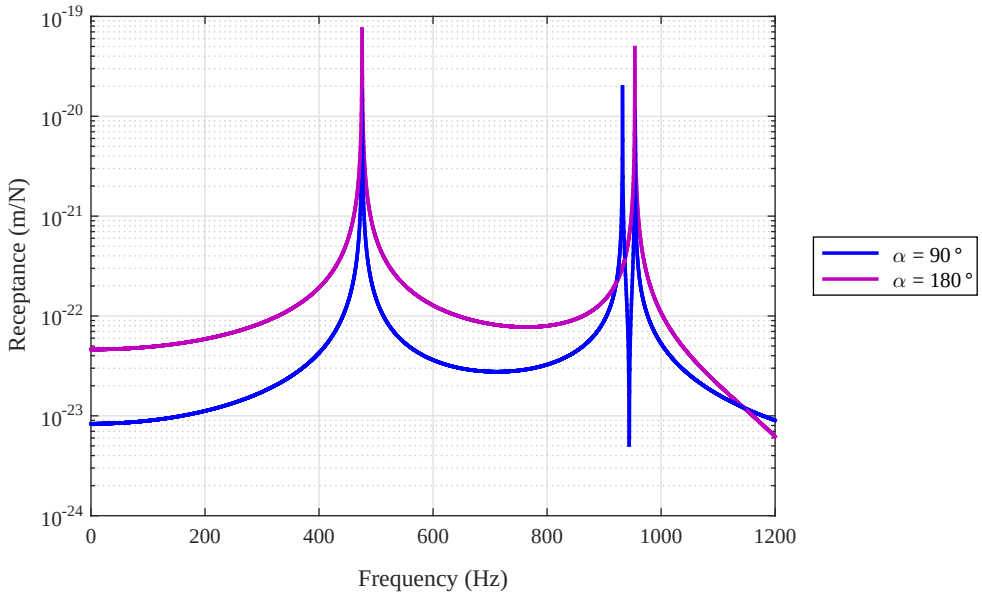

Figure 4.10. Stretching-twisting coupling effect, case: $90°$ and $180°$ fibre angles

It can be observed from figure 4.9 that for $60°$ fiber orientation angle, the stretching-twisting coupling effect is present. While it can be observed from figure 4.10 that for $90°$ and $180°$ fiber orientation angles, the stretching-twisting coupling effect can be neglected and assumed not present as for $0°$ fiber orientation angle. It can be noticed that this results are true for the case of non rotating and rotating shaft and this can be explained as we said in above that the gyroscopic effect is not present in the stretching and twisting behaviours.

4.11 Conclusion

The analysis of free vibration and frequency response of rotating composite shafts using Modified Equivalent Single Layer Theory is presented in this chapter. Several examples have been processed to validate this theory and to determine the influence of different mechanical coupling on rotating composite shafts dynamic behaviour. In fact, results have allowed us to conclude that mechanical couplings such as the bending-bending, shear-bending and the stretching-twisting are influenced by changing stacking sequences, number of layers, fiber orientations and rotational speeds. Therefore, the stacking sequence and the fiber orientation are considered as optimization parameters for the dynamic behaviour of rotating composite shafts.

In some practical shaft configurations, different layers may be made of materials with quite different mechanical properties. Thus, the development of Layerwise Shaft Theory based on layerwise displacement will give more accurate results than ESLT and Modified ESLT.

Chapter 5

New Finite Element Formulation Based on Layerwise Shaft Theory

5.1 Introduction

A literature review, as presented in section 1.4, shows that finite element formulations based on layerwise theory are expected to yield more accurate results because of more realistic displacement field and reveals that a development is needed for layerwise theory since layerwise theories available in the literature are reduced from shell theory and not based on shaft theory. One of the application field of Layerwise Shaft Theory (LST), developed in this work, is modeling the composite shaft, the functionally graded material shaft and the viscoelastic damping treatments. In fact, in those practical shaft configurations, different layers may consist of different materials. So, different laminate may have different slopes. Therefore, layerwise displacement field becomes more meaningful in those composite shaft applications.

In this chapter, LST is developed based on shaft finite element theory unlike Layerwise Beam Theory (LBT) available in the literature which are reduced from shell finite element theory. The layerwise character of the composite shaft is conserved. The composite shaft wall thickness is made up of several layers with different individual thicknesses and fiber orientations. LST is based on unique displacement field for each layer and may enforce the interlaminar continuity of transverse shear stresses using the post processing procedure. The cross section of each layer remains straight which implies linear variation of displacement across the layer thickness. There is continuity of displacement due to perfect bonded assumed between layers at the interface of two plies. During deflection, there is no distortion of the shaft cross section to retain a beam like character of the shaft. Thus, a transverse deflection of shaft cross section, due to shaft bending, can also be represented by two components in cylindrical coordinate system: in-plane displacement (circumferential direction) and normal displacement (through the thickness direction). The displacement in axial direction is due to rotation of cross section about a diametral axis. Strain field is obtained by using this displacement field in strain displacement relations for a cylindrical coordinate system. Then, the expressions of composite shaft deformation energy and composite shaft kinetic energy are setup by integrating over the cross sectional area by summing up the contribution of each orthotropic layer. Next, equations of motion are obtained using Hamilton's principle which are solved for general composite rotor dynamic problem. The conventional rotor dynamic characteristics such as: natural frequencies, critical speeds were analysed and results from LST formulation were compared with those available in the literature in order to validate and illustrate the new finite element based on layerwise and shaft theories developed in this work.

5.2 Displacement field

The laminated composite shaft consists of P orthotropic layers as shown in figure 5.1. The modeling of the laminated composite shaft using Layerwise Shaft Theory (LST), developed in this work, is based on the following assumptions:

- Material of each layer is linearly elastic and has two planes of material symmetry (orthotropic);
- Each layer is of uniform thickness;
- Layers are perfectly bonded together at each interface;
- The displacement continuity at each interface is maintained.

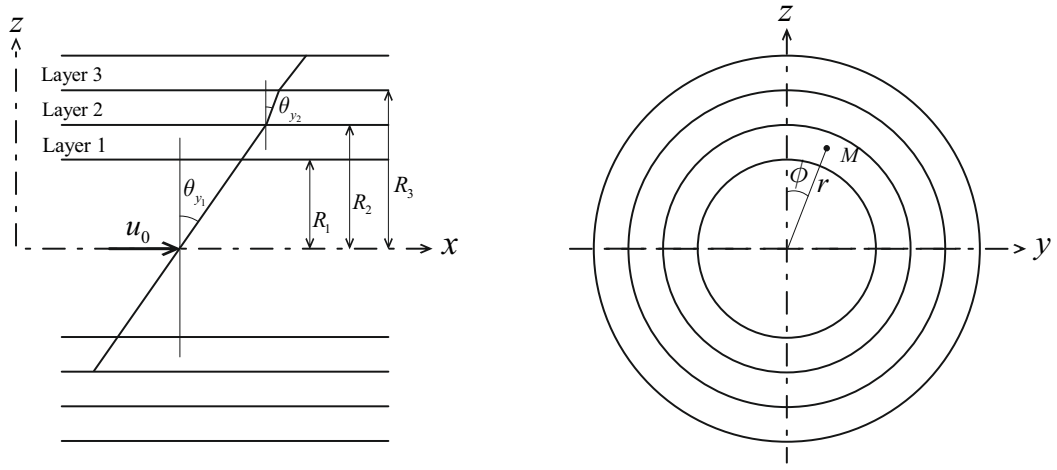

Figure 5.1. Layerwise model

By choosing the coordinate axis x to coincide with the shaft axis, the continuous displacement field of the kth layer of a composite shaft, with $k \in [1 \dots P]$, is described as follows:

$$\{U(x,y,z,t)\}_k = \begin{Bmatrix} u_x(x,y,z,t) \\ u_y(x,y,z,t) \\ u_z(x,y,z,t) \end{Bmatrix} = \begin{Bmatrix} u_k(x,y,z,t) \\ v(x,t) \\ w(x,t) \end{Bmatrix} \tag{5.1}$$

where $v(x,t)$ and $w(x,t)$ are the transverse displacements of any point of all the layers ($k \in [1 \dots P]$) along y and z directions respectively and $u_k(x,y,z,t)$ is the displacement of any generic point of the kth layer cross section along x direction. Denoting $\theta_{y_k}(x,t)$ and $\theta_{z_k}(x,t)$ as the rotations about y and z axis respectively of the kth layer where ($k \in [1 \dots P]$), (r,ϕ) as the coordinates of any point M belonging to the kth layer in the cylindrical coordinate system and $u_0(x,t)$ as the reference axial displacement of the shaft axis, accordingly with figure 5.1, $u_k(x,y,z,t)$ is expressed as follows:

- for the first layer: $k = 1$

$$u_1(x,y,z,t) = u_0(x,t) + r\sin(\phi)\,\theta_{y_1} - r\cos(\phi)\,\theta_{z_1} \tag{5.2}$$

- and for $k \in [2 \dots P]$

$$u_k(x,y,z,t) = u_0(x,t) + \sum_{j=1}^{k-1} h_j \sin(\phi)\,\theta_{y_j} - \sum_{j=1}^{k-1} h_j \cos(\phi)\,\theta_{z_j} + (r-h_k)\sin(\phi)\,\theta_{y_k} - (r-h_k)\cos(\phi)\,\theta_{z_k} \tag{5.3}$$

with $h_k = R_k - R_1$ and the jth layer thickness is defined as:

$$h_j = R_{j+1} - R_j \tag{5.4}$$

where R_{j+1} and R_j represent the outer and the inner radius of the jth layer respectively, with $j \in [1 \dots (k-1)]$, as shown in figure 5.2.

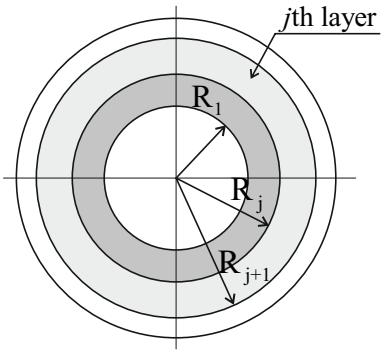

Figure 5.2. Inner and outer radius of the jth layer of the composite shaft

It can be noticed from the displacement field expressions (5.2) and (5.3) that the displacement continuity is verified at each interface. The practical result is that the displacement field of each layer $k \in [2 \dots P]$ is coupled to the displacement field of the first layer $k = 1$.

The displacement field $\{U\}_k$, given by expression (5.1), can be represented through a set of generalized variables as:

$$\{U\}_k = [\mathcal{N}]_k \{d\} \tag{5.5}$$

where

$$\{d\} = \left\{ u \quad v \quad w \quad \theta_{y_1} \quad \theta_{z_1} \quad \dots \quad \theta_{y_k} \quad \theta_{z_k} \quad \dots \quad \theta_{y_P} \quad \theta_{z_P} \right\}^{\mathrm{T}} \tag{5.6}$$

represents the generalized displacement field and matrix $[\mathcal{N}]_k$ is defined as follows:

- for the first layer: $k = 1$

$$[\mathcal{N}]_1 = \begin{bmatrix} 1 & 0 & 0 & r\sin\phi & -r\cos\phi \\ 0 & 1 & 0 & 0 & 0 \\ 0 & 0 & 1 & 0 & 0 \end{bmatrix} \tag{5.7}$$

- and for $k \in [2 \dots P]$

$$[\mathcal{N}]_k = \begin{bmatrix} 1 & 0 & 0 & h_1\sin\phi & -h_1\cos\phi & \dots & h_{k-1}\sin\phi & -h_{k-1}\cos\phi & (r-h_k)\sin\phi & -(r-h_k)\cos\phi \\ 0 & 1 & 0 & 0 & 0 & \dots & 0 & 0 & 0 & 0 \\ 0 & 0 & 1 & 0 & 0 & \dots & 0 & 0 & 0 & 0 \end{bmatrix} \tag{5.8}$$

5.3 Strain field

The kth layer strain field in the cartesian coordinate system is given as:

$$\{\varepsilon\}_k = \begin{Bmatrix} \varepsilon_{xx_k} \\ \gamma_{xy_k} \\ \gamma_{xz_k} \end{Bmatrix} \tag{5.9}$$

which can be expressed from the displacement field expression (5.1) and equations (5.2) and (5.3), where the stretching-bending relation is expressed as follows:

- for the first layer: $k = 1$

$$\varepsilon_{xx_1} = \frac{\partial u_0}{\partial x} + r\sin\phi\frac{\partial \theta_{y_1}}{\partial x} - r\cos\phi\frac{\partial \theta_{z_1}}{\partial x} \tag{5.10}$$

- and for $k \in [2 \dots P]$

$$\varepsilon_{xx_k} = \frac{\partial u_0}{\partial x} + \sum_{j=1}^{k-1} h_j \sin\phi\frac{\partial \theta_{y_j}}{\partial x} - \sum_{j=1}^{k-1} h_j \cos\phi\frac{\partial \theta_{z_j}}{\partial x} + (r-h_k)\sin\phi\frac{\partial \theta_{y_k}}{\partial x} - (r-h_k)\cos\phi\frac{\partial \theta_{z_k}}{\partial x} \tag{5.11}$$

and the shear-strain relation of the kth layer, where $k \in [1 \dots P]$, is expressed as:

$$\begin{cases} \gamma_{xy_k} = -\theta_{z_k} + \dfrac{\partial v}{\partial x} \\ \gamma_{xz_k} = \theta_{y_k} + \dfrac{\partial w}{\partial x} \end{cases} \tag{5.12}$$

Since the shape of the shaft cross section is assumed circular, it is more convenient to express the stress strain relations in the cylindrical coordinate system (x, r, ϕ). Using equation (3.11) and the strain field expression, given in equation (5.9), the strain components in the cylindrical coordinate system (x, r, ϕ) of the kth layer can be expressed as follows:

$$\begin{cases} \{\varepsilon\}_{xx_k} = \{\varepsilon\}_{xx_k} \\ \{\gamma\}_{x\phi_k} = \begin{bmatrix} -\sin\phi & \cos\phi \end{bmatrix} \begin{Bmatrix} \gamma_{xy_k} \\ \gamma_{xz_k} \end{Bmatrix} \\ \{\gamma\}_{xr_k} = \begin{bmatrix} \cos\phi & \sin\phi \end{bmatrix} \begin{Bmatrix} \gamma_{xy_k} \\ \gamma_{xz_k} \end{Bmatrix} \end{cases} \tag{5.13}$$

which can be rewritten in the matrix form as:

$$\begin{cases} \{\varepsilon\}_{xx_k} = [\mathcal{B}]_k^{\varepsilon} \{d\} \\ \{\gamma\}_{x\phi_k} = [\mathcal{B}]_k^{\gamma_\phi} \{d\} \\ \{\gamma\}_{xr_k} = [\mathcal{B}]_k^{\gamma_r} \{d\} \end{cases} \tag{5.14}$$

where $[\mathcal{B}]_k^{\varepsilon}$ is the stretching-bending matrix and $[\mathcal{B}]_k^{\gamma_\phi}$ and $[\mathcal{B}]_k^{\gamma_r}$ are the transverse shear deformation matrices of the kth layer, where $k \in [1 \dots P]$.

The stretching-bending matrix $[\mathcal{B}]_k^{\varepsilon}$ can be defined as follows:

- for the first layer: $k = 1$

$$[\mathcal{B}]_1^{\varepsilon} = [\mathcal{Z}]_1^{\varepsilon} \{\hat{\mathcal{B}}\}_1^{\varepsilon} \tag{5.15}$$

where

$$\begin{aligned} [\mathcal{Z}]_1^{\varepsilon} &= \begin{bmatrix} 1 & 0 & 0 & r\sin\phi & -r\cos\phi \end{bmatrix} \\ \{\hat{\mathcal{B}}\}_1^{\varepsilon} &= \begin{Bmatrix} \frac{\partial}{\partial x} & 0 & 0 & \frac{\partial}{\partial x} & \frac{\partial}{\partial x} \end{Bmatrix}^{\mathrm{T}} \end{aligned} \tag{5.16}$$

- and for $k \in [2 \dots P]$

$$[\mathcal{B}]_k^{\varepsilon} = [\mathcal{Z}]_k^{\varepsilon} \{\hat{\mathcal{B}}\}_k^{\varepsilon} \tag{5.17}$$

where

$$\begin{aligned} [\mathcal{Z}]_k^{\varepsilon} &= \begin{bmatrix} 1 & 0 & 0 & h_1\sin\phi & -h_1\cos\phi & \dots & h_{k-1}\sin\phi & -h_{k-1}\cos\phi & (r-h_k)\sin\phi & -(r-h_k)\cos\phi \end{bmatrix} \\ \{\hat{\mathcal{B}}\}_k^{\varepsilon} &= \begin{Bmatrix} \frac{\partial}{\partial x} & 0 & 0 & \frac{\partial}{\partial x} & \frac{\partial}{\partial x} & \dots & \frac{\partial}{\partial x} & \frac{\partial}{\partial x} & \frac{\partial}{\partial x} & \frac{\partial}{\partial x} \end{Bmatrix}^{\mathrm{T}} \end{aligned} \tag{5.18}$$

The transverse shear deformation matrices $[\mathcal{B}]_k^{\gamma_\phi}$ and $[\mathcal{B}]_k^{\gamma_r}$ are defined as:

$$\begin{cases} [\mathcal{B}]_k^{\gamma_\phi} = [\mathcal{Z}]_k^{\gamma_\phi} \{\hat{\mathcal{B}}\}_k^{\gamma} \\ [\mathcal{B}]_k^{\gamma_r} = [\mathcal{Z}]_k^{\gamma_r} \{\hat{\mathcal{B}}\}_k^{\gamma} \end{cases} \tag{5.19}$$

where

$$\begin{aligned} [\mathcal{Z}]_k^{\gamma_\phi} &= \begin{bmatrix} -\sin\phi & \cos\phi \end{bmatrix} \\ [\mathcal{Z}]_k^{\gamma_r} &= \begin{bmatrix} \cos\phi & \sin\phi \end{bmatrix} \\ \{\hat{\mathcal{B}}\}_k^{\gamma} &= \begin{bmatrix} 0 & \frac{\partial}{\partial x} & 0 & 0 & 0 & \dots & 0 & 0 & 0 & -1 \\ 0 & 0 & \frac{\partial}{\partial x} & 0 & 0 & \dots & 0 & 0 & 1 & 0 \end{bmatrix} \end{aligned} \tag{5.20}$$

5.4 Stress field

The generalized Hooke's law for an orthotropic material where $[Q]$ is the material stiffness matrix is given by:

$$\{\sigma\} = [Q]\{\varepsilon\} \tag{5.21}$$

Using the same development as in section 3.2.3, we obtain the abbreviated form of the stress field expression in the cylindrical coordinate system (x, r, ϕ) as follows:

$$\{\sigma\} = \left[\bar{Q}\right]\{\varepsilon\} \tag{5.22}$$

where $\left[\bar{Q}\right]$ is the transformed material stiffness matrix of the layer which is expressed in equation (3.17).

Using the same development as in section 3.2.4, the stress strain relations for the kth layer can be expressed as:

$$\begin{cases} \sigma_{xx_k} = \bar{Q}_{11_k}\varepsilon_{xx_k} + k_s\bar{Q}_{16_k}\gamma_{x\phi_k} \\ \tau_{xr_k} = k_s\bar{Q}_{55_k}\gamma_{xr_k} \\ \tau_{x\phi_k} = k_s\bar{Q}_{16_k}\varepsilon_{xx_k} + k_s\bar{Q}_{66_k}\gamma_{x\phi_k} \end{cases} \tag{5.23}$$

where k_s is the transverse shear correction factor and $\bar{Q}_{ij_k}$ are the constitutive terms which are related to the laminate angle α and the elastic constants of principal axes of the kth layer and are defined in equations (3.23).

5.5 Deformation energy

The deformation energy is obtained from the integral evaluated over the volume domain of the whole set of P individual layers as:

$$\Pi = \sum_{k=1}^{P} \frac{1}{2} \int_{V_k} \{\varepsilon\}_k^{\mathrm{T}} \{\sigma\}_k \, \mathrm{d}V_k \tag{5.24}$$

Replacing expression (5.23) in the deformation energy expression (5.24), one gets:

$$\begin{aligned}\Pi = \sum_{k=1}^{P} \frac{1}{2} \int_{\ell} \int_{A_k} \Big(& \{\varepsilon\}_{xx_k}^{\mathrm{T}} \bar{Q}_{11_k} \{\varepsilon\}_{xx_k} + \{\varepsilon\}_{xx_k}^{\mathrm{T}} k_s \bar{Q}_{16_k} \{\gamma\}_{x\phi_k} + \{\gamma\}_{x\phi_k}^{\mathrm{T}} k_s \bar{Q}_{16_k} \{\varepsilon\}_{xx_k} \\ & + \{\gamma\}_{x\phi_k}^{\mathrm{T}} k_s \bar{Q}_{66_k} \{\gamma\}_{x\phi_k} + \{\gamma\}_{xr_k}^{\mathrm{T}} k_s \bar{Q}_{55_k} \{\gamma\}_{xr_k} \Big) \mathrm{d}A_k \mathrm{d}x \end{aligned} \tag{5.25}$$

where $\{\varepsilon\}_{xx_k}^{\mathrm{T}} k_s \bar{Q}_{16_k} \{\gamma\}_{x\phi_k}$ and $\{\gamma\}_{x\phi_k}^{\mathrm{T}} k_s \bar{Q}_{16_k} \{\varepsilon\}_{xx_k}$ account for the shear-normal coupling effect. Substituting equations (5.14) into deformation energy expression (5.25), the laminated shaft deformation energy can be written as:

$$\begin{aligned}\Pi = \sum_{k=1}^{P} \frac{1}{2} \int_{L} \int_{A_k} \Big(& \left([\mathcal{B}]_k^{\varepsilon} \{d\}\right)^{\mathrm{T}} \bar{Q}_{11_k} [\mathcal{B}]_k^{\varepsilon} + \left([\mathcal{B}]_k^{\varepsilon} \{d\}\right)^{\mathrm{T}} k_s \bar{Q}_{16_k} [\mathcal{B}]_k^{\gamma_\phi} + \left([\mathcal{B}]_k^{\gamma_\phi} \{d\}\right)^{\mathrm{T}} k_s \bar{Q}_{16_k} [\mathcal{B}]_k^{\varepsilon} \\ & + \left([\mathcal{B}]_k^{\gamma_\phi} \{d\}\right)^{\mathrm{T}} k_s \bar{Q}_{66_k} [\mathcal{B}]_k^{\gamma_\phi} + \left([\mathcal{B}]_k^{\gamma_r} \{d\}\right)^{\mathrm{T}} k_s \bar{Q}_{55_k} [\mathcal{B}]_k^{\gamma_r} \Big) \{d\} \, \mathrm{d}A_k \mathrm{d}x \end{aligned} \tag{5.26}$$

5.6 Kinetic energy

The kinetic energy of the rotating composite shaft with rotational speed Ω is obtained from the integral evaluated over the volume of the whole set of P individual layers as:

$$T = \sum_{k=1}^{P} \frac{1}{2} \int_{V_k} \left\{\dot{U}\right\}_k^{\mathrm{T}} \rho_k \left\{\dot{U}\right\}_k \mathrm{d}V_k + \sum_{k=1}^{P} \frac{1}{2} \int_{V_k} \left([\mathcal{N}]_k \{d\}\right)^{\mathrm{T}} \rho_k \Omega \begin{bmatrix} 0 & -1 \\ 1 & 0 \end{bmatrix} [\mathcal{N}]_k \left\{\dot{d}\right\} \mathrm{d}V_k \tag{5.27}$$

where $\left\{\dot{U}\right\}_k$ and ρ_k represent respectively the velocity field and the mass density of the kth layer. Substituting equation (5.5) into composite shaft kinetic energy expression (5.27) and performing the time derivative, the rotating laminated composite kinetic energy can be written as follows:

$$\begin{aligned} T = & \sum_{k=1}^{P} \frac{1}{2} \int_{L} \int_{A_k} \left\{\dot{d}\right\}^{\mathrm{T}} [\mathcal{N}]_k^{\mathrm{T}} \rho_k [\mathcal{N}]_k \left\{\dot{d}\right\} \mathrm{d}A_k \mathrm{d}x \\ & + \sum_{k=1}^{P} \frac{1}{2} \int_{L} \int_{A_k} \{d\}^{\mathrm{T}} [\mathcal{N}]_k^{\mathrm{T}} \rho_k \Omega \begin{bmatrix} 0 & -1 \\ 1 & 0 \end{bmatrix} [\mathcal{N}]_k \left\{\dot{d}\right\} \mathrm{d}A_k \mathrm{d}x \end{aligned} \tag{5.28}$$

5.7 Variational formulation

For the derivation of the variational statement equivalent of the governing differential equations, the Hamilton's Principle is herein adopted:

$$\delta \int_{t_i}^{t_f} (T - \Pi)\, \mathrm{d}t = 0 \tag{5.29}$$

Introducing kinetic energy T expression (5.28) and deformation energy Π expression (5.26) into Hamilton's principle (5.29) and performing the variation and an integration by parts, and since the above stated Hamilton's principle must be verified for an arbitrary $\{\delta d\}$, the variational statement can be expressed as:

$$\begin{aligned}
&\sum_{k=1}^{P} \int_L \int_{A_k} \left([\mathcal{N}]_k \{\delta d\} \right)^{\mathrm{T}} \rho_k [\mathcal{N}]_k \{\ddot{d}\} \mathrm{d}A_k \mathrm{d}x + \sum_{k=1}^{P} \int_L \int_{A_k} \left([\mathcal{N}]_k \{\delta d\} \right)^{\mathrm{T}} \rho_k \Omega \begin{bmatrix} 0 & -1 \\ 1 & 0 \end{bmatrix} [\mathcal{N}]_k \{\dot{d}\} \mathrm{d}A_k \mathrm{d}x \\
&+ \sum_{k=1}^{P} \int_L \int_{A_k} \Big(\left([\mathcal{B}]_k^{\varepsilon} \{\delta d\} \right)^{\mathrm{T}} \bar{Q}_{11_k} [\mathcal{B}]_k^{\varepsilon} + \left([\mathcal{B}]_k^{\varepsilon} \{\delta d\} \right)^{\mathrm{T}} k_s \bar{Q}_{16_k} [\mathcal{B}]_k^{\gamma_\phi} + \left([\mathcal{B}]_k^{\gamma_\phi} \{\delta d\} \right)^{\mathrm{T}} k_s \bar{Q}_{16_k} [\mathcal{B}]_k^{\varepsilon} \\
&+ \left([\mathcal{B}]_k^{\gamma_\phi} \{\delta d\} \right)^{\mathrm{T}} k_s \bar{Q}_{66_k} [\mathcal{B}]_k^{\gamma_\phi} + \left([\mathcal{B}]_k^{\gamma_r} \{\delta d\} \right)^{\mathrm{T}} k_s \bar{Q}_{55_k} [\mathcal{B}]_k^{\gamma_r} \Big) \{d\}\, \mathrm{d}A_k \mathrm{d}x = 0 \qquad \forall\ \{\delta d\}
\end{aligned} \tag{5.30}$$

5.8 Finite element definition

The developed finite element has two nodes as shown in figure 5.3. In this case, for each node and for P layers, the element has $(3 + 2P)$ degrees of freedom: three displacements u, v, and w, P slopes about y axis and P slopes about z axis denoted respectively θ_{y_k} and θ_{z_k} for the kth layer, where $k \in [1 \dots P]$.

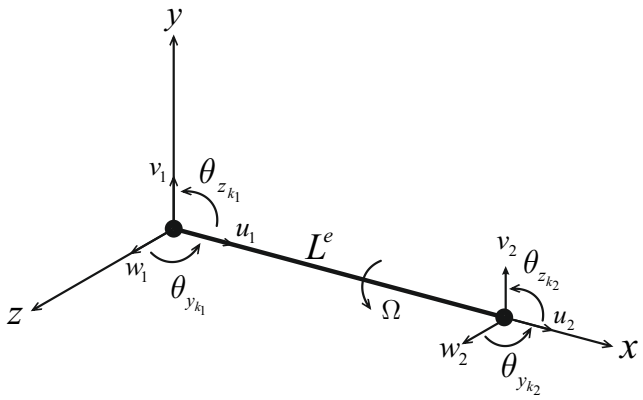

Figure 5.3. Shaft finite element for the kth layer

A natural coordinate system, where ξ coordinate is coincident with x direction, is defined in the unit finite element, in which the set of linear interpolation functions, used to interpolate the variables within the finite element domain, are defined as:

$$N_1 = \frac{1 - \xi}{2} \qquad \text{and} \qquad N_2 = \frac{1 + \xi}{2} \tag{5.31}$$

The elemental generalized displacement field $\{d^e\}$ is approximated using the set of interpolation functions, represented by the shape functions matrix $[N]$ and the elemental vector of nodal degree of freedom $\{q^e\}$ as:

$$\{d^e\} = [N]\{q^e\} \tag{5.32}$$

5.9 Weak form finite element discretization

The global weak form described in equation (5.30) can be expressed as the sum of the elemental forms leading to the definition of the elemental matrices. Adding the contribution of all the E finite elements, the global form can be expressed as:

$$\begin{aligned}\sum_{e=1}^{E}\Bigg(&\sum_{k=1}^{P}\int_{L^e}\int_{A_k^e}\{\delta d^e\}^{\mathrm{T}}[\mathcal{N}]_k^{\mathrm{T}}\rho_k[\mathcal{N}]_k\{\ddot{d}^e\}\mathrm{d}A_k^e\mathrm{d}x^e+\sum_{k=1}^{P}\int_{L^e}\int_{A_k^e}\{\delta d^e\}^{\mathrm{T}}[\mathcal{N}]_k^{\mathrm{T}}\rho_k\Omega\begin{bmatrix}0&-1\\1&0\end{bmatrix}[\mathcal{N}]_k\{\dot{d}^e\}\mathrm{d}A_k^e\mathrm{d}x^e\\&+\sum_{k=1}^{P}\int_{L^e}\int_{A_k^e}\Big(\left([\mathcal{B}]_k^{\varepsilon}\{\delta d^e\}\right)^{\mathrm{T}}\bar{Q}_{11_k}[\mathcal{B}]_k^{\varepsilon}+\left([\mathcal{B}]_k^{\varepsilon}\{\delta d^e\}\right)^{\mathrm{T}}k_s\bar{Q}_{16_k}[\mathcal{B}]_k^{\gamma_\phi}+\left([\mathcal{B}]_k^{\gamma_\phi}\{\delta d^e\}\right)^{\mathrm{T}}k_s\bar{Q}_{16_k}[\mathcal{B}]_k^{\varepsilon}\\&+\left([\mathcal{B}]_k^{\gamma_\phi}\{\delta d^e\}\right)^{\mathrm{T}}k_s\bar{Q}_{66_k}[\mathcal{B}]_k^{\gamma_\phi}+\left([\mathcal{B}]_k^{\gamma_r}\{\delta d^e\}\right)^{\mathrm{T}}k_s\bar{Q}_{55_k}[\mathcal{B}]_k^{\gamma_r}\Big)\{d^e\}\,\mathrm{d}A_k^e\mathrm{d}x^e\Bigg)=0\end{aligned} \tag{5.33}$$

where the generalized variables $\{d^e\}$ are restricted to the domain of integration L^e and an approximation is considered at a local level in each finite element as stated in equation (5.32).

The relation between the elemental degrees of freedom and the global ones is established through the connectivity matrices $[R^e]$, expressed as:

$$\{q^e\} = [R^e]\{q\} \tag{5.34}$$

where $\{q\}$ represents the vector of global degrees of freedom.

Substituting equation (5.32) into global form expression (5.33), yields:

$$\sum_{e=1}^{E}\Big(\{\delta q^e\}^{\mathrm{T}}[M^e]\{\ddot{q}^e\}+\{\delta q^e\}^{\mathrm{T}}[G^e(\Omega)]\{\dot{q}^e\}+\{\delta q^e\}^{\mathrm{T}}[K^e]\{q^e\}\Big)=0 \tag{5.35}$$

where $[M^e]$ is the elementary mass matrix, $[G^e(\Omega)]$ is the elementary gyroscopic matrix which is rotational speed Ω dependent and $[K^e]$ is the elementary stiffness matrix.

The elementary mass matrix $[M^e]$ is given by:

$$[M^e]=\sum_{k=1}^{P}[M^e]_k=\sum_{k=1}^{P}\int_{L^e}[N]_k^{\mathrm{T}}[J]_k[N]_k\,\mathrm{d}x^e \tag{5.36}$$

where $[J]_k$ is the inertia matrix, expressed as:

$$[J]_k=\int_{A_k^e}[\mathcal{N}]_k^{\mathrm{T}}\rho_k[\mathcal{N}]_k\,\mathrm{d}A_k^e \tag{5.37}$$

The elementary gyroscopic matrix $[G^e(\Omega)]$ is given by:

$$[G^e(\Omega)]=\sum_{k=1}^{P}[G^e(\Omega)]_k=\sum_{k=1}^{P}\int_{L^e}[N]_k^{\mathrm{T}}[H(\Omega)]_k[N]_k\,\mathrm{d}x^e \tag{5.38}$$

where $[H(\Omega)]_k$ is the gyroscopic inertia matrix which depends on the rotational speed Ω, given as:

$$[H(\Omega)]_k = \int_{A_k^e} [\mathcal{N}]_k^{\mathrm{T}} \rho_k \Omega \begin{bmatrix} 0 & -1 \\ 1 & 0 \end{bmatrix} [\mathcal{N}]_k \, \mathrm{d}A_k^e \tag{5.39}$$

The elementary stiffness matrix $[K^e]$ is given by:

$$[K^e] = \sum_{k=1}^{P} [K^e]_k = \sum_{k=1}^{P} \int_{L^e} \Big([B]_k^{\varepsilon^{\mathrm{T}}} D_{11_k} [B]_k^{\varepsilon} + [B]_k^{\varepsilon^{\mathrm{T}}} D_{16_k} [B]_k^{\gamma_\phi} + [B]_k^{\gamma_\phi^{\mathrm{T}}} \hat{D}_{16_k} [B]_k^{\varepsilon} + [B]_k^{\gamma_\phi^{\mathrm{T}}} D_{66_k} [B]_k^{\gamma_\phi} + [B]_k^{\gamma_r^{\mathrm{T}}} D_{55_k} [B]_k^{\gamma_r} \Big) \mathrm{d}x^e \tag{5.40}$$

where $[B]_k^{\varepsilon}$, $[B]_k^{\gamma_\phi}$ and $[B]_k^{\gamma_r}$ are the deformation matrices of the kth layer of the finite element, defined as:

$$\begin{cases} [B]_k^{\varepsilon} = \left[\hat{\mathcal{B}}\right]_k^{\varepsilon} [N] \\ [B]_k^{\gamma_\phi} = \left[\hat{\mathcal{B}}\right]_k^{\gamma_r} [N] \\ [B]_k^{\gamma_r} = \left[\hat{\mathcal{B}}\right]_k^{\gamma_r} [N] \end{cases} \tag{5.41}$$

and the terms D_{ij} are defined as:

$$\begin{cases} D_{11_k} = \displaystyle\int_{A_k^e} [\mathcal{Z}]_k^{\varepsilon^{\mathrm{T}}} \bar{Q}_{11_k} [\mathcal{Z}]_k^{\varepsilon} \, \mathrm{d}A_k^e \\ D_{16_k} = \displaystyle\int_{A_k^e} [\mathcal{Z}]_k^{\varepsilon^{\mathrm{T}}} k_s \bar{Q}_{16_k} [\mathcal{Z}]_k^{\gamma_\phi} \, \mathrm{d}A_k^e \\ \hat{D}_{16_k} = D_{16_k}^{\mathrm{T}} = \displaystyle\int_{A_k^e} [\mathcal{Z}]_k^{\gamma_\phi^{\mathrm{T}}} k_s \bar{Q}_{16_k} [\mathcal{Z}]_k^{\varepsilon} \, \mathrm{d}A_k^e \\ D_{66_k} = \displaystyle\int_{A_k^e} [\mathcal{Z}]_k^{\gamma_\phi^{\mathrm{T}}} k_s \bar{Q}_{66_k} [\mathcal{Z}]_k^{\gamma_\phi} \, \mathrm{d}A_k^e \\ D_{55_k} = \displaystyle\int_{A_k^e} [\mathcal{Z}]_k^{\gamma_r^{\mathrm{T}}} k_s \bar{Q}_{55_k} [\mathcal{Z}]_k^{\gamma_r} \, \mathrm{d}A_k^e \end{cases} \tag{5.42}$$

The elementary mass, gyroscopic and stiffness matrices are thus obtained as the sum of the corresponding individual matrices of each layer.

One of the application field of the Layerwise Shaft Theory (LST) is modeling the composite shaft, the functionally graded material shaft and the viscoelastic damping treatments. Since, in those practical shaft configurations, different layers may consist of materials with quite different mechanical properties.

5.10 Composite shaft application

5.10.1 Fiber orientation effect

For purpose of validation of the developed Layerwise Shaft Theory (LST), a simply supported composite shaft made of one single layer $[\alpha]$ is considered. The geometrical and material properties of the composite shaft are:

- $L = 1$ m, mean radius $= R_m = 0.05$ m, wall thickness $= h = 4 \times 10^{-3}$ m;

- $E_1 = 130$ GPa, $E_2 = 10$ GPa, $G_{ij} = 7$ GPa, $\nu_{12} = 0.25$, $\rho = 1500$ kg/m^3;
- Shear correction factor: $k_s = 1/2$.

The finite element model data are given as:

- Number of degrees of freedom $= 5$;
- Number of elements $= 20$.

In order to have a basis for comparison, the shear-normal coupling effects are ignored. Table 5.1 shows a comparison of the natural frequencies obtained using the developed LST and the available LBT developed by [Singh and Gupta, 1996a] and LBT developed by [Gubran and Gupta, 2005] excluding shear-normal coupling effects. Percentages shown in table 5.1 are those of the comparison between LST and LBT developed by [Gubran and Gupta, 2005].

Table 5.1. Comparison of natural frequencies (Hz) obtained by different formulations

α	LBT[1]		LBT[2]			LST		
	1st	2nd	1st	2nd	3rd	1st	2nd	3rd
0°	427.63	1226	428.04	1227.72	2056.44	428.89	1234.94	2079.08
						0.2%	0.6%	1.1%
15°	442.13	1431.4	442.50	1432.92	2576.95	431.83	1349.84	2377.92
						2.4%	5.8%	7.7%
30°	390.22	1409.4	390.52	1410.59	2787.43	384.13	1341.71	2571.78
						1.6%	4.9%	7.7%
45°	292.52	1108.8	292.75	1105.74	2297.63	290.75	1081.07	2209.27
						0.7%	2.2%	3.8%
60°	199.84	767.06	199.99	767.66	1627.53	199.56	762.368	1609.35
						0.2%	0.7%	1.1%
75°	150.66	576.65	150.77	577.09	1219.06	150.74	577.089	1221.48
						0.02%	0%	0.2%
90°	140.46	528.16	140.57	528.59	1092.06	140.98	534.41	1117.32
						0.3%	1.1%	2.31%

[1] [Singh and Gupta, 1996a].
[2] [Gubran and Gupta, 2005].

Results show a good agreement of natural frequencies obtained from different theories for composite shaft with one single layer with fibre orientation angle varying from $0°$ to $90°$. Natural frequencies of the first three bending modes increase when the value of the fiber orientation increases from $0°$ to $15°$ and decrease when the value of the fiber orientation increases from $15°$ to $90°$. Such behaviour is due to the neglect of the sher-normal coupling effects.

5.10.2 Shear-normal coupling effect

To illustrate the influence of the shear-normal coupling effects, natural frequencies obtained using LST excluding shear-normal coupling effects are compared with those obtained using LST including

shear-normal coupling effects as shown in table 5.2. Percentages shown in table 5.2 are those of the comparison between results obtained using LST including shear-normal coupling effects and those excluding shear-normal coupling effects.

Table 5.2. Shear-normal coupling effects on natural frequencies (Hz)

Angle	LST excluding shear-normal			LST including shear-normal		
	1st	2nd	3rd	1st	2nd	3rd
0°	428.89	1234.94	2079.08	428.89	1234.94	2079.08
				0%	0%	0%
15°	431.83	1349.84	2377.92	397.39	1259.10	2237.20
				8%	6.7%	5.9%
30°	384.13	1341.71	2571.78	329.72	1165.37	2267.72
				14.2%	13.1%	11.8%
45°	290.75	1081.07	2209.27	250.55	936.74	1931.01
				13.8%	13.3%	12.6%
60°	199.56	762.37	1609.35	183.63	702.79	1488.11
				8%	7.8%	7.5%
75°	150.74	577.09	1221.48	148.86	570.03	1207.12
				1.2%	1.2%	1.2%
90°	140.98	534.41	1117.32	140.98	534.41	1117.32
				0%	0%	0%

As expected, it can be observed from table 5.2 that natural frequencies of the first three bending modes obtained using LST including shear-normal coupling effects decrease when the value of the fiber orientation increases from 0° to 90°. In fact, the layer with 0° fiber orientation has the largest longitudinal modulus, consequently, it has the highest natural frequencies. It can be observed from the given percentages that for 0° and 90° fiber orientation angles, the shear-normal coupling has no influence on natural frequencies and that the highest percentages of difference in natural frequencies are those for 30° and 45° fiber orientation. This behaviour can be explained as under.

Figure 5.4 shows the variation of the shear-normal coupling term for different fiber orientations.

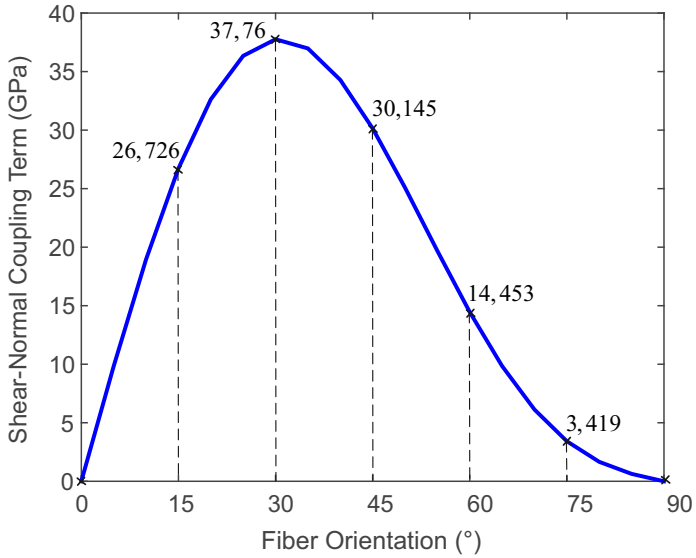

Figure 5.4. Shear-normal coupling term for different fiber orientations

It can be observed from figure 5.4 that for $0°$ and $90°$, the shear-normal coupling term is equal to zero. In this case, the shear-normal coupling effect can be neglected. While, for other fiber orientations, the shear-normal coupling term is different from zero and presents the highest values for $[15° - 45°]$ fiber orientation angle range. It can be concluded that the shear-normal coupling effect should not be neglected for the fiber orientations different from $0°$ and $90°$.

Figure 5.5 shows a comparison between $\bar{Q}_{11}$ term and shear-normal coupling term for different fiber orientations.

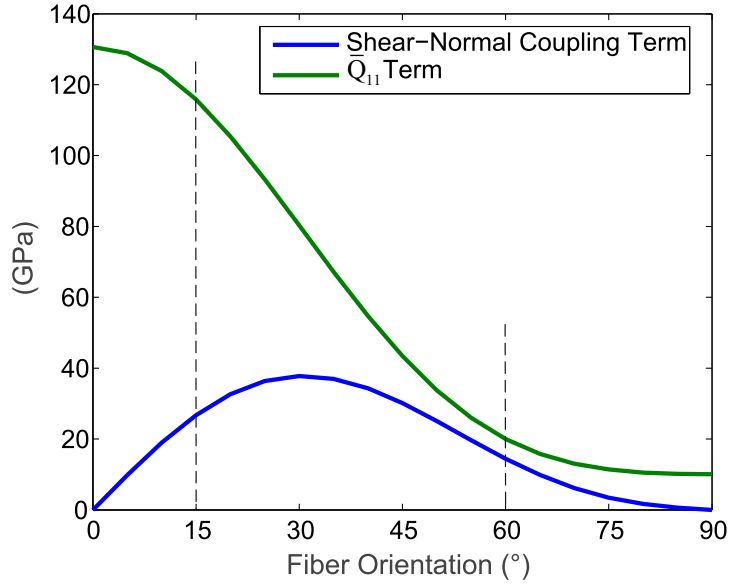

Figure 5.5. Comparison between $\bar{Q}_{11}$ term and shear-normal coupling term

This comparison confirms what was concluded above. In fact, it can be observed from Figure 5.5 that,

especially for the region where the fiber orientation is between $15°$ and $60°$, the shear-normal coupling effect is more significant. Actually, for $60° \pm 5°$, shear-normal coupling term values and $\bar{Q}_{11}$ values have a slight difference.

Figure 5.6 shows the variation of the first critical speed for different fiber orientations.

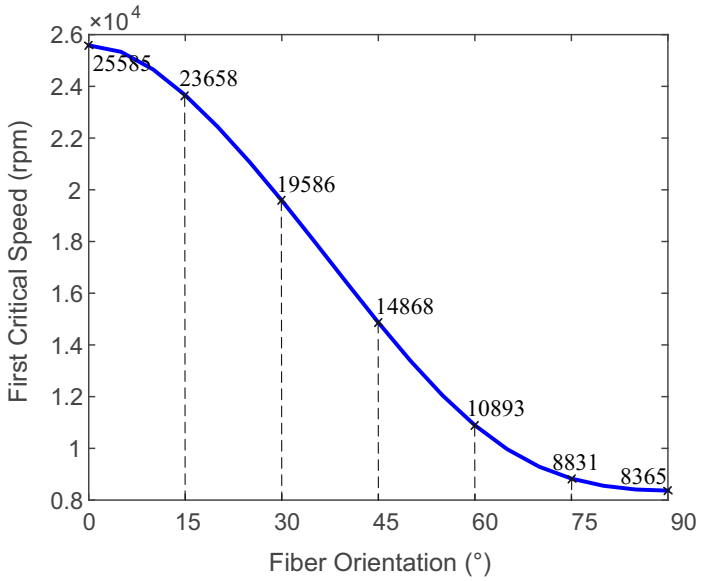

Figure 5.6. First critical speed for different fiber orientations.

Variation of 67% for the first critical speed is obtained when comparing $90°$ fiber orientation to $0°$ fiber orientation. It can be concluded that fiber orientation has a significant influence on the dynamic analysis of rotating composite shaft.

5.10.3 Stacking sequence effect

In the second case study of validation, the composite shaft is made of 10 layers of equal thickness. The geometrical and material properties of the composite shaft are:

- $L = 2.47$ m, mean radius $= R_m = 0.0635$ m, wall thickness $= h = 0.132 \times 10^{-3}$ m;
- $E_1 = 211$ GPa, $E_2 = 24.1$ GPa, $G_{ij} = 6.9$ GPa, $\nu_{12} = 0.36$, $\rho = 1965$ kg/m^3;
- 10 layers of equal thickness from the inner layer $[90°, 45°, -45°, [0°]_6, 90°]$;
- Shear correction factor: $k_s = 1/2$.

The finite element model data are given as:

- Number of degrees of freedom $= 23$;
- Number of elements $= 20$.

The first critical speed obtained from the present work using LST, excluding and including shear-normal coupling effect, is compared to those available in the literature using different theories as shown in table 5.3.

Table 5.3. Comparison of the first critical speed (rpm) obtained by different investigators

Investigator	Critical speed	Method
[Zinberg and Symonds, 1970]	5500	Experimental
	5780	EMBT
[Singh and Gupta, 1996a]	5746	EMBT
	5620	LBT
[Gubran and Gupta, 2005]	5552	Modified EMBT
	5820	LBT
[Sino et al., 2008]	5435	SHBT
Present work	5556	LST excluding shear-normal coupling
	5479	LST including shear-normal coupling

As it is shown in table 5.3, LST prediction from the present analysis is close to experimental prediction of [Zinberg and Symonds, 1970] and LBT prediction of [Singh and Gupta, 1996a]. Both LBT available in the literature are reduced from shell theory, unlike LST developed in this work which is based on beam theory. Thus, a new finite element for rotating laminated shaft based on Layerwise and beam theories including fiber orientation, stacking sequence and shear-normal coupling effects has been implemented and validated in this work.

5.11 Functionally graded material shaft application

In order to illustrate the capabilities of the developed LST finite element, the dynamical behaviour of a functionally graded material shaft is also analysed. The functionally graded material (FGM) considered is composed of two material constituents: inner and outer material as shown in figure 5.7.

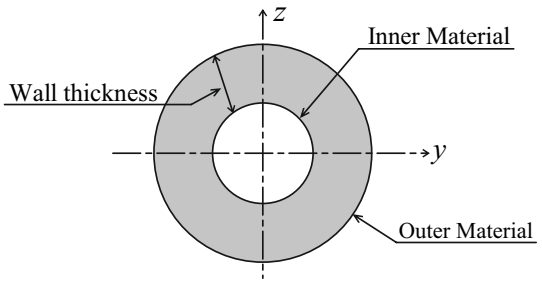

Figure 5.7. Inner and outer material of FGM shaft

For a cylindrical shaft with a uniform thickness, the material property gradation through the shaft radius is presented as [Pradhana et al., 2000]:

$$P(r) = (P_o - P_i)\left(\frac{r - R_i}{h}\right)^n + P_i \qquad r \in [R_i \;\; R_o] \tag{5.43}$$

where $P(r)$ denotes a generic material property, P_o and P_i denote respectively the property of the outer and the inner material of the shaft, n is the power law index that indicates the material variation profile

through the shaft radius $r \in [R_i \;\; R_o]$, where R_i and R_o denote respectively the inner and the outer radius of the shaft and h is the wall thickness of the shaft as shown in figure 5.7. This study assumes that Young's modulus E, Poisson's coefficient ν and mass density ρ vary according to the gradation relation (5.43):

$$\begin{cases} E(r) = (E_o - E_i)\left(\dfrac{r - R_i}{h}\right)^n + E_i \\ \nu(r) = (\nu_o - \nu_i)\left(\dfrac{r - R_i}{h}\right)^n + \nu_i \\ \rho(r) = (\rho_o - \rho_i)\left(\dfrac{r - R_i}{h}\right)^n + \rho_i \end{cases} \tag{5.44}$$

The constituent material properties considered in this analysis are given in table 5.4.

Table 5.4. Functionally graded material properties at temperature $T = 300$ K [Boukhalfa, 2014]

FGM	E (Pa)	ν	ρ (kg/m^3)
Nickel	2.05098 $\times 10^{11}$	0.31	8900
Stainless Steel	2.07788 $\times 10^{11}$	0.317756	8166
Zirconia	1.68063 $\times 10^{11}$	0.297996	5700

5.11.1 Validation case study

Consider a simply supported cylindrical shaft with mean radius R_m, length L and wall thickness h. The shaft presents the following geometric properties:

- $h = 0.002$ m, $\;\; R_m/h = 500, \;\; L/R_m = 20$;
- Shear correction factor: $k_s = 1/2$.

The finite element model data are given as:

- Number of numerical layers to capture the FGM properties variation through the thickness $= 5$;
- Number of degrees of freedom $= 13$;
- Number of elements $= 50$.

In this case, the functionally graded shaft materials has Nickel on its inner surface and Stainless Steel on its outer surface. Their material properties are given in table 5.4. Figure 5.8 shows the variation of Young's modulus E, Poisson's coefficient ν and mass density ρ through the shaft radius for different power law index n. It can be shown from figure 5.8 that the material properties vary continuously from the shaft inner surface to the shaft outer surface. For $n = 0$, the material properties of the inner and outer surfaces of the shaft are those of the outer surface material which is the Stainless Steel. For different power law index $n > 0$, Young's modulus E and Poisson's coefficient ν increase through the shaft radius. However, mass density ρ decreases through the shaft radius for different power law index $n > 0$.

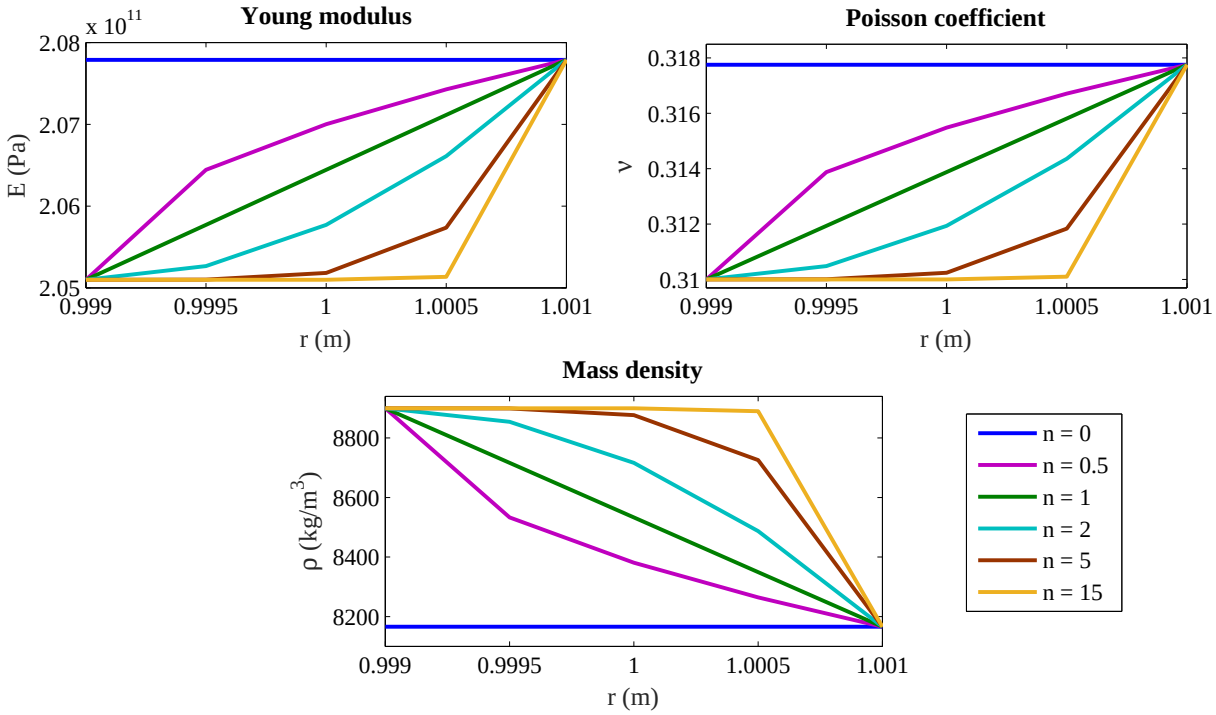

Figure 5.8. Variation of material properties through the shaft radius for different power law index n

Table 5.5 shows a comparison between the fundamental bending frequency for different power law index n obtained using Love's shell theory proposed by [Loy et al., 1999] and those obtained using Layerwise shaft theory based on beam theory proposed by the present work.

Table 5.5. Fundamental bending frequency (Hz) using different theories for different power law index n

n	Love's shell theory [Loy et al., 1999]	Layerwise shaft theory Present work	%
0	13.548	14.197	4.8%
0.5	13.321	13.910	4.4%
0.7	13.269	13.872	4.5%
1	13.211	13.827	4.7%
2	13.103	13.738	4.8%
5	12.998	13.653	5.0%
15	12.933	13.618	5.3%
30	12.914	13.616	5.4%

The percentages shown in table 5.5 are the difference in results obtained using both theories. The difference, which is around 5%, is explained by the fact that [Loy et al., 1999] used Love's shell theory based on shell theory unlike Layerwise shaft theory developed in this work which is based on beam theory. Therefore, it can be concluded that the developed Layerwise Shaft Theory (LST) based on layerwise and shaft theory can be effectively used for the dynamic analysis of functionally graded material rotating

shafts.

5.11.2 Functionally graded material type effect

A simply supported cylindrical shaft with mean radius R_m, length L and wall thickness h is considered. The shaft presents the following geometric properties:

- $h = 0.002$ m, $R_m/h = 500$, $L/R_m = 20$;
- Shear correction factor: $k_s = 1/2$.

The finite element model data are given as:

- Number of numerical layers to capture the FGM properties variation through the thickness $= 5$;
- Number of degrees of freedom $= 13$;
- Number of elements $= 20$.

Consider 4 functionally graded material types (I,II,III,IV). Properties of each constituent material are presented in table 5.4.

- Type I: Zirconia on the inner surface and Stainless Steel on the outer surface.
- Type II: Stainless Steel on the inner surface and Zirconia on the outer surface.
- Type III: Nickel on the inner surface and Stainless Steel on the outer surface.
- Type IV: Stainless Steel on the inner surface and Nickel on the outer surface.

Figure 5.9 shows the variation of the fundamental bending frequency with the power law index n for different functionally graded material shaft types.

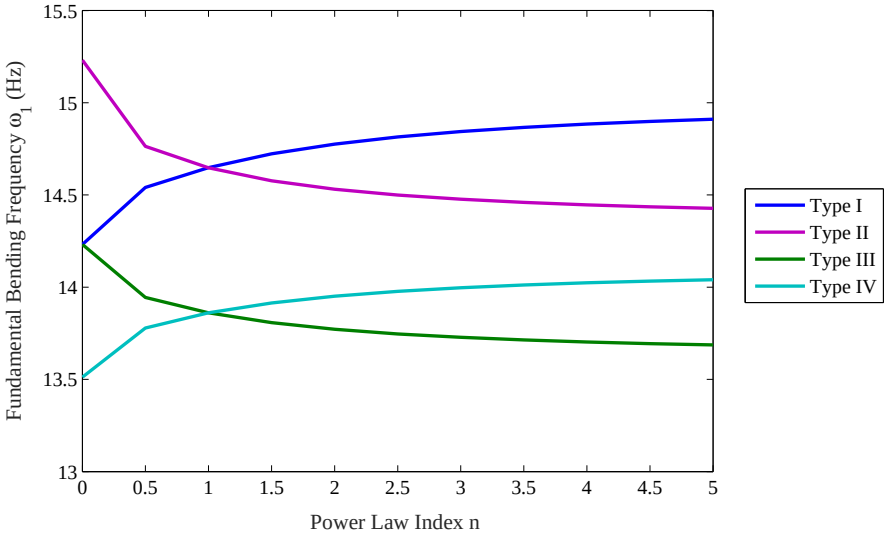

Figure 5.9. Variation of the fundamental bending frequency ω_1 with power law index n for several FGM types

The highest fundamental bending frequencies are those of type I and II where the functionally graded material is composed by Stainless Steel and Zirconia and the lowest fundamental bending frequencies are those of type III and IV where the functionally graded material is composed by Stainless Steel and Nickel. For the type I and IV, the fundamental bending frequencies increase when n increases and for the type II and III, the fundamental bending frequencies decrease when n increases. For $n = 0$, the material properties of the functionally graded material shaft are those of the outer surface material. So, in type III and IV, the fundamental bending frequencies for all value of n is between those for a Nickel and Stainless Steel shaft and in type I and II, the fundamental bending frequencies for all value of n is between those for a Stainless Steel and Zirconia shaft. For $n < 1$, the fundamental bending frequencies for type III are higher than those for type IV and the fundamental bending frequencies for type II are higher than those for type I and for $n > 1$, the fundamental bending frequencies for type IV are higher than those for type III and the fundamental bending frequencies for type I are higher than those for type II. Thus, it can be concluded that the configurations of the constituent materials affect the natural frequencies of the shaft.

A modal analysis is performed to illustrate the effect of frequencies variation associated with the first bending mode with the variation of rotational speeds. Figure 5.10 shows the Campbell diagram for forward and backward natural frequencies of the first bending mode over a rotational speed range for different FGM types where the power law index $n = 5$.

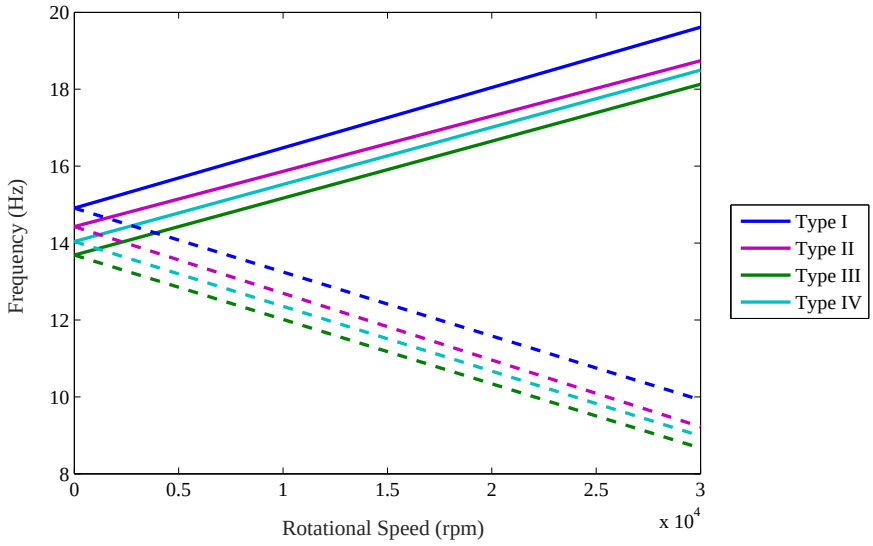

Figure 5.10. Campbell diagram for the first bending mode for several FGM types where power law index $n = 5$ (– FW, - - BW).

It can be observed from Figure 5.10 that for all FGM types, backward modes (BW) decrease with frequencies, whereas forward modes (FW) increase. It can be seen also that for the corresponding power law index $n = 5$, the highest frequencies are those for type I and the lowest frequencies are those for type III.

5.12 Viscoelastic damping treatments application

One of the application field of Layerwise Shaft Theory is modelling the viscoelastic damping treat-

ments. In this treatment, an upper layer made of high elastic modulus material can be superimposed to the low modulus viscoelastic material applied on the shaft surface as shown in figure 5.11.

In order to illustrate the capabilities of the developed LST finite element, the dynamical effects of a viscoelastic damping treatment applied on a shaft are analysed and discussed. Viscoelastic materials are known by their damping capabilities. Due to their particular molecular structure, these materials are able to dissipate deformation energy. When applied on a host structure, this is achieved because the deformation of the host structure increases internal molecular friction of the viscoelastic layer and yields energy dissipation due to the heating effect [Moreira and Rodrigues, 2006].

The viscoelastic treatments can be done in different arrangements. In this work, the configuration adopted to increase the passive damping in a shaft is the passive constrained layer damping (PCLD) as shown in figure 5.11.

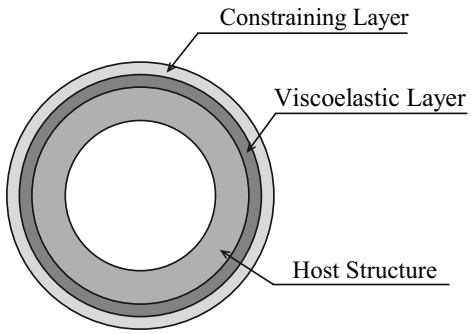

Figure 5.11. Passive constrained layer damping

It has been demonstrated that the PCLD is a much more efficient treatment due to their superior damping performance with low weight increase. In this treatment, an upper layer made of high elastic modulus material can be superimposed to the low modulus viscoelastic material in order to force the shear deformation in the viscoelastic layer, what increases the energy dissipation. The passive constrained layer damping treatments are being increasingly used in automotive, railway and aircraft applications due to their ability to reduce vibration and noise [Johnson, 1995].

In order to show the viscoelastic damping treatments effect, a non rotating simply supported shaft made of three layers is considered. The length of the shaft is $L = 1.2$ m. The geometric and the material properties of each layer are:

- First layer: host structure made of steel where:
  - Exterior radius $= R = 0.048$ m, wall thickness $= h = 0.008$ m;
  - $E = 210$ GPa, $\nu = 0.36$, $\rho = 7800$ kg/m^3;
- Second layer: viscoelastic layer where:
  - Interior radius $= R_v = 0.048$ m, wall thickness $= h_v = 0.25 \times 10^{-3}$ m;
  - $E = 7.28(1 + j\eta)$ MPa, loss factor $= \eta = 1.3$, $\nu = 0.45$, $\rho = 1140$ kg/m^3;
- Third layer: constrained layer made of aluminium where:

- Interior radius $= R_c = R_v + h_v$, wall thickness $= h_c = 1 \times 10^{-3}$ m;
- $E = 66$ GPa, $\nu = 0.33$, $\rho = 2680$ kg/m^3;

• Shear correction factor: $k_s = 1/2$.

It is worth to mention that the modulus of the shaft material and the viscoelastic material present a magnitude order difference of 5. The values of the lowest bending frequencies of the supported shaft made of three layers obtained using the new developed shaft finite element based on layerwise theory LST are compared with those obtained using ESLT as shown in table 5.6.

Table 5.6. Lowest bending frequencies (Hz) of the considered shaft

	First	Second	Third	Fourth	Fifth
ESLT	173.680	661.278	1388.22	2281.17	3287.58
LST	173.294	657.834	1375.25	2251.55	3235.80
%	0.22	0.52	0.93	1.3	1.57

The FRFs represented in figures 5.12 and 5.13 show the effect of viscoelastic damping treatments on the dynamic behaviour of the non rotating shaft.

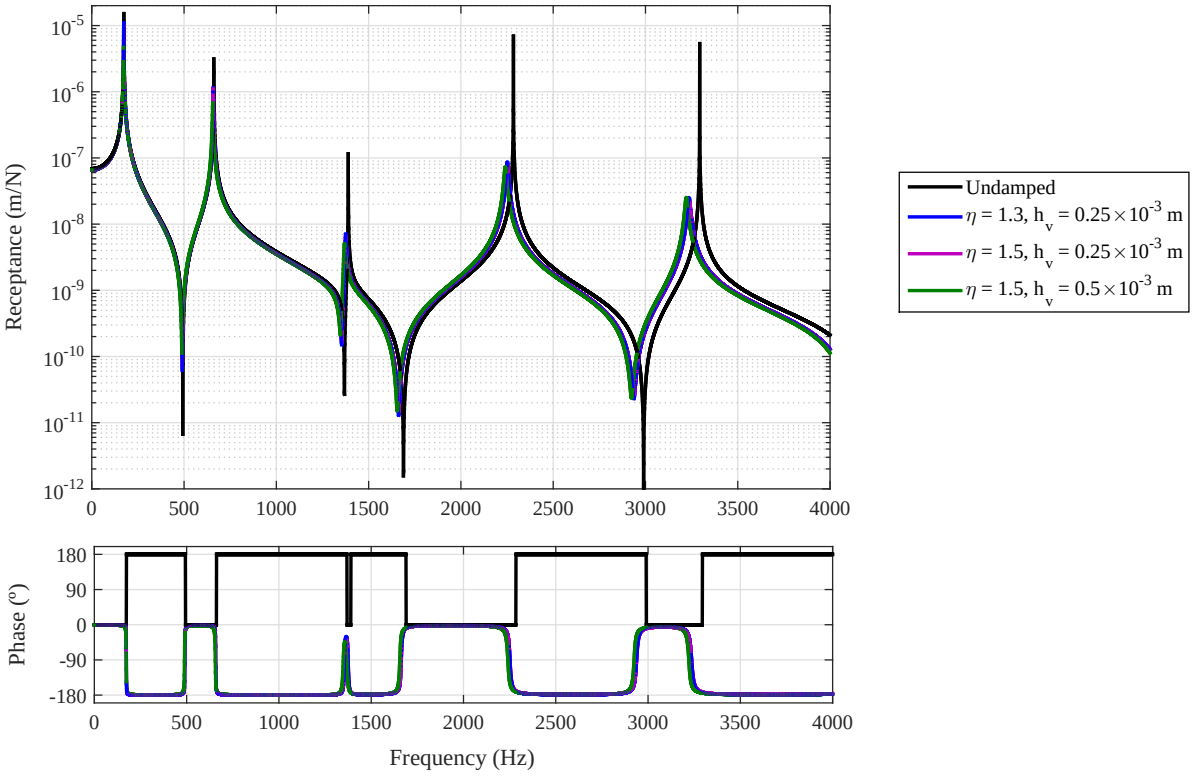

Figure 5.12. Effects of the variation of the loss factor and the viscoelastic layer thickness

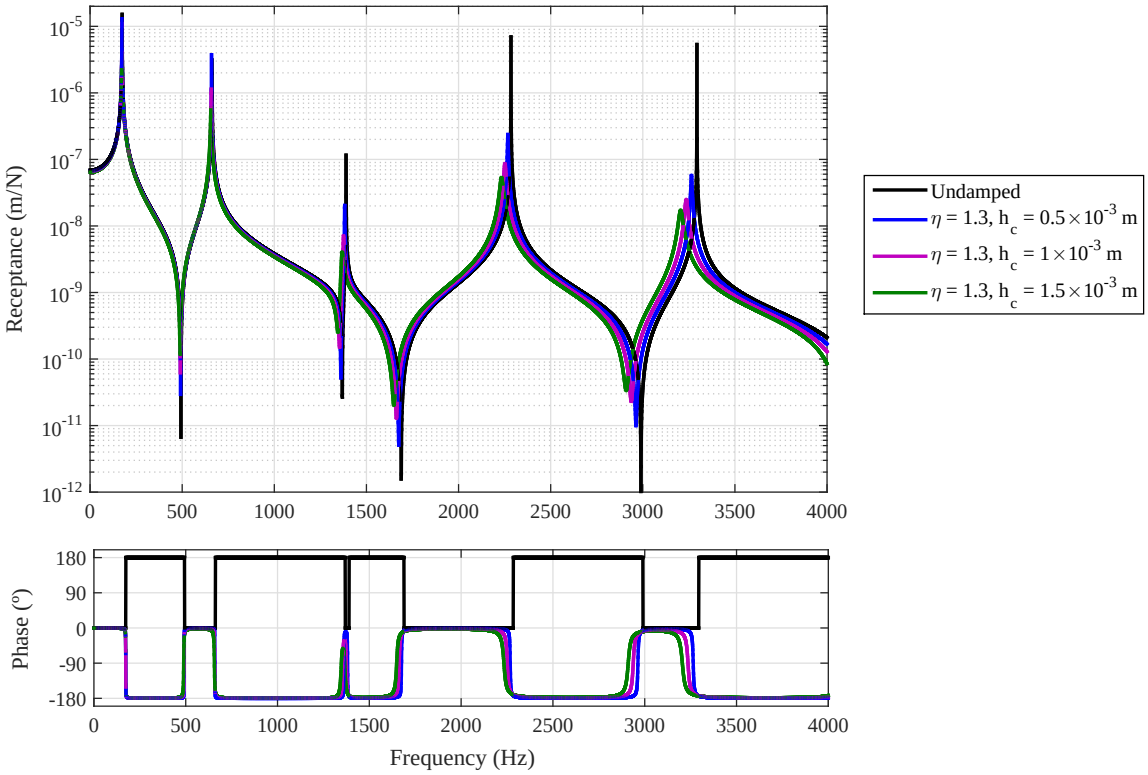

Figure 5.13. Effects of the variation of the constrained layer thickness

It can be observed from figure 5.12 that the shaft is more damped when we add the viscoelastic damping treatments. The amplitude of the receptance is lower than that of the undamped structure. For higher frequencies, natural frequencies decrease due to the addition of the mass of the viscoelastic layer and the constrained layer. However, the variation of the loss factor η from 1.3 to 1.5 does not affect the dynamic behaviour of the structure because the difference between this two values is not too important in this case. But, it is evident that if we increase (decrease) the loss factor η, the system will be more (less) damped. It can be observed also that when the viscoelastic layer thickness h_v increases, the system becomes more damped. But, we can consider that the damping capacity is negligible in front of viscoelastic material mass added. The analysis of the dynamic behaviour of the viscoelastic damping treatments should take into account the relation between the damping capacity and the adding mass.

5.13 Conclusion

The analysis of free vibration and frequency response of rotating laminated shafts using Layerwise Shaft Theory is presented in this chapter. Several examples for different layerwise laminated shaft applications have been processed to validate Layerwise Shaft Theory and to determine the influence of different geometrical and physical parameters of rotating laminated shafts on their dynamic behaviour. The development of this theory has allowed us to reach the following conclusions:

- The variation of the stacking sequence and the fiber orientation and the shear-normal coupling have significative effects on the dynamic behaviour of rotating composite shafts.

- The constituent material properties and the power law index have an important influence on the dynamic behaviour of functionally graded material rotating shafts.
- The passive viscoelastic damping treatments technology reveals efficient, although the relation between the damping capacity introduced and the mass added seems to be an important parameter.

Different deformation theories have been developed in the above chapters to analyse the dynamic behaviour of rotating laminated shafts by identifying the system natural frequencies, critical speeds and vibration response. Therefore, the stability analysis of rotating laminated composite shafts will be presented in the following chapter to identify the stability regions and the instability thresholds of the rotor system.

Chapter 6

Finite Element Formulation for Stability Analysis of rotating composite shafts

6.1 Introduction

A precise prediction of damping effects is basically necessary in the stability analysis of rotor dynamic behaviour. Damping is considered as an internal damping such as material damping or as an external damping as in the case of bearings damping and it is principally modeled using viscous or hysteretic damping. The basic difference between viscous and hysteric models is that the dissipation of energy by viscous damping depends on frequency, while the dissipation of energy by hysteretic damping does not. In composite rotor dynamic field, internal damping can be meaningful because of the damping capacity of the matrix [Wettergren and Olsson, 1996]. Moreover, most materials such as metallic materials, carbon/epoxy materials and viscoelastic materials show a vibratory damping behaviour which looks like hysteretic internal damping much more than viscous internal damping [Montagnier and Hochard, 2007].

In this chapter, a Euler-Bernoulli shaft finite element formulation based on Equivalent Single Layer Theory (ESLT) is adopted. ESLT consists on considering a laminated shaft made of several orthotropic layers as an equivalent single layer having equivalent mechanical properties of all the layers. In fact, each orthotropic layer contributes with its fiber orientation and its distance from the shaft longitudinal axis. The developed formulation considers the translatory, rotary inertia and gyroscopic effects as well as the shear transverse effect which was introduced in the shape functions. This formulation is developed to analyse the effects of hysteric internal damping, fiber orientation and stacking sequence on natural frequencies, critical speeds and instability thresholds of internally damped rotating composite shafts. A brief description of the theoretical background concerning the hysteretic internal damping modeling is presented. First, the deformation energy and the kinetic energy of the rotor system are established. Then, the finite element method is employed and the equation of motion is determined using Lagrange's equations.

6.2 Composite shaft

The stress-strain relation for a composite shaft including hysteretic internal damping is given by [Pereira and Silveira, 2002]:

$$\{\sigma\} = [Q]\{\varepsilon\} + [Q]^{\psi}\{\dot{\varepsilon}\} \tag{6.1}$$

where $[Q]^{\psi} = [Q][\eta]$ is the damped material stiffness matrix and $[\eta]$ is the damping matrix of the layer

which can be linked to the specific damping capacity matrix $[\psi]$ as follows:

$$[\eta] = \frac{1}{2\pi}[\psi] \tag{6.2}$$

The dissipative properties of the layer can also be expressed by using the specific damping capacity matrix $[\psi]$ defined as:

$$[\psi] = \begin{bmatrix} \psi_1 & 0 & 0 & 0 & 0 \\ 0 & \psi_2 & 0 & 0 & 0 \\ 0 & 0 & \psi_{23} & 0 & 0 \\ 0 & 0 & 0 & \psi_{13} & 0 \\ 0 & 0 & 0 & 0 & \psi_{12} \end{bmatrix} \tag{6.3}$$

where ψ_1, ψ_2, ψ_{23}, ψ_{13} and ψ_{12} are identified for each layer in the orthotropic axes $(1, 2, 3)$: 1 is the fiber direction, 2 is the transverse direction of the fiber and 3 is the perpendicular direction to the layer as shown in figure 3.6.

Consequently, the damped material stiffness matrix $[Q]^{\psi}$ is expressed as a function of the specific damping capacity matrix $[\psi]$ as:

$$[Q]^{\psi} = \frac{1}{2\pi}[Q][\psi] \tag{6.4}$$

Let consider an arbitrary layer of the laminate whose fiber orientation makes an angle α with respect to the x axis as shown in figure 3.6. The stress-strain relation including the hysteretic internal damping can be written in the global frame (x, y, z) as:

$$\{\sigma\} = \left[\bar{Q}\right]\{\varepsilon\} + \left[\bar{Q}\right]^{\psi}\{\dot{\varepsilon}\} \tag{6.5}$$

where $\left[\bar{Q}\right]$ is the transformed material stiffness matrix and $\left[\bar{Q}\right]^{\psi}$ is the transformed damped material stiffness matrix of the layer:

$$\left[\bar{Q}\right] = [T]^{\mathrm{T}}[Q][T] \quad \text{and} \quad \left[\bar{Q}\right]^{\psi} = [T]^{\mathrm{T}}[Q]^{\psi}[T] \tag{6.6}$$

where the transformation matrix $[T]$ is given by:

$$[T] = \begin{bmatrix} \cos^2\alpha & \sin^2\alpha & 0 & 0 & \cos\alpha\sin\alpha \\ \sin^2\alpha & \cos^2\alpha & 0 & 0 & -\cos\alpha\sin\alpha \\ 0 & 0 & \cos\alpha & -\sin\alpha & 0 \\ 0 & 0 & \sin\alpha & \cos\alpha & 0 \\ -2\cos\alpha\sin\alpha & 2\cos\alpha\sin\alpha & 0 & 0 & \cos^2\alpha - \sin^2\alpha \end{bmatrix} \tag{6.7}$$

The stress-strain relation expressed in equation (6.5) can be written as follows:

$$\{\sigma\} = \begin{cases} \sigma_{xx} = \bar{Q}_{11}\varepsilon_{xx} + \bar{Q}^{\psi}_{11}\dot{\varepsilon}_{xx} \\ \tau_{xz} = k_s\bar{Q}_{55}\gamma_{xz} + k_s\bar{Q}^{\psi}_{55}\dot{\gamma}_{xz} \\ \tau_{xy} = k_s\bar{Q}_{66}\gamma_{xy} + k_s\bar{Q}^{\psi}_{66}\dot{\gamma}_{xy} \end{cases} \tag{6.8}$$

where k_s is the shear correction factor and $\bar{Q}_{ij}$ and $\bar{Q}^{\psi}_{ij}$ are the constitutive terms which are related to the fiber orientation angle α and the elastic constants of principal axes as follows:

$$\begin{cases} \bar{Q}_{11} = Q_{11}\cos^4\alpha + Q_{22}\sin^4\alpha + (2Q_{12} + 4Q_{66})\cos^2\alpha\sin^2\alpha \\ \bar{Q}_{55} = Q_{44}\sin^2\alpha + Q_{55}\cos^2\alpha \\ \bar{Q}_{66} = (Q_{11} + Q_{22} - 2Q_{12})\cos^2\alpha\sin^2\alpha + Q_{66}(\cos^2\alpha - \sin^2\alpha)^2 \end{cases} \tag{6.9}$$

$$\begin{cases} \bar{Q}_{11}^{\psi} = \psi_1 Q_{11}\cos^4\alpha + \psi_2 Q_{22}\sin^4\alpha + (\psi_1 Q_{12} + \psi_2 Q_{12} + 4\psi_{12}Q_{66})\cos^2\alpha\sin^2\alpha \\ \bar{Q}_{55}^{\psi} = \psi_{23}Q_{44}\sin^2\alpha + \psi_{13}Q_{55}\cos^2\alpha \\ \bar{Q}_{66}^{\psi} = (\psi_1 Q_{11} + \psi_2 Q_{22} - \psi_1 Q_{12} - \psi_2 Q_{12})\cos^2\alpha\sin^2\alpha + \psi_{12}Q_{66}(\cos^2\alpha - \sin^2\alpha)^2 \end{cases} \tag{6.10}$$

6.3 Deformation energy

The displacement field is described by transverse displacements v and w along y and z directions respectively and slopes θ_y and θ_z in x-y and x-z planes respectively as shown in figure 6.1.

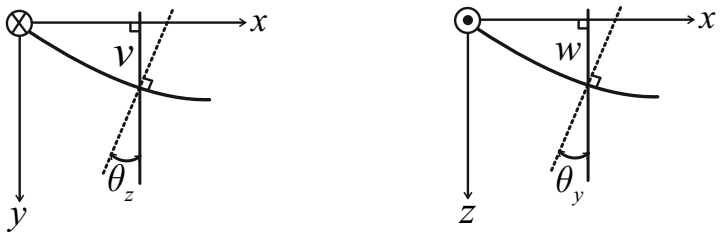

Figure 6.1. Displacement field variables

Considering small deformations, the longitudinal strain subjected to the bending efforts is given by:

$$\varepsilon_{xx} = z\frac{\partial\theta_y}{\partial x} - y\frac{\partial\theta_z}{\partial x} \tag{6.11}$$

Deriving the longitudinal strain expression (6.11) with respect to time, one gets:

$$\dot{\varepsilon}_{xx} = z\frac{\partial\dot{\theta}_y}{\partial x} - y\frac{\partial\dot{\theta}_z}{\partial x} \tag{6.12}$$

According to Euler-Bernoulli equations, the relations between the displacements v^* and w^* of the geometric center of the shaft cross section and the slopes θ_y and θ_z about y and z axis respectively are given as:

$$\theta_y = -\frac{\partial w^*}{\partial x} \qquad \text{and} \qquad \theta_z = \frac{\partial v^*}{\partial x} \tag{6.13}$$

Substituting equations (6.13) into equations (6.11) and (6.12), one gets:

$$\begin{cases} \varepsilon_{xx} = -z\dfrac{\partial^2 w^*}{\partial x^2} - y\dfrac{\partial^2 v^*}{\partial x^2} \\ \dot{\varepsilon}_{xx} = -z\dfrac{\partial^2 \dot{w}^*}{\partial x^2} - y\dfrac{\partial^2 \dot{v}^*}{\partial x^2} \end{cases} \tag{6.14}$$

The composite shaft deformation energy is given by:

$$\Pi = \frac{1}{2}\int_V \varepsilon^{\mathrm{T}}\sigma \mathrm{d}V$$

Considering the longitudinal strain subjected to the bending ε_{xx} and using equation (6.8), the internally damped composite shaft deformation energy can be expressed as:

$$\Pi = \frac{1}{2}\int_V \left(\bar{Q}_{11}\varepsilon_{xx}^2 + \bar{Q}_{11}^{\psi}\varepsilon_{xx}\dot{\varepsilon}_{xx}\right)\mathrm{d}V \tag{6.15}$$

Substituting equations (6.14) into composite shaft deformation energy expression (6.15) yields:

$$\Pi = \frac{1}{2}\int_V \bar{Q}_{11}\left(-z\frac{\partial^2 w^*}{\partial x^2} - y\frac{\partial^2 v^*}{\partial x^2}\right)^2 \mathrm{d}V + \frac{1}{2}\int_V \bar{Q}^{\psi}_{11}\left(-z\frac{\partial^2 w^*}{\partial x^2} - y\frac{\partial^2 v^*}{\partial x^2}\right)\left(-z\frac{\partial^2 \dot{w}^*}{\partial x^2} - y\frac{\partial^2 \dot{v}^*}{\partial x^2}\right)\mathrm{d}V \tag{6.16}$$

Accordingly to figure 6.2, the relations between the displacements v^* and w^* and the displacements v and w measured in the inertial axes system are:

$$\begin{cases} v^* = w\sin(\Omega t) + v\cos(\Omega t) \\ w^* = w\cos(\Omega t) - v\sin(\Omega t) \end{cases} \tag{6.17}$$

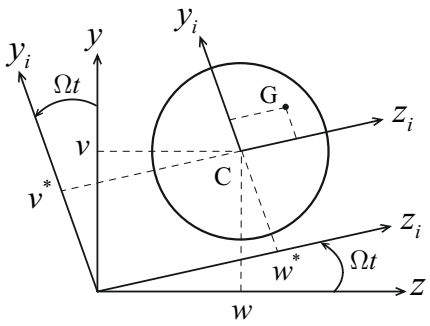

Figure 6.2. Coordinates of the geometric center C and an arbitrary point G in the shaft cross section axes system

Deriving equations (6.17) with respect to time, one gets the velocity expressions:

$$\begin{cases} \dot{v}^* = \dot{w}\sin(\Omega t) + w\Omega\cos(\Omega t) + \dot{v}\cos(\Omega t) - v\Omega\sin(\Omega t) \\ \dot{w}^* = \dot{w}\cos(\Omega t) - w\Omega\sin(\Omega t) - \dot{v}\sin(\Omega t) - v\Omega\cos(\Omega t) \end{cases} \tag{6.18}$$

Substituting equations (6.17) and (6.18) into composite shaft deformation energy expression (6.16) and integrating over the shaft cross sectional area by summing up the contribution of each orthotropic layer, the internally damped composite shaft deformation energy can be expressed as:

$$\begin{aligned} \Pi = {} & \frac{1}{2}A_{11}\int_0^L \left[\left(\frac{\partial^2 v}{\partial x^2}\right)^2 + \left(\frac{\partial^2 w}{\partial x^2}\right)^2\right]\mathrm{d}x \\ & + \frac{1}{2}A^{\psi}_{11}\int_0^L \left[\left(\frac{\partial^2 v}{\partial x^2}\frac{\partial^2 \dot{v}}{\partial x^2}\right) + \left(\frac{\partial^2 w}{\partial x^2}\frac{\partial^2 \dot{w}}{\partial x^2}\right)\right]\mathrm{d}x \\ & + \frac{1}{2}A^{\psi}_{11}\Omega\int_0^L \left[\left(\frac{\partial^2 v}{\partial x^2}\frac{\partial^2 w}{\partial x^2}\right) - \left(\frac{\partial^2 w}{\partial x^2}\frac{\partial^2 v}{\partial x^2}\right)\right]\mathrm{d}x \end{aligned} \tag{6.19}$$

where L is the length of the composite shaft, the second and the third terms are related to the hysteretic internal damping and the terms A_{11} and A^{ψ}_{11} are given as follows:

$$\begin{cases} A_{11} = \dfrac{\pi}{4}\displaystyle\sum_{p=1}^{P}\bar{Q}_{11p}\left(R_p^4 - R_{p-1}^4\right) \\ A^{\psi}_{11} = \dfrac{\pi}{4}\displaystyle\sum_{p=1}^{P}\bar{Q}^{\psi}_{11p}\left(R_p^4 - R_{p-1}^4\right) \end{cases} \tag{6.20}$$

where R_{p-1} is the inner radius and R_p is the outer radius of the pth layer of the composite shaft, as shown in figure 3.8.

6.4 Kinetic energy

Integrating over the shaft cross sectional area by summing up the contribution of each orthotropic layer, the kinetic energy of the rotating laminated shaft including the translatory, rotary inertia and gyroscopic effects is given by:

$$T = \frac{1}{2}\int_0^L \left[I_m \left(\dot{v}^2 + \dot{w}^2\right) + I_d\left(\dot{\theta}_y^2 + \dot{\theta}_z^2\right) - 2I_p\Omega\theta_y\dot{\theta}_z + I_p\Omega^2 \right] \mathrm{d}x \tag{6.21}$$

where the mass quantity I_m denotes the mass per unit length of the composite shaft, while I_d and I_p denote respectively the diametrical and the polar moment of inertia of the shaft cross section, defined in equations (3.32). The term $I_d\left(\dot{\theta}_y^2 + \dot{\theta}_z^2\right)$, given in equation (6.21), represents the rotary inertia effect and $2I_p\Omega\theta_y\dot{\theta}_z$ accounts for the gyroscopic effect.

6.5 Finite element definition

The developed shaft finite element has two nodes as shown in figure 3.11. For each node, the element has four degrees of freedom: two displacements v and w and two slopes θ_y and θ_z about y and z axes respectively.

The nodal degrees of freedom vector of the shaft element is given by:

$$\{q^e\} = \begin{Bmatrix} v_1 & w_1 & \theta_{y_1} & \theta_{z_1} & v_2 & w_2 & \theta_{y_2} & \theta_{z_2} \end{Bmatrix}^{\mathrm{T}} \tag{6.22}$$

which, accordingly to the relations (6.13), includes the nodal vectors $\{q_v^e\}$ and $\{q_w^e\}$ given by:

$$\begin{aligned} \{q_v^e\} &= \begin{Bmatrix} v_1 & \theta_{z_1} & v_2 & \theta_{z_2} \end{Bmatrix}^{\mathrm{T}} \\ \{q_w^e\} &= \begin{Bmatrix} w_1 & -\theta_{y_1} & w_2 & -\theta_{y_2} \end{Bmatrix}^{\mathrm{T}} \end{aligned} \tag{6.23}$$

The displacement functions v and w are defined as:

$$v = [N]\{q_v^e\} \quad \text{and} \quad w = [N]\{q_w^e\} \tag{6.24}$$

where $[N]$ is the shape function matrix. Under the Euler-Bernoulli beam hypothesis [Hinton and Owen, 1981] and considering the transverse shear effect through the parameter Φ, the shape function matrix is defined as:

$$[N] = \frac{1}{4(1+\Phi)}\begin{bmatrix} N_1 & N_2 & N_3 & N_4 \end{bmatrix} \tag{6.25}$$

Using the normalized coordinate $\xi \in [-1, 1]$ with its origin at $x = L^e/2$, the one-dimensional interpolation functions in terms of the normalized coordinate are defined as:

$$\begin{cases} N_1 = 2 - 3\xi + \xi^3 + 2\Phi\left(1 - \xi\right) \\ N_2 = J\left(1 - \xi - \xi^2 + \xi^3 + \Phi\left(1 - \xi^2\right)\right) \\ N_3 = 2 + 3\xi - \xi^3 + 2\Phi\left(1 + \xi\right) \\ N_4 = J\left(-1 - \xi + \xi^2 + \xi^3 - \Phi\left(1 - \xi^2\right)\right) \end{cases} \tag{6.26}$$

where J is the Jacobian of the transformation.

For a composite shaft, the transverse shear effect parameter Φ, presented in equations (6.25) and (6.26), is given by [Muslmani, 2013]:

$$\Phi = \frac{12A_{11}}{k_s(A_{55}+A_{66})L^{e^2}} \tag{6.27}$$

where the term A_{11} is defined in equation (6.20) and the terms A_{55} and A_{66}, including the contribution of each orthotropic layer, are given as follows:

$$\begin{cases} A_{55} = \pi \sum_{p=1}^{P} \bar{Q}_{55p} \left(R_p^2 - R_{p-1}^2\right) \\ A_{66} = \pi \sum_{p=1}^{P} \bar{Q}_{66p} \left(R_p^2 - R_{p-1}^2\right) \end{cases} \tag{6.28}$$

6.5.1 Elementary stiffness, dissipation and circulation matrices

The deformation energy described in equation (6.19) can be expressed as the sum of the elemental deformation energy leading to the definition of the elementary stiffness, dissipation and circulation matrices. Adding the contribution of all the E finite elements, the deformation energy can be expressed as:

$$\Pi = \sum_{e=1}^{E} \Pi^e \tag{6.29}$$

Using the interpolation (6.24) for the displacement function expressions v and w and the deformation energy expression (6.19), the elemental internally damped composite shaft deformation energy Π^e can be expressed as:

$$\begin{aligned} \Pi^e = & \frac{1}{2}A_{11} \int_0^{L^e} \left[\{q_v^e\}^{\mathrm{T}} \frac{d^2}{dx^2} [N]^{\mathrm{T}} \frac{d^2}{dx^2} [N] \{q_v^e\} + \{q_w^e\}^{\mathrm{T}} \frac{d^2}{dx^2} [N]^{\mathrm{T}} \frac{d^2}{dx^2} [N] \{q_w^e\} \right] \mathrm{d}x \\ & + \frac{1}{2}A_{11}^{\psi} \int_0^{L^e} \left[\{q_v^e\}^{\mathrm{T}} \frac{d^2}{dx^2} [N]^{\mathrm{T}} \frac{d^2}{dx^2} [N] \{\dot{q}_v^e\} + \{q_w^e\}^{\mathrm{T}} \frac{d^2}{dx^2} [N]^{\mathrm{T}} \frac{d^2}{dx^2} [N] \{\dot{q}_w^e\} \right] \mathrm{d}x \\ & + \frac{1}{2}A_{11}^{\psi}\Omega \int_0^{L^e} \left[\{q_v^e\}^{\mathrm{T}} \frac{d^2}{dx^2} [N]^{\mathrm{T}} \frac{d^2}{dx^2} [N] \{q_w^e\} - \{q_w^e\}^{\mathrm{T}} \frac{d^2}{dx^2} [N]^{\mathrm{T}} \frac{d^2}{dx^2} [N] \{q_v^e\} \right] \mathrm{d}x \end{aligned} \tag{6.30}$$

So, the internally damped composite shaft deformation energy can be written as:

$$\Pi = \sum_{e=1}^{E} \Pi^e = \sum_{e=1}^{E} \left(\frac{1}{2} \{q^e\}^{\mathrm{T}} [K^e] \{q^e\} + \frac{1}{2} \{q^e\}^{\mathrm{T}} [H_d^e] \{\dot{q}^e\} + \frac{1}{2} \{q^e\}^{\mathrm{T}} [H_c^e(\Omega)] \{q^e\} \right) \tag{6.31}$$

where $[K^e]$ is the elementary stiffness matrix and $[H_d^e]$ and $[H_c^e(\Omega)]$ are the elementary matrices related

to the hysteretic internal damping, given by:

$$[K^e] = \frac{A_{11}}{(1+\Phi)\,L^{e^3}} \begin{bmatrix} 12 & 0 & 0 & -6L^e & -12 & 0 & 0 & -6L^e \\ & 12 & 6L^e & 0 & 0 & -12 & 6L^e & 0 \\ & & (4+\Phi)\,L^{e^2} & 0 & 0 & -6L^e & (2-\Phi)\,L^{e^2} & 0 \\ & & & (4+\Phi)\,L^{e^2} & 6L^e & 0 & 0 & (2-\Phi)\,L^{e^2} \\ & & & & 12 & 0 & 0 & 6L^e \\ & & & & & 12 & -6L^e & 0 \\ & \text{Sym.} & & & & & (4+\Phi)\,L^{e^2} & 0 \\ & & & & & & & (4+\Phi)\,L^{e^2} \end{bmatrix} \tag{6.32}$$

$$[H_d^e] = \frac{A_{11}^{\psi}}{(1+\Phi)\,L^{e^3}} \begin{bmatrix} 12 & 0 & 0 & -6L^e & -12 & 0 & 0 & -6L^e \\ & 12 & 6L^e & 0 & 0 & -12 & 6L^e & 0 \\ & & (4+\Phi)\,L^{e^2} & 0 & 0 & -6L^e & (2-\Phi)\,L^{e^2} & 0 \\ & & & (4+\Phi)\,L^{e^2} & 6L_e & 0 & 0 & (2-\Phi)\,L^{e^2} \\ & & & & 12 & 0 & 0 & 6L^e \\ & & & & & 12 & -6L^e & 0 \\ & \text{Sym.} & & & & & (4+\Phi)\,L^{e^2} & 0 \\ & & & & & & & (4+\Phi)\,L^{e^2} \end{bmatrix} \tag{6.33}$$

$$[H_c^e\,(\Omega)] = \frac{A_{11}^{\psi}\Omega}{(1+\Phi)\,L^{e^3}} \begin{bmatrix} 0 & -12 & -6L^e & 0 & 0 & 12 & -6L^e & 0 \\ & 0 & 0 & -6L^e & -12 & 0 & 0 & -6L^e \\ & & 0 & -(4+\Phi)\,L^{e^2} & -6L^e & 0 & 0 & -(2-\Phi)\,L^{e^2} \\ & & & 0 & 0 & -6L^e & (2-\Phi)\,L^{e^2} & 0 \\ & & & & 0 & -12 & 6L^e & 0 \\ & & & & & 0 & 0 & 6L^e \\ & \text{Skew-Sym.} & & & & & 0 & -(4+\Phi)\,L^{e^2} \\ & & & & & & & 0 \end{bmatrix} \tag{6.34}$$

6.5.2 Elementary mass and gyroscopic matrices

The kinetic energy described in equation (6.21) can be expressed as the sum of the elemental kinetic energy leading to the definition of the elementary mass and gyroscopic matrices. Adding the contribution of all the E finite elements, the kinetic energy can be expressed as:

$$T = \sum_{e=1}^{E} T^e \tag{6.35}$$

Using the interpolation (6.24) for the displacement function expressions v and w and the kinetic

energy expression (6.21), the elemental kinetic energy T^e can be expressed as:

$$\begin{aligned} T^e = & \frac{1}{2} I_m \int_0^{L^e} \left[\{\dot{q}_v^e\}^{\mathrm{T}} [N]^{\mathrm{T}} [N] \{\dot{q}_v^e\} + \{\dot{q}_w^e\}^{\mathrm{T}} [N]^{\mathrm{T}} [N] \{\dot{q}_w^e\} \right] \mathrm{d}x \\ & + \frac{1}{2} I_d \int_0^{L^e} \left[\{\dot{q}_v^e\}^{\mathrm{T}} \frac{d}{dx} [N]^{\mathrm{T}} \frac{d}{dx} [N] \{\dot{q}_v^e\} + \{\dot{q}_w^e\}^{\mathrm{T}} \frac{d}{dx} [N]^{\mathrm{T}} \frac{d}{dx} [N] \{\dot{q}_w^e\} \right] \mathrm{d}x \\ & - I_p \Omega \int_0^{L^e} \left[\{q_v^e\}^{\mathrm{T}} \frac{d}{dx} [N]^{\mathrm{T}} \frac{d}{dx} [N] \{\dot{q}_w^e\} \right] \mathrm{d}x \end{aligned} \tag{6.36}$$

So, the kinetic energy can be written as:

$$T = \sum_{e=1}^{E} T^e = \sum_{e=1}^{E} \left(\frac{1}{2} \{\dot{q}^e\}^{\mathrm{T}} [M^e] \{\dot{q}^e\} + \frac{1}{2} \{q^e\}^{\mathrm{T}} [G^e(\Omega)] \{\dot{q}^e\} \right) \tag{6.37}$$

where $[M^e]$ is the elementary mass matrix and $[G^e(\Omega)]$ is the elementary gyroscopic matrix, given by:

$$[M^e] = \frac{L^e}{840(1+\Phi)^2} \begin{bmatrix} M_1 & 0 & 0 & M_2 & M_3 & 0 & 0 & M_4 \\ & M_1 & -M_2 & 0 & 0 & M_3 & -M_4 & 0 \\ & & M_5 & 0 & 0 & M_4 & M_6 & 0 \\ & & & M_5 & -M_4 & 0 & 0 & M_6 \\ & & & & M_1 & 0 & 0 & -M_2 \\ & & & & & M_1 & M_2 & 0 \\ & \text{Sym.} & & & & & M_5 & 0 \\ & & & & & & & M_5 \end{bmatrix} \tag{6.38}$$

$$[G^e(\Omega)] = \frac{I_p \Omega}{60 L^e (1+\Phi)^2} \begin{bmatrix} 0 & G_1 & G_2 & 0 & 0 & -G_1 & G_2 & 0 \\ & 0 & 0 & G_2 & G_1 & 0 & 0 & G_2 \\ & & 0 & G_3 & G_2 & 0 & 0 & G_4 \\ & & & 0 & 0 & G_2 & -G_4 & 0 \\ & & & & 0 & G_1 & -G_2 & 0 \\ & & & & & 0 & 0 & -G_2 \\ & \text{Skew-Sym.} & & & & & 0 & G_3 \\ & & & & & & & 0 \end{bmatrix} \tag{6.39}$$

The elementary mass components given in equation (6.38) are expressed as:

$$\begin{cases} M_1 = I_m \left(312 + 588 + 280\Phi^2\right) + \dfrac{1008 I_d}{L^{e^2}} \\ M_2 = -I_m L^e \left(44 + 77\Phi + 35\Phi^2\right) - \dfrac{(84 - 420\Phi) I_d}{L^e} \\ M_3 = I_m \left(108 + 252\Phi + 140\Phi^2\right) - \dfrac{1008 I_d}{L^{e^2}} \\ M_4 = I_m L^e \left(26 + 63\Phi + 35\Phi^2\right) - \dfrac{(84 - 420\Phi) I_d}{L^e} \\ M_5 = I_m L^{e^2} \left(8 + 14\Phi + 7\Phi^2\right) + I_d \left(112 + 140\Phi + 280\Phi^2\right) \\ M_6 = -I_m L^{e^2} \left(6 + 14\Phi + 7\Phi^2\right) - I_d \left(28 + 140\Phi - 140\Phi^2\right) \end{cases} \tag{6.40}$$

and the elementary gyroscopic terms presented in equation (6.39) are given by:

$$\begin{cases} G_1 = -72 \\ G_2 = -L^e\left(6 - 30\Phi\right) \\ G_3 = -L^{e^2}\left(8 + 10\Phi + 20\Phi^2\right) \\ G_4 = L^{e^2}\left(2 + 10\Phi - 10\Phi^2\right) \end{cases} \tag{6.41}$$

6.6 Equation of motion

The relation between the elemental degrees of freedom and the global degrees of freedom is established through the connectivity matrices $[R^e]$, expressed as:

$$\{q^e\} = [R^e]\{q\} \tag{6.42}$$

where $\{q\}$ represents the vector of global degrees of freedom.

Introducing the connectivity (6.42) into internally damped composite shaft deformation energy expression (6.31) gives:

$$\Pi = \frac{1}{2}\{q\}^{\mathrm{T}}[K]\{q\} + \frac{1}{2}\{q\}^{\mathrm{T}}[H_d]\{\dot{q}\} + \frac{1}{2}\{q\}^{\mathrm{T}}[H_c(\Omega)]\{q\} \tag{6.43}$$

where the assembled stiffness matrix $[K]$ and the assembled matrices related to the hysteretic internal damping matrices $[H_d]$ and $[H_c(\Omega)]$ are defined by:

$$\begin{cases} [K] = \sum_{e=1}^{E}[R^e]^{\mathrm{T}}[K^e][R^e] \\ [H_d] = \sum_{e=1}^{E}[R^e]^{\mathrm{T}}[H_d^e][R^e] \\ [H_c(\Omega)] = \sum_{e=1}^{E}[R^e]^{\mathrm{T}}[H_c^e(\Omega)][R^e] \end{cases} \tag{6.44}$$

Introducing also the connectivity (6.42) into kinetic energy expression (6.37) gives:

$$T = \frac{1}{2}\{\dot{q}\}^{\mathrm{T}}[M]\{\dot{q}\} + \frac{1}{2}\{q\}^{\mathrm{T}}[G(\Omega)]\{\dot{q}\} \tag{6.45}$$

where the assembled global mass $[M]$ and gyroscopic $[G(\Omega)]$ matrices are defined by:

$$\begin{cases} [M] = \sum_{e=1}^{E}[R^e]^{\mathrm{T}}[M^e][R^e] \\ [G(\Omega)] = \sum_{e=1}^{E}[R^e]^{\mathrm{T}}[G^e(\Omega)][R^e] \end{cases} \tag{6.46}$$

The Lagrange's equation is adopted herein:

$$\frac{\mathrm{d}}{\mathrm{d}t}\left(\frac{\partial T}{\partial \dot{q}}\right) - \frac{\partial T}{\partial q} + \frac{\partial \Pi}{\partial q} = 0 \tag{6.47}$$

Applying Lagrange's equations (6.47) to the kinetic energy expression (6.45) and the deformation energy expression (6.31) yields to the definition of the equation of motion of the hysteretic damped rotating system:

$$[M]\{\ddot{q}\} + \Big([G(\Omega)] + [H_d]\Big)\{\dot{q}\} + \Big([K] + [H_c(\Omega)]\Big)\{q\} = \{0\} \tag{6.48}$$

where $[M]$ is the symmetric mass matrix, $[G(\Omega)]$ is the skew-symmetric gyroscopic matrix which is rotational speed Ω dependent, $[K]$ is the stiffness matrix and $[H_d]$ and $[H_c(\Omega)]$ are the matrices related to the hysteric internal damping. $\{\ddot{q}\}$, $\{\dot{q}\}$ and $\{q\}$ are respectively nodal acceleration, nodal velocity and nodal displacement vectors.

Using the equivalence between the hysteretic damping and the viscous damping, the symmetric dissipation matrix $[K_d]$ and the skew-symmetric circulation matrix $[K_c(\Omega)]$, which is rotational speed Ω dependent, are obtained as follows Lalanne et al. [1986]:

$$\begin{cases} [K_d] = \dfrac{1}{\pi}[H_d][\omega]^{-1} \\ [K_c(\Omega)] = \dfrac{1}{\pi}[H_c(\Omega)][\omega]^{-1} \end{cases} \tag{6.49}$$

where $[\omega]$ is the diagonal natural frequencies matrix of the undamped non rotating system [Silveira, 2001].

Therefore, the equation of motion of the hysteretic damped rotating system can be written:

$$[M]\{\ddot{q}\} + \Big([G(\Omega)] + [K_d]\Big)\{\dot{q}\} + \Big([K] + [K_c(\Omega)]\Big)\{q\} = \{0\} \tag{6.50}$$

where spatial matrices are of order n for an n degrees of freedom system. It is well known that the presence of a circulation matrix can cause instability, and rotors are no exception to this rule [Genta, 2005].

The dynamic equilibrium equation (6.50) can be written in the first order form as:

$$[A]\{\dot{x}\} + [B(\Omega)]\{x\} = \{0\} \tag{6.51}$$

which is the state-space form of the equation of motion where the $2n \times 2n$ matrix $[A]$ is a real symmetric positive definite matrix, the $2n \times 2n$ matrix $[B]$ is a real non-symmetric matrix and the $2n$ vector $\{x\}$ is the state-space vector, defined as:

$$[A] = \begin{bmatrix} [M] & [0] \\ [0] & [M] \end{bmatrix}, \qquad [B(\Omega)] = \begin{bmatrix} [0] & -[M] \\ [K] + [K_c(\Omega)] & [G(\Omega)] + [K_d] \end{bmatrix}, \qquad \{x\} = \begin{Bmatrix} q \\ \dot{q} \end{Bmatrix} \tag{6.52}$$

The solutions of equation (6.51) can be assumed as:

$$\{x\} = \{X\}\,\mathrm{e}^{\lambda t} \tag{6.53}$$

which, after introduction in (6.51), lead to the generalized eigenvalue problem:

$$[B(\Omega)]\{X\} = -\lambda[A]\{X\} \tag{6.54}$$

which has $2n$ eigensolutions (λ_r, X_r). The eigenvalues λ_r are obtained as n pairs of complex conjugates of the form:

$$\lambda_r = \mu_r \pm \mathrm{j}\omega_r \tag{6.55}$$

where the imaginary part ω_r are the natural frequencies and the real part μ_r characterise the stability of the system. In fact, if $\mu_r > 0$, the system is unstable [Pereira and Silveira, 2002].

6.7 Results and discussion

6.7.1 Stacking sequence effect

The rotor test , studied first by [Pereira and Silveira, 2002] and then by [Sino et al., 2008], which is a composite shaft with two rigid steel discs supported by two bearings at the ends, is considered. The geometric and material properties of the structure are presented in the section 3.7.1. The carbon/epoxy shaft properties of each layer are summarized in table 6.1.

Table 6.1. Carbon/epoxy material data

E_1 (GPa)	E_2 (GPa)	G_{ij} (GPa)	ν_{12}	ρ (kg/m^3)	$\psi_1(\%)$	$\psi_2(\%)$	$\psi_{12}(\%)$
172.7	7.2	3.76	0.3	1446.2	0.45	4.22	7.05

Table 6.2 gives the first natural frequency and the instability threshold obtained from the proposed model ESLT for different stacking sequences in both symmetric and non-symmetric configurations with 8 layers of equal thickness.

Table 6.2. Stacking sequence effects on fundamental natural frequency (Hz) and instability threshold (rpm)

Stacking Sequence	ω_1(Hz)			Instability threshold (rpm)		
	EMBT[1]	SHBT [2]	ESLT	EMBT[1]	SHBT[2]	ESLT
1: $[\pm 75]_{8S}$	16.88	16.88	17.22	1167	1167	1210
2: $[90_2, 45, 0]_S$	42.76	39.87	42.20	6956	5864	6481
3: $[90, 0, 90, 45, 90, 45, 0, 90]$	42.76	40.08	42.41	6965	5913	6559
4: $[90, 45, 0_2]_S$	52.37	50.71	51.79	12064	10981	11060
5: $[0_2, 45_2, 90_2, 0_2]$	53.37	50.91	51.83	12064	11106	11084
6: $[0_2, 90, 45]_S$	52.37	50.92	51.96	12064	11111	11165
7: $[45, 0, 45, 0, 90, 0, 90, 0]$	52.37	51.36	52.07	12064	11395	11235

[1] [Pereira and Silveira, 2002].
[2] [Sino et al., 2008].

The instability threshold values given in table 6.2 are obtained from figure 6.3 where the real parts of the eigenvalues are presented in function of the rotational speed of the rotor. In fact, when the real parts of the eigenvalues become positive, the instability occurs.

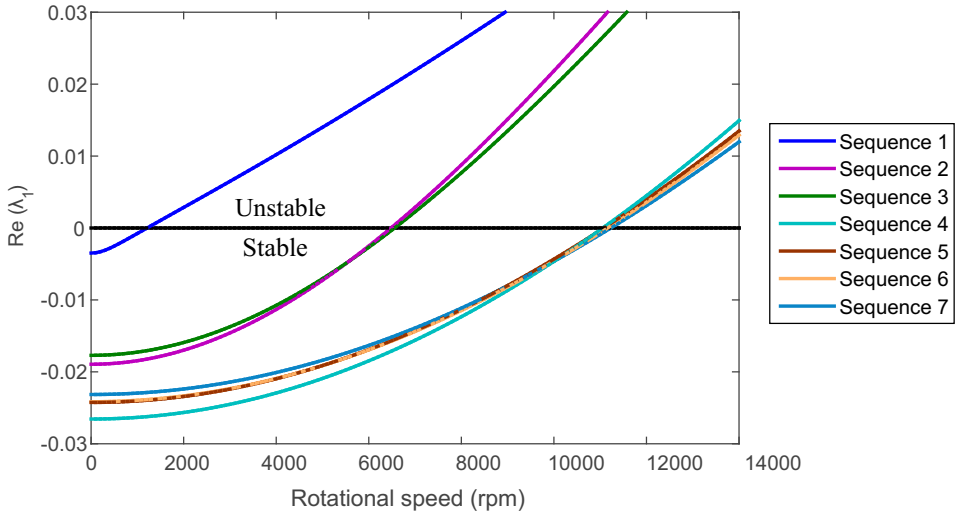

Figure 6.3. Real part of the eigenvalue of the first forward mode

It appears from table 3.3 that obtained results are in good agreement with those obtained using both theories and are closer to results obtained by [Pereira and Silveira, 2002] using formulation based on EMBT. In fact, [Pereira and Silveira, 2002] used Euler-Bernoulli beam theory based on EMBT excluding the transverse shear. Actually, [Singh and Gupta, 1996a,b] showed that EMBT is quite adequate for estimation of dynamic behaviour of rotating composite shafts but predicts inaccurate results for non-symmetric stacking sequences. In the other hand, SHBT proposed by [Sino et al., 2008] used Timoshenko beam theory considering the transverse shear effects and the stacking sequence effects. However, the formulation developed in this work employs Euler-Bernoulli beam theory based on ESLT including the transverse shear and the stacking sequence effects as well as the hysteretic internal damping effects. It can be concluded that the Euler-Bernoulli finite element formulation based on ESLT developed in this work is adequate for the dynamic and stability analysis of rotating composite shafts considering transverse shear, stacking sequence and hysteretic internal damping effects.

Stacking sequences 2-3 are composed of four layers with fibers orientated at $90°$, two layers with fibers orientated at $45°$ and two layers with fibers orientated at $0°$, whereas stacking sequences 4-7 are composed of four layers with fibers orientated at $0°$, two layers with fibers orientated at $45°$ and two layers with fibers orientated at $90°$. Each layer contributes in function of its fiber orientation and its distance from the longitudinal shaft axis. When comparing stacking sequences 2 to 7, differences of 19% for the fundamental natural frequency and 42% for the associated instability threshold are obtained. When comparing instability threshold values obtained for the stacking sequence 1 with 2 and those obtained for the stacking sequence 3 with 4, 5, 6 and 7 (see table 6.2), it can be shown that the greater the number of layers with fibers oriented at $90°$ and positioned at the outer and the inner radius, the more the instability may appear at lower rotational speed.

A modal analysis is performed to see the effects of changing rotational speeds, from a non-rotating to a high rotational speed and to follow the frequencies associated with the bending modes. Figures 6.4 and 6.5 show the Campbell diagrams for forward and backward natural frequencies over a wide speed range for the second and the fifth stacking sequences respectively (see table 6.2). From this figures, it

can observed that the frequencies of the bending modes do change over the rotational speed range. The backward mode (BW) decreases in frequency, while the forward mode (FW) increases.

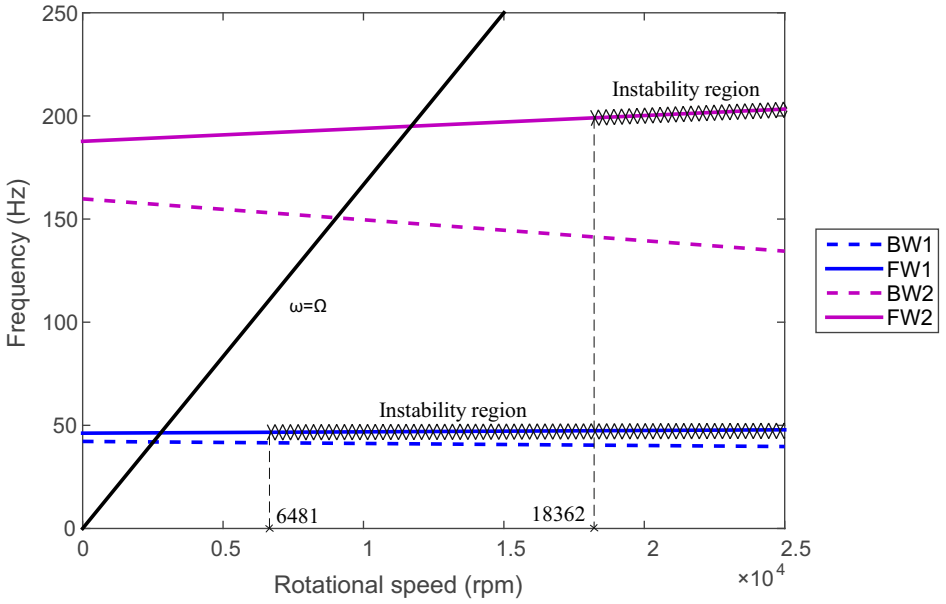

Figure 6.4. Campbell diagram: second sequence $[90_2, 45, 0]_S$

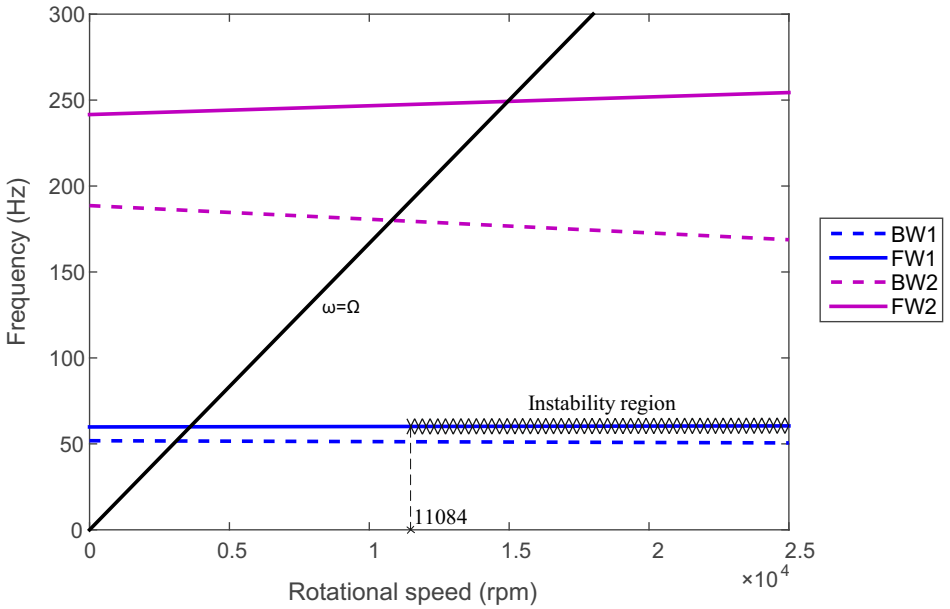

Figure 6.5. Campbell diagram: fifth sequence $[0_2, 45_2, 90_2, 0_2]$

Campbell diagrams, associated to the second and the fifth stacking sequence (see table 6.2) which are shown in figures 6.4 and 6.5, perform the evolution of natural frequencies with rotational speeds and illustrate the meaningful influence of stacking sequences on natural frequencies, critical speeds and instability thresholds. Variations of 18% for fundamental natural frequencies and 41% for the instability thresholds are obtained when comparing the second and the fifth stacking sequences. As it is expected,

for different stacking sequences, the instability appears in the supercritical ranges only for the forward bending modes (FW). The backward bending modes (BW) are stable for all the rotational speeds. For the second stacking sequence, the instability occurs in the first and the second forward bending modes (FW1 and FW2), whereas for the fifth stacking sequence, the instability occurs just in the first forward bending mode (FW1) in the considered rotational speed range. For the fifth stacking sequence, critical speeds are higher than those of the second stacking sequence and rotor speed surpass the third critical speed without producing rotor instability, while for the second stacking sequence, instability appears following the second critical speed. This behaviour is explained by the fact that the greater the number of layers with fibers oriented at 90° and positioned at the outer and the inner radius such as the second stacking sequence $[90_2, 45, 0]_S$, the more the instability may appear at lower rotational speed. Consequently, it can be concluded that the greater the number of layers with fibers oriented close to the longitudinal direction of the shaft (fibers oriented at 0°) and positioned at the outer and the inner radius of the shaft, the more they contribute to the shaft rigidity and therefore, the higher natural frequencies and critical speeds are and the lower the internal composite materials damping is and thus, the more the instability appears at higher rotational speed.

6.7.2 Fiber orientation effect

In order to show the effects of fiber orientations on natural frequencies, critical speeds and instability threshold, a rotor of the same geometric and material properties as the rotor test with two rigid steel discs and supported by two isotropic bearings at the ends ($K_{yy} = K_{zz} = 1 \times 10^8$ N/m) is considered. The stacking sequence of composite material consists of one layer $[\alpha]$. Figure 6.6 shows the Campbell diagram of the first pairs of the bending mode and the instability region of the rotor (symbolized by dashed line).

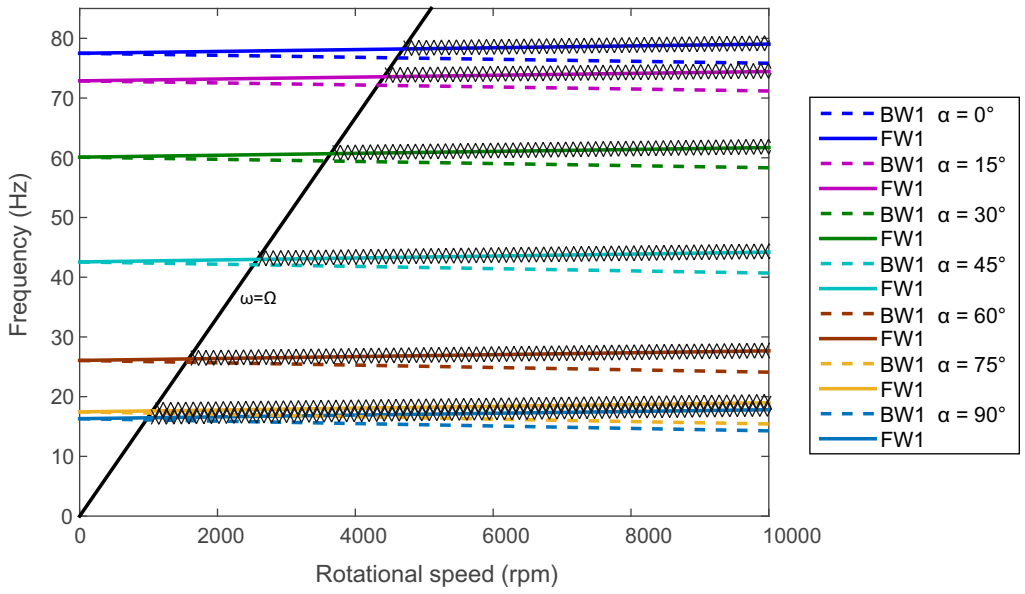

Figure 6.6. Fiber orientation effects of rotating composite shaft

It can be observed from figure 6.6 that the backward modes are stable at all rotational speeds, whereas

the forward modes destabilize from the first critical speed. Figure 6.7 shows the instability threshold for different fiber orientations. The instability region corresponds the the region above the curve.

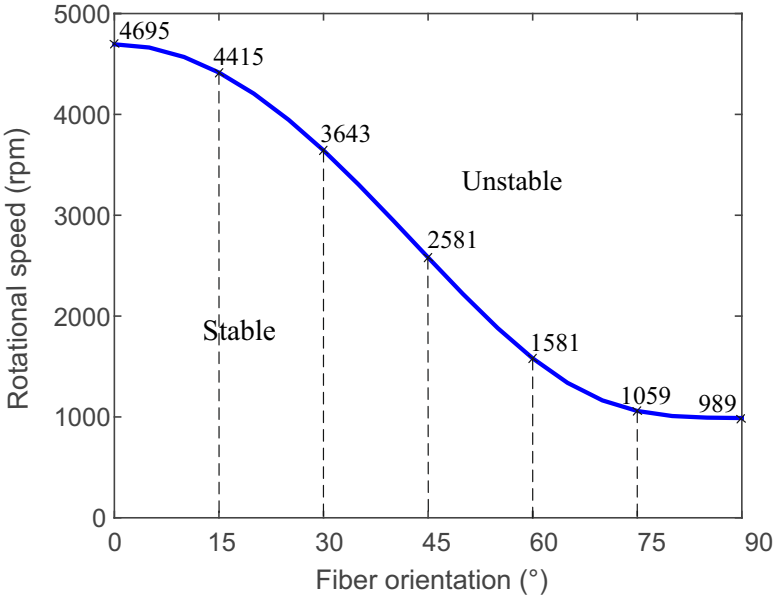

Figure 6.7. Instability threshold for different fiber orientations

As it was concluded in the above sections, as higher is the fiber orientation angle, higher is the internal damping of the composite material matrix and therefore, the instability occurs at lower rotational speed. It can be observed from both figures 6.6 and 6.7 that for small fiber orientation angle, the internal composite material damping has a less influence on the rotor instability which occurs at higher rotational speed compared to the large fibre orientation angle. It can be concluded that the closer the fibre is oriented to the longitudinal direction of the shaft, the higher the natural frequencies and critical speeds are and at higher rotational speed, the rotor instability appears.

6.7.3 Bearings properties effect

In order to analyse the bearing properties effects on natural frequencies, critical speeds and instability thresholds, a rotor of the same geometric and material properties as the rotor test with two rigid steel discs and supported by two isotropic bearings at the ends is considered. As the bearings are isotropic, their stiffness and their damping are the same in two orthogonal directions: $K_{yy} = K_{zz} = 1 \times 10^8$ N/m and $C_{yy} = C_{zz}$. Isotropic bearings with coupled terms $K_{yz} = K_{zy} = 1 \times 10^7$ N/m are also considered. The composite shaft configuration is balanced and symmetric: $[\pm 15]_{8S}$.

Considering the isotropic bearings without external damping, figure 6.8 shows the Campbell diagram of the rotating composite shaft supported by isotropic bearings, while figure 6.9 shows the Campbell diagram of the rotating composite shaft supported by isotropic bearings with coupled terms.

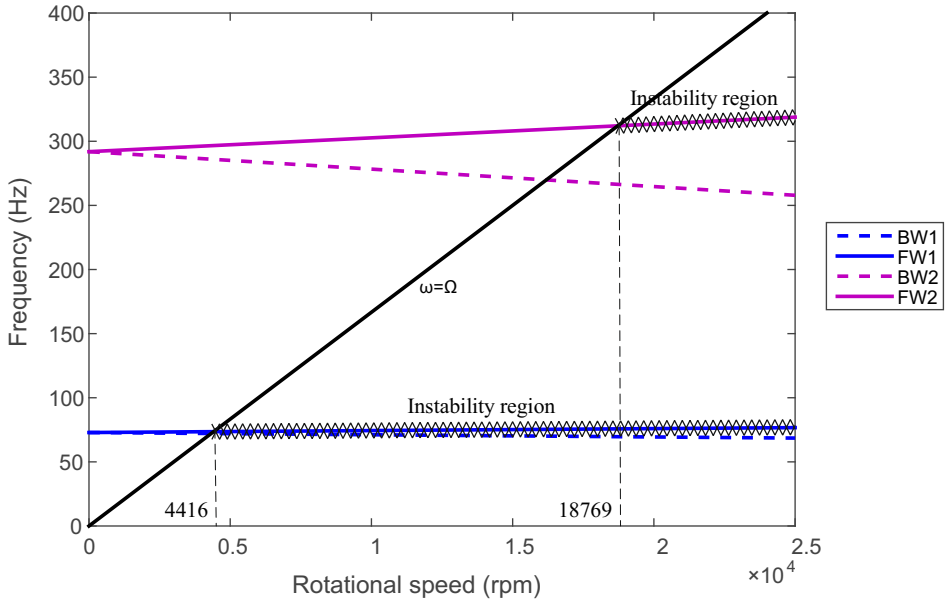

Figure 6.8. Case: isotopic bearings

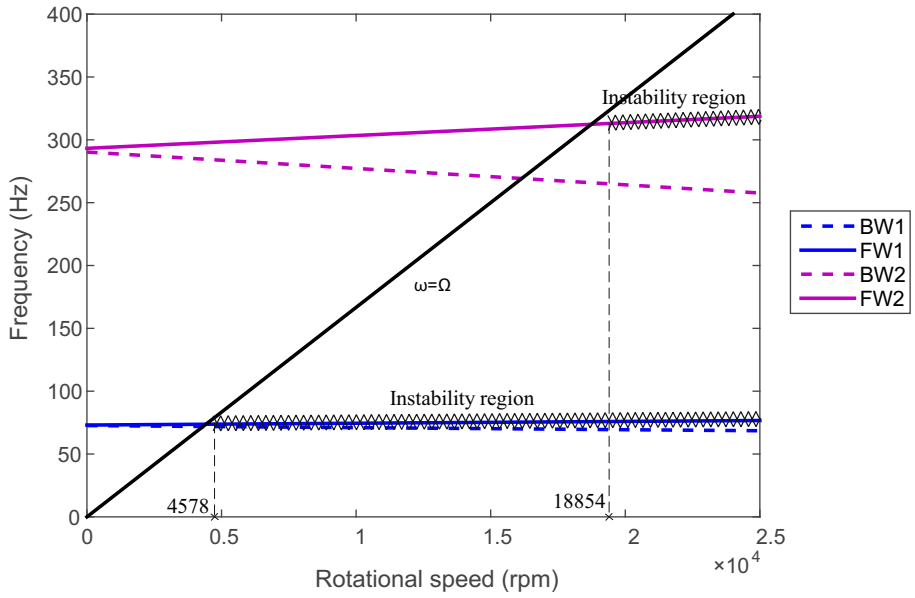

Figure 6.9. Case: isotopic bearings with coupled terms $K_{yz} = K_{zy} = 1 \times 10^7$ N/m

It can be seen from figure 6.8 that the instability occurs at the critical speeds for the forward modes (FW), while comparing figures 6.8 and 6.9, it can be observed that the associated coupling terms destabilize the forward modes at rotational speeds slightly higher than the critical speeds.

Considering now the isotropic bearings with external damping, figures 6.10 and 6.11 show the Campbell diagrams of the rotating composite shaft supported by isotropic bearings with different values of external damping. It can be observed that the external damping introduced by the bearings increases quite the threshold instability and for higher external damping, the rotor would be stable at all rotational

speeds.

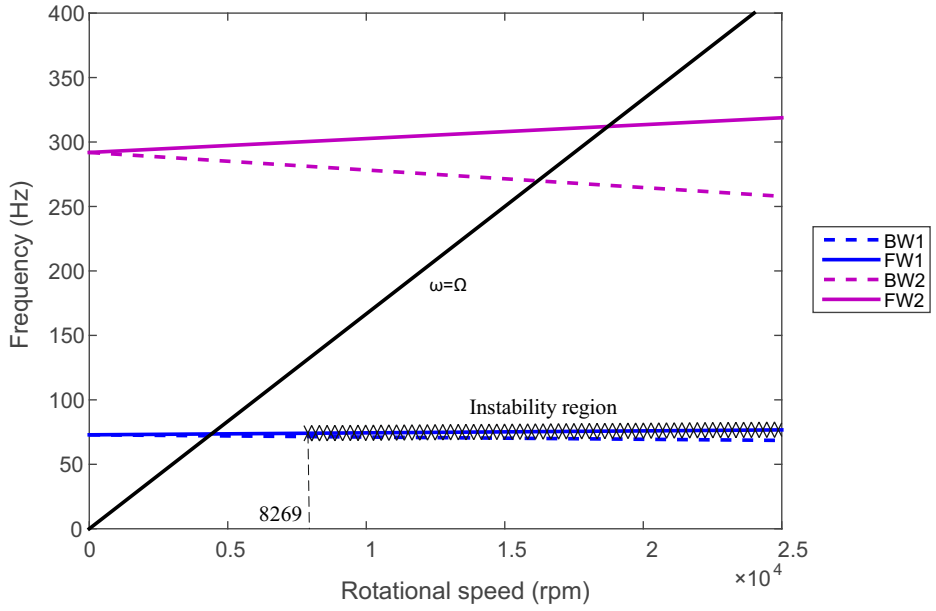

Figure 6.10. Case: isotopic bearings with external damping $C_{yy} = C_{zz} = 1 \times 10^2$ N/m/s

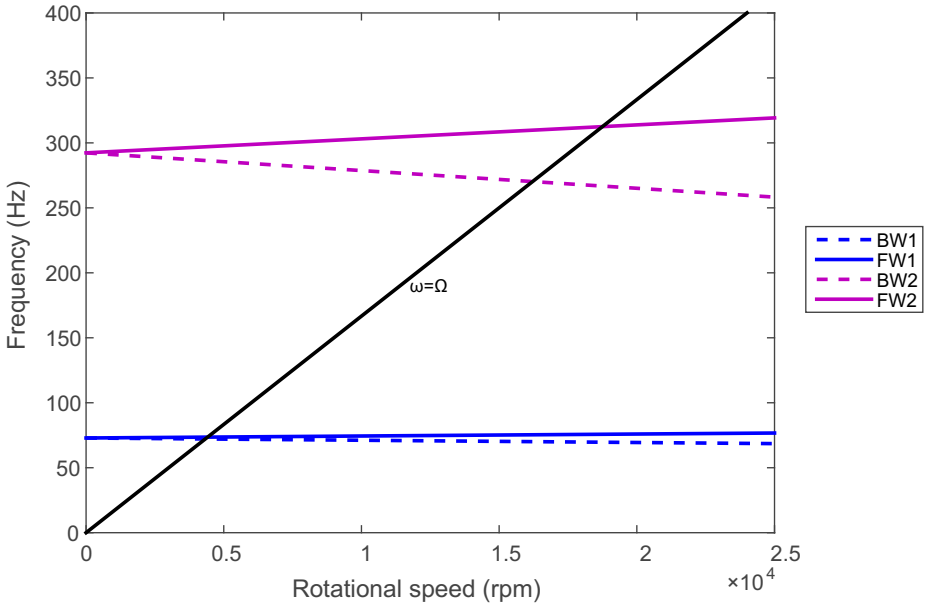

Figure 6.11. Case: isotopic bearings with external damping $C_{yy} = C_{zz} = 1 \times 10^4$ N/m/s

Figure 6.12 shows the Campbell diagrams of the rotating composite shaft supported by isotropic bearings with external damping and coupled terms. Comparing figures 6.10 and 6.12, it can be observed that the coupled terms introduced by the bearings increase slightly the threshold instability. It can be concluded that rotor stability is improved by increasing the damping and the coupled terms provided by the bearings, whereas increasing internal composite material damping may reduce the instability threshold.

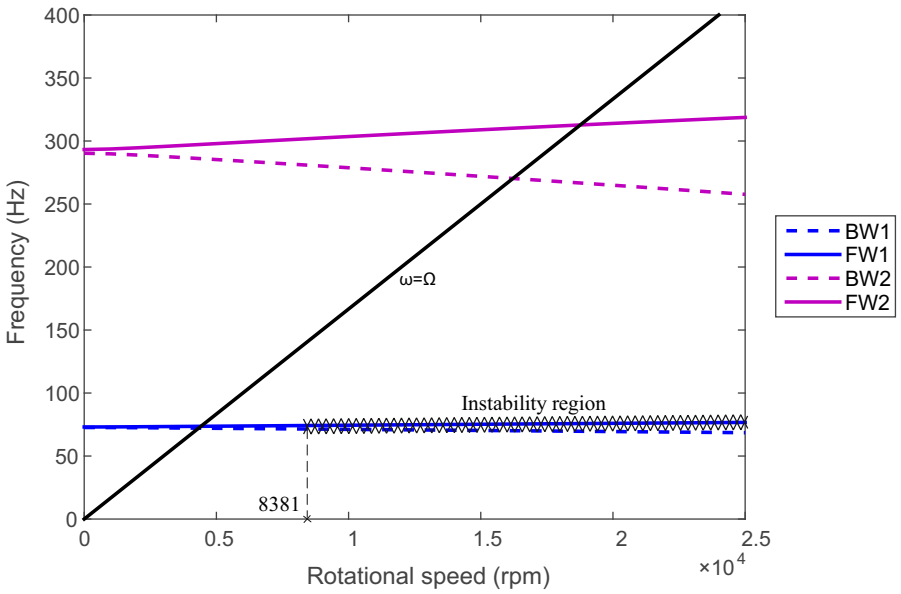

Figure 6.12. Case: isotopic bearings with external damping $C_{yy} = C_{zz} = 1 \times 10^2$ N/m/s and coupled terms $K_{yz} = K_{zy} = 1 \times 10^7$ N/m

6.8 Conclusion

The stability analysis of internally damped rotating composite shafts using the finite element method is presented in this chapter. The developed Equivalent single layer theory (ESLT) is compared to the classical equivalent modulus beam theory (EMBT) and the simplified homogenized beam theory (SHBT). The agreement has been found to be good in terms of natural frequencies, critical speeds and instability threshold compared with results available in the literature using different theories. Developed ESLT avoids the main drawbacks associated with EMBT, that considers only symmetric stacking sequences. A quantitative study of the effects of various parameters on natural frequencies and instability threshold of rotating composite shafts was carried out. The analysis shows that as higher is the fiber orientation angle, higher is the internal damping introduced by composite material. Therefore, the instability regions occurs at lower rotational speed. The study shows also that the rotor stability can be improved by increasing the damping of the bearings, whereas increasing internal damping may reduce the instability threshold. Thus, the fiber orientation, stacking sequence and bearings properties can be considered as optimization parameters for the dynamic behaviour and stability analysis of rotating composite shafts.

Conclusions and Future Works

✣ Conclusions:

The analysis of free vibration and frequency response of rotating composite shafts using the finite element method is presented in this work. Several examples have been processed to validate different deformation theories and finite element formulations and to determine the influence of different geometrical and physical parameters on rotating composite shaft dynamic and stability behaviours. Results are consistent with those available in the literature. This work has allowed us to reach the following conclusions:

- The gyroscopic effect induces a coupling of the orthogonal displacements to the rotation axis which has the consequence of separating natural frequencies to a forward and backward movement according to the direction of the shaft rotating movement. In the case of forward, this movement is in the same direction with the shaft rotation while, in the case of backward, this movement is in the opposite direction. This effect has an important influence on the dynamic behaviour of rotating composite shafts.

- Dynamic characteristics of the rotating composite shafts such as natural frequencies and critical speeds are influenced by changing stacking sequences, fiber orientations, length, mean diameter, nature of the materials, rotational speeds and boundary conditions.

- Natural frequencies of the rotating steel shaft and aluminium shaft are close to those of the rotating composite shaft with identical geometrical properties where the layer's fibers are oriented at 45°.

- The variation of the stacking sequence and fiber orientation and the shear-normal coupling have significative effects on the dynamic behaviour of rotating composite shafts.

- Elastic bearings properties and disk positions have an important influence on the dynamic characteristics of the rotating composite shafts.

- Mechanical couplings such as bending-bending, shear-normal and stretching-twisting of the rotating composite shafts are influenced by changing stacking sequences, number of layers, fiber orientations and rotational speeds.

- A new multi-layer finite element for rotating laminated shafts based on layerwise theory is formulated and implemented in order to dispose of a more realistic description of the displacement field; this finite element has revealed particulary adequate to analyse the dynamic behaviour of composite shafts, functionally graded material shafts and viscoelastic damping treatments with a constrained layer configuration.

- The constituent material properties and the power law index have an important influence on the dynamic behaviour of functionally graded material rotating shafts.
- The passive viscoelastic damping treatments technology reveals efficient, although the relation between the introduced damping capacity and the added mass seems to be an important parameter.
- A quantitative study of the effects of various parameters on natural frequencies and instability threshold of internally damped rotating composite shafts shows that as higher is the fiber orientation angle, higher is the internal damping introduced by composite material, and consequently, the instability regions occurs at lower rotational speed.
- Fiber orientations, stacking sequences and bearings properties are considered as optimization parameters for the dynamic behaviour and the stability of rotating composite shafts.
- Rotor stability is improved by increasing the damping of the bearings, whereas increasing internal damping may reduce the instability threshold.
- The presence of external damping and coupled terms trend to reduce the instability regions.
- The different case studies analysed show the possibility of using rotating composite shafts in some applications due to their tolerable dynamic and stability characteristics via stacking sequences and fiber orientations.

✣ Future works:

Based on the developed work, several other studies can be made from the present one and such as, some suggestions are made for further development of the present work:

- Selection and manufacture of composite shaft specimens for the experimental modal analysis.
- Proper validation of the composite shaft model for $\Omega = 0$ with an experimental modal analysis and validation of the presented results.
- Development of finite element formulation based on Timoshenko theory for the stability analysis of hysteretic internally damped rotating composite shafts.

References

Alwan, V., Gupta, A., Sekhar, A., and Velmurugan, R. (2010). Dynamic analysis of shafts of composite materials. *Journal of Reinforced Plastics and Composites*, 29(22):3364–3379.

Badie, M., Mahdi, E., and Hamouda, A. (2011). An investigation into hybrid carbon/glass fiber reinforced epoxy composite automotive drive shaft. *Materials and Design*, 32:1485–1500.

Balasubramanian, M. (2014). *Composite materials and processing*. CRC Press.

Bauchau, O. A. (1981). *Design, Manufacturing and Testing of High Speed Rotating Graphite/Epoxy Shafts*. PhD thesis, S.M. Massachusetts Institute of Technology.

Bhajantri, V., Bajantri, S., Shindolkar, A., and Amarapure, S. (2014). Design and analysis of composite drive shaft. *International Journal of Research in Engineering and Technology*, 3:738–745.

Boukhalfa, A. (2014). Dynamic analysis of a spinning functionally graded material shaft by the p-version of the finite element method. *Latin American Journal of Solids and Structures*, 11:2018–2038.

Boukhalfa, A., Hadjoui, A., and Cherif, S. H. (2008). Free vibration analysis of a rotating composite shaft using the p-version of the finite element method. *International Journal of Rotating Machinery*, 2008:1–10.

Chandra, R., Singh, S., and Gupta, K. (1999). Damping studies in fiber-reinforced composites - a review. *Composite Structures*, 46:41–51.

Chang, C., Chang, M., and Huang, J. (2004a). Vibration analysis of rotating composite shafts containing randomly oriented reinforcements. *Composite Structures*, 63:21–32.

Chang, M., Chen, J., and Chang, C. (2004b). A simple spinning laminated composite shaft model. *International Journal of Solids and Structures*, 41:637–662.

Chen, L. and Ku, D. (1990). Dynamic stability analysis of a rotating shaft by the finite element method. *Journal of Sound and Vibration*, 143(1):143–151.

Chen, L. and Peng, W. (1998a). Dynamic stability of rotating composite shaft under periodical axial compressive loads. *Journal of Sound and Vibration*, 212(2):215–230.

Chen, L. and Peng, W. (1998b). The stability behavior of rotating composite shaft under axial compressive loads. *Composite Structures*, 41(3-4):253–263.

Chowdhuri, M. and Hossain, R. (2010). Design analysis of an automotive composite drive shaft. *International Journal of Engineering and Technology*, 2(2):45–48.

Dongare, P. and Deshmukh, S. (2013). Effect of fiber angle orientation on stress, deformation and buckling torque of the composite drive shaft. *Global Journal of Researches in Engineering-Mechanical and Mechanics Engineering*, 13:1–7.

Ewins, D. (1984). *Modal Testing: Theory and Practice*. Research Studies Press LTD.

Freund, J. and Karakoc, A. (2016). Shear and torsion correction factors of timoshenko beam model for generic cross sections. *Research on Engineering Structures and Materials*, 2:19–27.

Gay, D. (2003). *Composite Materials: Design and Applications*. CRC Press.

Genta, G. (2004). On a persistent misunderstanding of the role of hysteretic damping in rotordynamics. *Journal of Vibration and acoustics*, 126:459–461.

Genta, G. (2005). *Dynamics of Rotating Systems*. Springer.

Ghoneam, S., Hamada, A., and Elamy, M. (Unknown year). Dynamic analysis of a rotating composite shaft. *Department of Production Engineering and Mechanical Design, Faculty of Engineering, Menoufiya University, Egypt*.

Gindele, J., Novak, W., Fietkau, P., Neuwirth, P., and Leitermann, W. (2015). The transaxle powertrain of the mercedes-amg sports cars.

Gubran, H. and Gupta, K. (2005). The effect of stacking sequence and coupling mechanisms on the natural frequencies of composite shafts. *Journal of Sound and Vibration*, 282:231–248.

Gubran, H. and Gupta, K. (2014). Design optimization of automotive propeller shafts. *Journal of Vibration Engineering and Technologies*, 2(1):35–45.

Gupta, A., Sekhar, A., and Velmurugan, R. (2009). Damping estimation and dynamic analysis of a composite shaft - rotor system. *Presented at the Sixteenth International Congress on Sound and Vibration*.

Gupta, K., editor (2011). *IUTAM Symposium on Emerging Trends in Rotor Dynamics*. Springer Netherlands.

Gupta, K. (2015). Composite shaft rotor dynamics: An overview. In Sinha, J., editor, *Vibration Engineering and Technology of Machinery*, pages 79–94. Springer International Publishing Switzerland.

Hinton, E. and Owen, D. (1981). *An introduction to finite element computation*. Pineridge Press Limited.

Johnson, C. (1995). Design of passive damping systems. *Journal of Vibration and Acoustics*, 117(B):171–176.

Khoshravan, M. and Paykani, A. (2012). Design of a composite drive shaft and its coupling for automotive application. *Journal of Applied Research and Technology*, 10:826–834.

Khoshravan, M., Paykani, A., and Akbarzadeh, A. (2011). Design and modal analysis of composite drive shaft for automotive application. *International Journal of Engineering Science and Technology*, 3(4):2543–2549.

Kim, C. and Bert, C. (1993). Critical speed analysis of laminated composite, hollow drive shafts. *Composites Engineering*, 3(7–8):633–643.

Lalanne, M., Berthier, P., and Hagopian, J. D. (1986). *Mécanique des Vibrations Linéaires*. Masson.

Lalanne, M. and Ferraris, G. (1990). *Rotordynamics Prediction in Engineering*. John Wiley and Sons.

Lee, D., Kim, H., Kim, J., and Kim, J. (2004). Design and manufacture of an automotive hybrid aluminum/composite drive shaft. *Composite Structures*, 63:87–99.

Loy, C., Lam, K., and Reddy, J. (1999). Vibration of functionally graded cylindrical shells. *International Journal of Mechanical Sciences*, 41:309–324.

Montagnier, O. and Hochard, C. (2007). Dynamic instability of supercritical driveshafts mounted on dissipative supports-effects of viscous and hysteretic internal damping. *Journal of Sound and Vibration*, 305:378–400.

Montagnier, O. and Hochard, C. (2013). Optimisation of hybrid high-modulus/high-strength carbon fibre reinforced plastic composite drive shafts. *Materials and Design*, 46:88–100.

Moorthy, R., Mitiku, Y., and Sridhar, K. (2013). Design of automobile driveshaft using carbon/epoxy and kevlar/epoxy composites. *American Journal of Engineering Research*, 2:173–179.

Moreira, R. and Rodrigues, J. D. (2006). A layerwise model for thin soft core sandwich plates. *Computers and Structures*, 84:1256–1263.

Moreira, R., Rodrigues, J. D., and Ferreira, A. (2006). A generalized layerwise finite element for multi-layer damping treatments. *Computational Mechanics*, 37:426–444.

Muslmani, M. A. (2013). *Rotordynamic Analysis of Tapered Composite Driveshaft Using Conventional and Hierarchical Finite Element Formulations*. PhD thesis, Concordia University Montreal, Quebec, Canada.

Newkirk, B. (1924). Shaft whipping. *General Electric Rev*, 27(3):169–178.

Patil, R. and Shinde, S. (2014). Layerwise theories for cross-ply laminated composite beam. *International Journal of Current Engineering and Technology*, 4(3):1753–1758.

Pereira, J. and Silveira, M. (2000). Instability regions due to internal damping on rotors in wounding shaft. *In: 21st Iberian Latin American Congress on Computational Methods in Engineering*.

Pereira, J. and Silveira, M. (2002). Evaluation and optimization of the instability regions on rotors in wounding shaft. *In: II National Congress of Mechanical Engineering*, pages 315–320.

Pradhana, S., Loy, C., Lama, K., and Reddy, J. (2000). Vibration characteristics of functionally graded cylindrical shells under various boundary conditions. *Applied Acoustics*, 61:111–129.

Rangaswamy, T. and Vijayarangan, S. (2005). Optimal sizing and stacking sequence of composite drive shafts. *Materials Science*, 11(2):133–138.

Rangaswamy, T., Vijayarangan, S., Chandrashekar, R., Venkatesh, T., and Anantharaman, K. (2002). Optimal design and analysis of automotive composite drive shaft. *International Symposium of Research Students on Materials Science and Engineering*, pages 1–9.

Reddy, J. (1993). An evaluation of equivalent-single-layer and layerwise theories of composite laminates. *Composite Structures*, 25:21–35.

Reddy, J. (1997). *Mechanics of Laminated Composite Plates - Theory and Analysis*. CRC Press.

Richardet, G., Chatelet, E., and Baranger, T. (2011). Rotating internal damping in the case of composite shafts. In Gupta, K., editor, *IUTAM Symposium on Emerging Trends in Rotor Dynamics*, pages 125–134. Springer Netherlands.

Roos, C. and Bakis, C. (2011). Multi-physics design and optimization of flexible matrix composite driveshafts. *Composite Structures*, 93:2231–2240.

Silveira, M. E. (2001). Análise do comportamento dinâmico de rotores em eixos bobinados. Master's thesis, Universidade Federal de Santa Catarina.

Singh, S., Gubran, H., and Gupta, K. (1997). Developments in dynamics of composite material shafts. *International Journal of Rotating Machinery*, 3(3):189–198.

Singh, S. and Gupta, K. (1996a). Composite shaft rotordynamic analysis using a layerwise theory. *Journal of Sound and Vibration*, 191(5):739–756.

Singh, S. and Gupta, K. (1996b). Dynamic analysis of composite rotors. *International Journal of Rotating Machinery*, 2(3):179–186.

Sino, R., Baranger, T., Chatelet, E., and Jacquet, G. (2008). Dynamic analysis of a rotating composite shaft. *Composites Science and Technology*, 68(2):337–345.

Talib, A. A., Ali, A., Badie, M., Lah, N. C., and Golestaneh, A. (2010). Developing a hybrid, carbon/glass fiber-reinforced, epoxy composite automotive drive shaft. *Materials and Design*, 31:514–521.

Tsai, S. (1984). *Composites Design*. PhD thesis, Wright-Patterson Air Force Base, Ohio.

Web1 (2017). http://www.smartturner.ca/double-suction-pumps.html.

Web2 (2017). http://www.trenew.ch/industry-automation.html.

Web3 (2017). https://www.energy.siemens.com/co/en/services/industrial-applications/compressors/#content=Siemens%20Turbocompressors%20(STC).

Wettergren, H. and Olsson, K. (1996). Dynamic instabilty of a rotating asymmetric shaft with internal viscous damping supported in anisotropic bearings. *Journal of Sound and Vibration*, 195(1):75–84.

Yongsheng, R., Xingqi, Z., Yanghang, L., and Xiulong, C. (2014). Vibration and instability of rotating composite thin-walled shafts with internal damping. *Hindawi Publishing Corporation-Shock and Vibration*, pages 1–10.

Zinberg, H. and Symonds, M. (1970). The development of an advanced composite tail rotor driveshaft. *Presented at the 26th Annual Forum of the American Helicopter Society, Washington, DC*.

Scientific Publications

✣ Published articles:

- Safa Ben Arab, José Dias Rodrigues, Slim Bouaziz, Mohamed Haddar, A finite element based on Equivalent Single Layer Theory for rotating composite shafts dynamic analysis. *Composite Structures* 178 (2017) 135–144, DOI: 10.1016/j.compstruct.2017.06.052.
- Safa Ben Arab, José Dias Rodrigues, Slim Bouaziz, Mohamed Haddar, Dynamic analysis of laminated rotors using a layerwise theory, *Composite Structures* 182 (2017) 335–345, DOI: 10.1016/j.compstruct.2017.09.033.

✣ Submitted article:

- Ben Arab S., Dias Rodrigues J., Bouaziz S., Haddar M., Stabilty Analysis of Internally Damped Rotating Composite Shafts Using a Finite Element Formulation, *Compte Rendus Mécanique*.

✣ International conferences:

- S. Ben Arab, S. Bouaziz, J. Dias Rodrigues, M. Haddar, Finite Elements Formulation for Composite Shafts, *International Conference Multiphysics and Simulation for Systems Design, MMSSD 2014, Sousse, Tunisia*.
- S. Ben Arab, J. Dias Rodrigues, S. Bouaziz, M. Haddar, Analysis of stacking sequence effects of the rotating composite shafts using a finite element formulation, *First International Conference on Automotive Composites, ICAutoC 2016, Lisbon, Portugal*.
- S. Ben Arab, J. Dias Rodrigues, S. Bouaziz, M. Haddar, Finite Element Formulation for Stability Analysis of Rotating Composite Shafts, *Seventh International Congress on Design and Modeling of Mechanical Systems, CMSM 2017, Hammamet, Tunisia*.

Composite Shaft Rotordynamic Analysis Using the Finite Element Method

Safa BEN ARAB CHAKER

Résumé: Ce travail est consacré à l'étude du comportement dynamique des rotors composites. Deux modèles éléments finis basés sur la théorie d'une seule couche équivalente et la théorie modifiée d'une seule couche équivalente sont développés pour modéliser les arbres composites rotatifs en utilisant la théorie des poutres de Timoshenko. De plus, un nouveau élément fini multicouche basé sur la théorie de couche par couche et la théorie d'arbre est formulé pour un arbre rotatif laminé. Ce modèle est mis en œuvre pour disposer d'une description plus réaliste du champ de déplacement à travers l'épaisseur de l'arbre laminé. Ces formulations sont introduites pour considérer les effets de l'orientation des fibres, de la séquence d'empilement et du couplage normal au cisaillement. En outre, une formulation d'éléments finis d'Euler-Bernoulli basée sur la théorie d'une seule couche équivalente considérant un amortissement interne hystérétique et les effets de cisaillement transversal est utilisée pour évaluer l'influence de divers paramètres sur les fréquences naturelles, les vitesses critiques et les seuils d'instabilité. Les résultats obtenus montrent que les théories développées peuvent être efficacement utilisées pour l'analyse dynamique des rotors composites et que la stabilité du rotor est sensible aux paramètres du laminage et aux propriétés des paliers.

Mots clés: Analyse dynamique, Analyse de stabilité, Méthode des éléments finis, Théorie de couche par couche, Arbre tournant, Matériau composite, Amortissement interne hystérétique.

Abstract: This work is concerned with the study of the vibratory behaviour of rotating composite shafts. A finite element models based on Equivalent Single Layer Theory and Modified Equivalent Single Layer Theory are developed to model the rotating composite shafts using Timoshenko beam theory. Moreover, a new multi-layer finite element for rotating laminated shaft based on Layerwise and shaft theories is formulated and implemented to dispose of a more realistic description of the displacement field through the laminated shaft thickness. Those formulations are introduced to consider the effects of fiber orientation, stacking sequence and shear-normal coupling. Furthermore, a Euler-Bernoulli shaft finite element formulation based on Equivalent Single Layer Theory including hysteretic internal damping and transverse shear effects is introduced and then used to evaluate the influence of various parameters on natural frequencies, critical speeds and instability thresholds. The close agreement in the obtained results shows that the developed theories can be effectively used for composite rotor dynamic analysis and that rotor stability is sensitive to laminate parameters and bearing properties.

Keywords: Dynamic analysis, Stability analysis, Finite element method, Layerwise theory, Rotating shaft, Composite material, hysteretic internal damping.